



**HAL**  
open science

# Rheophysics of granular materials with an interstitial fluid: a numerical simulation study

Saeed Khamseh

► **To cite this version:**

Saeed Khamseh. Rheophysics of granular materials with an interstitial fluid: a numerical simulation study. Fluid mechanics [physics.class-ph]. Université Paris-Est, 2014. English. NNT: . tel-01103346v1

**HAL Id: tel-01103346**

**<https://theses.hal.science/tel-01103346v1>**

Submitted on 14 Jan 2015 (v1), last revised 7 Mar 2015 (v2)

**HAL** is a multi-disciplinary open access archive for the deposit and dissemination of scientific research documents, whether they are published or not. The documents may come from teaching and research institutions in France or abroad, or from public or private research centers.

L'archive ouverte pluridisciplinaire **HAL**, est destinée au dépôt et à la diffusion de documents scientifiques de niveau recherche, publiés ou non, émanant des établissements d'enseignement et de recherche français ou étrangers, des laboratoires publics ou privés.



RHEOPHYSICS OF GRANULAR MATERIALS WITH AN  
INTERSTITIAL FLUID: A NUMERICAL SIMULATION STUDY

THÈSE

Présentée par

**Saeed Khamseh**

Pour obtenir le grade de

Docteur de l'Université Paris-Est

Dans la spécialité: **Sciences des Matériaux**

Soutenue le 05/05/2014 devant le jury composé de:

M. Bruno Chareyre	(rapporteur)
M. Jean-Yves Delenne	(rapporteur)
M. Ivan Iordanoff	(examineur)
M. Pierre Jop	(examineur)
M. Patrick Richard	(examineur)
M. Jean-Noël Roux	(directeur de thèse)
M. François Chevoir	(co-directeur de thèse)



# Acknowledgements

It was not possible to finish my PhD thesis without the help and support of many kind people around me. Foremost, I would like to express my deep gratitude to my supervisor Jean-Noël Roux for his patient guidance, enthusiastic encouragement, availability and readiness, and for being always kind and supporting in all aspects. Beside his vast knowledge in Physics, his great insight to science has been always inspiring for me. One who taught me that “we should appreciate every single scientific result”. I would like to express my very great appreciation to François Chevoir for his valuable and constructive suggestions and comments during the planning and development of this research work. I also want to express my gratitude to the reading committee Jean-Yves Delenne, Bruno Chareyre, Ivan Iordanoff, Pierre Jop and Patrick Richard, for their careful reading, their insightful comments and questions and their encouragement. My sincere thanks to my colleagues and staff members in Laboratoire Navier. I wish to thank my friends for their willingness helps, moral supports and motivations. Who made the last three years of my life in France full of pleasures and new experiences. Lastly, I would like to thank my family for all their love and encouragement. My parents who raised me and supported me in all my pursuits. My wife, Zhaleh, who has been a constant source of love, concern, support and strength all these years. I would like to express my heartfelt gratitude to her for her understanding, patience and love.





# Contents

<b>Introduction</b>	<b>1</b>
<b>1 Rheophysics of dry and wet granular materials and suspensions</b>	<b>3</b>
1.1 Some basic macroscopic mechanical properties of solid-like granular materials	3
1.1.1 Yield criterion . . . . .	4
1.1.2 Stress-strain response and plastic behaviour . . . . .	5
1.1.3 The critical state . . . . .	7
1.1.4 Some macroscopic effects of cohesion . . . . .	7
1.2 Grain-level mechanics and microstructure . . . . .	8
1.2.1 Contact mechanics . . . . .	8
Normal contact forces . . . . .	8
Tangential contact forces: elasticity and friction . . . . .	9
Friction and rolling friction . . . . .	10
1.2.2 Contact networks and internal states of granular assemblies . . . . .	11
Stress tensor . . . . .	11
Coordination number . . . . .	11
Relation between pressure and average force . . . . .	12
Force disorder . . . . .	12
Contact network and force anisotropies . . . . .	13
1.2.3 Cohesive and wet granular assemblies . . . . .	15
Cohesive grains . . . . .	15
Capillary forces . . . . .	16
1.2.4 Wet granular materials . . . . .	19
The role of roughness . . . . .	20
Liquid content, limit of pendular state . . . . .	21
Mechanical properties of wet granular materials . . . . .	22
1.3 Discrete simulations of granular materials (DEM) . . . . .	23
1.3.1 Some characteristic material states . . . . .	24
Critical state . . . . .	24
Loose configurations of adhesive particles. . . . .	25
1.3.2 Dimensional analysis . . . . .	25
Stiffness number . . . . .	26
Inertial number . . . . .	26
Reduced pressure . . . . .	26
Influence of dimensionless control parameters, in different regimes. . .	27
1.3.3 Implementation of DEM for plane shear flow . . . . .	27
Boundary condition and stress control . . . . .	28
Steady state and measurements . . . . .	29
1.4 Dense flow: the “ $\mu^*(I)$ rheology” . . . . .	30
1.4.1 From numerical results to constitutive modeling . . . . .	30
1.4.2 Pressure controlled versus volume controlled behaviour . . . . .	32

1.4.3	Dense flow of cohesive grains . . . . .	33
1.5	Dense suspensions . . . . .	33
1.5.1	Scope, basic properties . . . . .	34
	Granular suspensions . . . . .	34
	Diphasic aspects and the homogeneity issue . . . . .	35
	Macroscopic constitutive laws . . . . .	35
	Normal stresses and particle stresses . . . . .	36
	Viscosity divergence in the jamming limit . . . . .	36
1.5.2	Micromechanical modeling and simulations . . . . .	37
	Hydrodynamic interactions and hydrodynamic resistance matrix . . . . .	37
	The assumption of lubrication force dominance . . . . .	37
	Lubrication singularity and contact problem . . . . .	38
	Viscous jamming and hydroclusters . . . . .	39
1.5.3	The “granular” approach to suspension rheology . . . . .	39
<b>2</b>	<b>Shear flow of wet granular materials: capillary effects</b>	<b>43</b>
2.1	Model material and simulation technique . . . . .	43
2.1.1	Control Parameters . . . . .	44
2.2	Macroscopic analysis . . . . .	45
2.2.1	Steady state, macroscopic measurements . . . . .	45
2.2.2	Localization . . . . .	46
	Instantaneous velocity profile . . . . .	47
	Local solid fraction . . . . .	49
	Deviation from linear profile . . . . .	49
	Effect of system size . . . . .	51
2.2.3	Macroscopic behaviour and constitutive relations . . . . .	53
2.2.4	Contribution of different interactions to stresses . . . . .	56
2.2.5	Normal stress differences . . . . .	58
2.2.6	Influence of capillary force model on macroscopic behaviour . . . . .	59
	The Soulié formula for capillary forces . . . . .	59
	Influence of meniscus volume and force range . . . . .	60
	Influence of capillary force hysteresis . . . . .	62
2.3	Microscopic analysis . . . . .	63
2.3.1	Coordination number . . . . .	63
	Contact and distant coordination number . . . . .	63
	Total coordination number and saturation . . . . .	64
	Coordination number of tensile and compressive bonds . . . . .	65
	Coordination number of close neighbours . . . . .	65
2.3.2	Normal interactions . . . . .	67
	Pressure and average normal force . . . . .	67
	Probability distribution function of normal forces . . . . .	68
2.3.3	Anisotropy . . . . .	69
	Stress-anisotropy relation . . . . .	70
	Structural anisotropy . . . . .	71
	Mechanical anisotropy . . . . .	73
2.3.4	Calculation of stress components from microscopic parameters . . . . .	74
	Contribution of contacts to shear stress . . . . .	74
	Contribution of distant interactions to shear stress . . . . .	75
2.3.5	Microscopic origin of normal stress differences . . . . .	76
2.3.6	Influence of capillary force model on microscopic behaviours . . . . .	78
	Influence of the force range and meniscus volume . . . . .	78

	Influence of capillary force hysteresis . . . . .	78
2.3.7	Agglomeration . . . . .	79
	Age of contacts and of distant interactions . . . . .	79
	Clusters . . . . .	80
2.4	Summary and discussion . . . . .	84
<b>3</b>	<b>Rheology of very dense, viscous suspensions</b>	<b>87</b>
3.1	Numerical suspension model . . . . .	87
3.1.1	Interactions . . . . .	87
3.1.2	Boundary conditions . . . . .	88
3.1.3	Hydrodynamic resistance matrix, equations of motion . . . . .	88
3.1.4	Practical computation procedure . . . . .	89
3.1.5	Dimensional analysis and state parameters . . . . .	90
3.1.6	Macroscopic phenomena, rheology . . . . .	91
	Internal friction coefficient and solid fraction . . . . .	91
	Effective suspension viscosity . . . . .	91
	Viscosity of a random isotropic suspension . . . . .	91
	Contact contribution to shear stress . . . . .	92
	Normal stress differences . . . . .	92
3.1.7	Microscopic characteristics . . . . .	93
	Coordination numbers . . . . .	93
	Fabric parameters . . . . .	93
3.2	Conclusion . . . . .	93
<b>4</b>	<b>Conclusions and perspectives</b>	<b>97</b>
	<b>Appendices</b>	<b>99</b>
	<b>Appendix</b>	<b>101</b>
<b>A</b>	<b>Force and fabric Anisotropies, expression of stress components</b>	<b>101</b>
A.1	Expansions with anisotropy parameters . . . . .	101
A.1.1	Arbitrary functions . . . . .	101
A.1.2	Products, to leading order in anisotropy coefficients . . . . .	102
A.1.3	Fabric . . . . .	102
A.1.4	Average normal force . . . . .	102
A.1.5	Branch vector . . . . .	103
A.2	Stress components to first order in anisotropy parameters . . . . .	103
<b>B</b>	<b>Normal stress components, comparing microscopic estimation with direct measurements</b>	<b>105</b>
	<b>References</b>	<b>106</b>



# Introduction

Granular materials are assemblies of macroscopic solid particles, or grains, which interact at their contacts, such as sands, gravels, powders or seeds. Their crucial role in many natural processes and human activities, such as agriculture, civil engineering, mining and pharmaceutical industry and also their importance in many geological and medical studies, have attracted a lot of attention in many research fields including soft matter physics, soil mechanics and geomaterial studies. They form a vast family of materials, composed of grains with very different shapes and sizes. Depending on the size and the geometry of grains, the density of particles, the applied external forces, the type of interactions in grain scale and many other parameters, granular materials may exhibit quite different behaviors. Generally, these behaviors are very complex and it is very difficult to relate the macroscopic properties to those of microscopic constituents. Despite these difficulties, recent studies on granular materials have granted a remarkable progress to this field of study [6], especially given the improvement of computer performances and the development of numerical simulation techniques [109]. Computer simulation methods made it possible to investigate large scale systems in both macroscopic and microscopic levels. They provided a convenient way to study the different geometries and to define desired interaction models and also to have access to various structural details such as, configuration of particles, spatial and temporal distributions of velocities, local density, porosity, agglomeration and geometry of clusters.

A fundamental characteristic of granular material is their intermediate behavior: depending on the external load or the density of the particles, they may behave like a non-Newtonian fluid in fast flows or like a solid in slow flows. For many years, the studies on granular material have been mostly restricted to solid-like properties, motivated by many applications such as building structures on soil grounds or grain storing in silos. However, the applications of granular flow are also numerous, e.g., landslides, rock, ice and snow avalanches, river sedimentation, dune formation, soil liquefaction, and ice flow mechanics.

Most studies on granular flow have focused on dry materials, in which the effects of the interstitial fluids are negligible for the particle dynamics. However, the presence of an interstitial liquid is known to have important consequences, in solid-like as well as liquid-like situations. The amount of liquid in a granular sample can strongly affect its mechanical properties. For instance, to make a sand castle, one needs to add a small amount of water to the beach sands. The small amount of the interstitial water strongly increases the stability of the material and its resistance to the external load. On the other hand, large amounts of water may decrease the material stability, e.g., the landslide phenomenon in which the liquefied layer of a sand hill creeps down like a viscous fluid. Moreover, dense grains fully saturated by a liquid occur very often in natural or man-made settings such as slurries or composite materials. Understanding the flow properties of partially wetted granular materials and dense suspensions is a significant challenge.

This thesis deals with the rheology of granular materials in the presence of an interstitial liquid, which may entail capillary and/or viscous forces, depending on saturation and flow conditions. Both effects are studied separately by grain-level numerical simulations for model

---

systems: assemblies of spherical objects, with capillary or viscous forces acting in the liquid bridges joining close neighbours. We mainly investigate slow flows (as opposed to strongly agitated materials), which coincide in some quasi-static limit with plastic deformation. We exploit the wealth of information supplied by numerical simulations to relate the macroscopic mechanical properties of those materials to microscopic phenomena.

Granular flow modeling has benefited from important developments in recent years. Chap. 1 first provides a brief review of the basic current knowledge about dry and wet granular material and dense suspension rheology and of some of the recent advances which the reported research elaborates upon. The rheological properties of granular materials at small liquid saturation is studied in Chap. 2. In Chap. 3 we report and discuss the results obtained on the rheology of dense suspensions. The final chapter (Chap. 4) is a synthetic conclusion indicating future research directions.

# Chapter 1

## Rheophysics of dry and wet granular materials and suspensions

This chapter briefly reviews the state of the art on rheophysics of wet granular materials or granular pastes, which the results of this thesis rely on. We also present the basic ingredients of the simulation methods employed in the following chapters, and introduce the appropriate state variables, on the macroscopic (continuous) and microscopic (grains or contact networks) scales. We focus on rather dense assemblies of grains which may be classified as solid-like or liquid-like materials, and on large strain behaviour, excluding, on the one hand, the granular gases often studied, in analogy with molecular gases, by kinetic theories [24, 56]; and, on the other hand, the small-strain quasistatic behaviour and its complex modeling approaches, many of which were developed for geomaterials [33, 64, 37].

Perhaps the most basic feature of the rheology of such materials is the existence of a flow threshold: a surface, in stress space (generally implying the deviator stress, and most often its magnitude, relative to the average pressure) separating possible static states from situations of flow. Another, rather unique, feature of those materials is the coupling of density to deviatoric stresses and strains – Reynolds dilatancy [117]. Such aspects of granular mechanics are recalled in Sec. 1.1, which also evokes stress-strain relationships in the quasistatic regime and introduces the essential concept of *critical state*. Section 1.2 introduces the microscopic, grain-level interactions, and the most relevant variables describing the internal state of granular assemblies, with a specific attention paid to cohesive systems and capillary forces. The discrete simulation method exploiting those micromechanical ingredients is briefly presented in Sec. 1.3. We then turn to the rheology of dense granular flow in Sec 1.4 and introduce the recently developed approach and constitutive laws that we use as a starting point for the numerical studies reported in the present dissertation. While the previous ones situate our studies of low saturation wet granular materials (chapter 2), Section 1.5 defines the context for our studies of suspensions (chapter 3), insisting on the analogies with granular systems, and on the insights in very dense suspension rheology recently brought about by the adoption of a “granular” point of view.

### 1.1 Some basic macroscopic mechanical properties of solid-like granular materials

Solid-like granular materials are well-known in soil mechanics. There is a rich literature on the properties and constitutive modeling of granular assemblies, mostly derived from geotechnical engineering [152, 96]. Macroscopic constitutive laws have been designed, with various levels



of sophistication, which adequately describe the basic trends of quasistatic granular materials rheology.

In the context of our studies on the rheology in dense flow conditions, the most relevant known features of solid-like granular materials are the ones related to dense, steady plastic flows, their conditions of occurrence (the flow threshold or yield criterion, Sec. 1.1.1), the evolution from initial packings to such flow conditions at large strains (Sec. 1.1.2) and the *critical state* (Sec. 1.1.3)

### 1.1.1 Yield criterion

One essential basic feature of granular mechanics is the existence of a yield threshold, or surface in stress space, within which the material is able to remain in a solid state and support the applied load. As its boundary is reached, the material starts to flow. The most simple criterion, or condition for absence of failure, is the Coulomb one, according to which the tangential stress vector component,  $\tau$ , imposed to a surface and the normal stress vector component,  $\sigma$ , should satisfy the following inequality:

$$|\tau| \leq \mu^* \sigma + c. \quad (1.1)$$

$\mu^*$  and  $c$  are respectively called the coefficient of internal friction and the cohesion, and depend on the nature of the material [98]. On attempting to slide adjacent layers of materials along their mutual separation plane, internal friction angle  $\varphi$ , such that  $\tan \varphi = \mu^*$ , plays the role of the friction angle between rigid solid bodies, while the *cohesion*,  $c$ , characterizes the resistance to this tangential relative displacement in the absence of any normal load pressing the layers onto one another. An interpretation of  $c$  is that it might be due to a mutual attraction of those adjacent layers, giving rise to an equivalent normal stress  $\sigma_0$ , with  $c = \sigma_0 \tan \varphi$  (as one would observe between two magnetic, frictional plane surfaces attracting each other with force per unit area equal to  $\sigma_0$ ). Consequently, a non-vanishing cohesion is expected when the grains are attracted to one another. Assemblies of non-adhesive grains, such as sands, are generally devoid of macroscopic cohesion ( $c = 0$ ). In conformity with the sliding block analogy, failure is expected in materials abiding by the Mohr-Coulomb yield criterion in the form of sliding along surfaces for which (1.1) holds as an equality.

Internal friction angle  $\varphi$  should coincide with the “angle of repose” for cohesionless materials. At least, it is easy to show that, under gravity, no slope inclined with an angle larger than  $\varphi$  with respect to the horizontal can stay stable [98]. In a cohesive material, the repose angle might exceed  $\varphi$ , but depends, then, on the height of the slope. In the case of a material with homogeneous mass density  $\rho$ , the height  $H$  (measured vertically, as an elevation) of a slope inclined at angle  $\alpha > \varphi$  with the horizontal, and ending in a horizontal surface at the top, has an upper bound [98]:

$$H \leq \frac{4c \sin \alpha \cos \varphi}{\rho g (1 - \cos(\alpha - \varphi))}, \quad (1.2)$$

$g$  denoting the intensity of gravity. In particular, the free surface of a material sample under gravity might comprise vertical steps or “cliffs” ( $\alpha = 90^\circ$ ) of maximum height  $\frac{4c \cos \varphi}{\rho g (1 - \sin(\varphi))}$ . The value of  $c$  introduces a stress scale in the yield properties of a cohesive material, which gravity translates into a characteristic height.

$\sigma$  and  $\tau$ , in condition (1.1), are the coordinates in the so-called Mohr plane, i.e., the normal and tangential components of stress vector  $\underline{\sigma} \cdot \mathbf{n}$  on surfaces with unit normal vector  $\mathbf{n}$ . The locus of points of coordinates  $\sigma$ ,  $\tau$  in this plane for all possible values of  $\mathbf{n}$  are the three circles cutting the  $\sigma$  axis for abscissae  $\sigma_1 \leq \sigma_2 \leq \sigma_3$  equal to the three principal stresses, eigenvalues of the stress tensor. Fig. 1.1 shows the Mohr-Coulomb yield condition, i.e., the

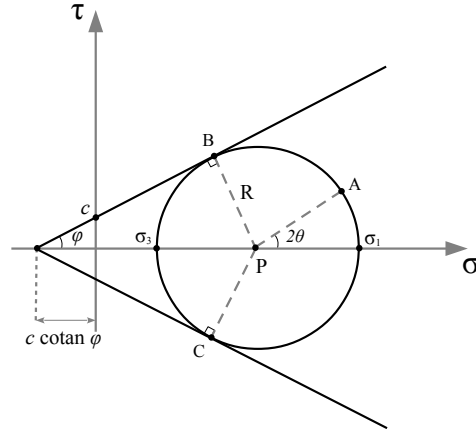


Figure 1.1: Mohr-Coulomb failure criterion.

cone where (1.1) holds as an equality. Condition (1.1) expresses that the largest Mohr circle, cutting the axis at abscissae  $\sigma_3$  and  $\sigma_1$  should be included in the interior region of the cone. Thus the Mohr-Coulomb condition may be expressed in terms of principal stresses as

$$\sigma_1(1 - \sin \varphi) - \sigma_3(1 + \sin \varphi) \leq c \cos \varphi. \quad (1.3)$$

It is independent of the intermediate principal stress,  $\sigma_2$ . Other criteria than Mohr-Coulomb are often more accurate and involve all three principal stresses, such as the Lade-Duncan criterion [79].

### 1.1.2 Stress-strain response and plastic behaviour

The yield criterion is quite a rough characterisation of the material, which is not sufficient to describe and model the onset of flow. It is of fundamental interest, and also practically useful in engineering applications, to be able to model the strains prior to failure.

One of the most common rheological tests on solid-like granular materials is the one carried out with the triaxial apparatus, as schematized in Fig. 1.2. Its design is motivated by the observation of a reasonably homogeneous state of stress and strain in a sample, thereby enabling the identification of constitutive stress-strain laws, to be applied at the level of a representative volume element in more general situations. In this test a cylindrical sample

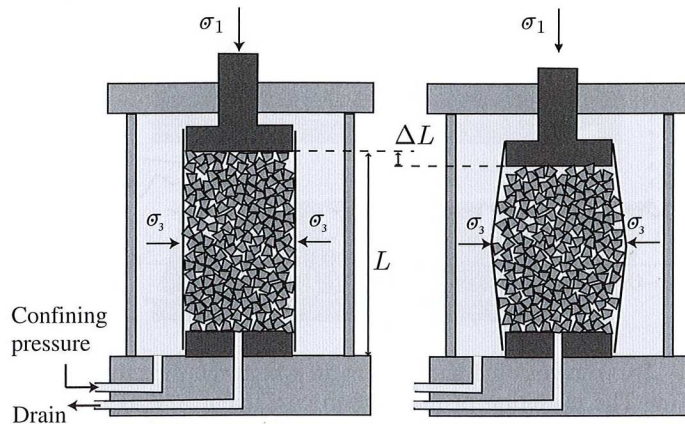


Figure 1.2: Triaxial test.

of material is wrapped in a flexible, impervious membrane and then immersed in a confining

cell filled with a fluid. Thus a lateral confining stress  $\sigma_2 = \sigma_3$ , equal to the fluid pressure, is applied, on which an additional vertical stress (in the direction of the cylinder axis) may be controlled through the force applied on the top and bottom horizontal platens, thus ensuring  $\sigma_1 > \sigma_3$ . Most often, one actually controls the vertical strain rate  $\dot{\epsilon}_1$ , set to a small value (typically of order  $10^{-4}$  or  $10^{-5}$  s $^{-1}$ ), in order to investigate the quasi-static material behaviour. Special care has to be exercised in the preparation stage, especially for cohesionless materials, to ensure sample homogeneity and axial symmetry. In careful experiments stresses and strains are uniform, at least in the central part of the specimen, away from the top and bottom boundaries. The most accurate results are obtained if strains are directly measured on the sample itself, in its central part, with precision sensors. The most accurate measurements are able to record strain variations of order  $10^{-5}$  or  $10^{-6}$  [78, 132, 65, 53]. More standard devices, however, simply record the approach of the top and bottom platens, and the variation of the internal sample volume, by monitoring the quantity of liquid contained in the pores of a saturated sample (maintained at atmospheric pressure). It is standard to measure deviator stress  $q = \sigma_1 - \sigma_3$  and volumetric strain (relative volume decrease)  $\epsilon_v$ , versus *axial strain*  $\epsilon_1$ <sup>1</sup>. The material behaviour investigated in such a test concerns the effect of stress *increments*, added to the initial isotropic state of stress. The application of the initial pressure is the final part of the preparation process that determines the initial state of the material probed in a triaxial test. The first part of the preparation stage is the assembling of the sample, and it is known to be of crucial importance, as it influences the material properties such as the maximum deviator stress. The maximum value of principal stress ratio in a cohesionless material, according to the Mohr-Coulomb criterion is, from (1.3),

$$\left(\frac{\sigma_1}{\sigma_3}\right)_{\max} = \frac{1 + \sin \varphi}{1 - \sin \varphi},$$

and thus the internal friction angle corresponding to material stability (static angle) depends on material preparation.

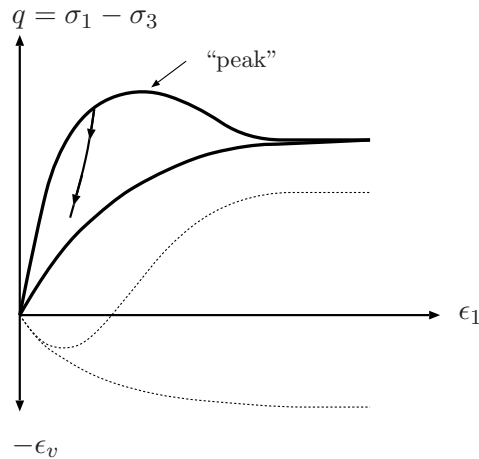


Figure 1.3: Aspect of stress-strain curves obtained in initially dense (upper curves) and loose (lower curves) cohesionless systems:  $q$  versus  $\epsilon_1$  (solid lines),  $\epsilon_v$  versus  $\epsilon_1$  (dotted lines). The axis points downwards for volumetric strains, so that a growing  $\epsilon_v$  curve corresponds to positive dilatancy.

The most important factor by which the initial state influences the yield criterion, and

---

<sup>1</sup>Throughout the thesis we adopt the conventions of soil mechanics for stresses and strains: tensile stresses are negative, and so are strains expressing relative increases of lengths. Thus the small strain tensor associated with displacement field  $\mathbf{u}$  is  $\underline{\underline{\epsilon}} = -\frac{1}{2}(\underline{\underline{\nabla}}\mathbf{u} + \underline{\underline{\nabla}}\mathbf{u}^T)$ .

the strains prior to the full mobilization of internal friction, is its density, or solid fraction  $\Phi$  (fraction of sample volume occupied by the solid grains). Fig. 1.3 schematically illustrates the behaviours of a dense and of a loose cohesionless sample in triaxial compression. While the initially dense systems reach a maximum deviator stress for some value of  $\epsilon_1$  (typically, a few percent), and then decreases to a plateau for larger strains (30-50%), the deviator in loose ones grows monotonically, and approaches the same plateau for large strains. Meanwhile, the density increases (positive, growing  $\epsilon_v$ , or downward curve on the graph of Fig. 1.3) in loose systems, and decreases (after an initial increase for small  $\epsilon_1$ ) in dense ones. Dense states exhibit positive dilatancy, loose ones negative dilatancy or contractancy. Upon reversal of the load direction (changing the sign of  $\dot{\epsilon}_1$ ), the “unloading” stress-strain curves do not coincide with the initial “loading” response (see the load reversal curve, with arrows, for some interval of  $\epsilon_1$  in Fig. 1.3, for the dense case). The response on the scale relevant for Fig. 1.3 is not reversible, and if modeled as elastoplastic, should comprise work hardening (i.e., inside the yield criterion, the response is not reversible elastic).

After large enough strains, the material (Fig. 1.3) keeps deforming at constant deviator stress and constant density (constant  $\epsilon_v$ ). It turns out that, whatever the initial value of the density, its value once this plateau is reached is the same (save for some possible pressure effects, to be discussed below). This is the *critical state*, obtained after a sufficiently large strain accumulated in the same direction.

### 1.1.3 The critical state

An important basic concept of soil mechanics [129, 152], the critical state is the product of the deformation process, and independent of the initial state. The granular material, once this attractor state is reached, keeps deforming at constant density, and behaves, for the same load, as a perfectly plastic one.

The critical state, in general, and in particular the values of critical solid fraction  $\Phi_c$  and critical internal friction  $\mu_c^*$ , depends on confining stress  $\sigma_3$ , or equivalently on the average pressure  $\mathcal{P}$ , defined as

$$\mathcal{P} = \frac{1}{3}(\sigma_1 + \sigma_2 + \sigma_3) \quad (1.4)$$

– an issue which we further discuss in Sec. 1.1.4.

The critical state solid fraction  $\Phi_c$  is the value separating *dense* initial states, for which, after a small initial contraction, the material will dilate towards its final steady state with  $\Phi = \Phi_c$ , from loose ones, which will contract towards the same final density. The critical state represents an important limit for rheology of dense flow, as we shall see in the next sections, the limit of slow flow or *quasistatic limit*.

As we are to deal with granular flow, we will focus on shear tests, rather than triaxial ones, as, in simple shear, arbitrary large strains can be attained and properties of steady flows can be measured accurately on averaging over time. Shear tests are much easier to carry out as virtual, numerical experiments than as real ones in the laboratory, and will therefore be discussed in Sec. 1.3.

### 1.1.4 Some macroscopic effects of cohesion

The presence of cohesion in the Mohr-Coulomb yield criterion has the important consequence of introducing a stress scale in the material behaviour – as previously remarked in connection with Eq. 1.2 the maximum height of a steep slope is related to some maximum value of stresses. While cohesionless materials are essentially sensitive to *ratios* of stress components, cohesive ones will respond differently according to the *absolute magnitude* of stresses. This is quite conspicuous on dealing with compression tests in which all stress ratios remain constant.

The simplest one is the isotropic compression test. In the oedometric test, stress  $\sigma_1$  increases, while all strains other than  $\epsilon_1$  are maintained to zero. It is usually performed on horizontal layers of material, or samples with low height to width ratio, assembled under gravity. The oedometric test is also observed to correspond to constant principal stress ratio  $\sigma_3/\sigma_1$ . In such situations, while cohesionless soils exhibit little density change on increasing stresses, cohesive ones undergo some irreversible compaction under growing  $\mathcal{P}$  (the average pressure, as defined in (1.4)), which is traditionally modeled [12] as a linear variation of the *void ratio*, i.e.,  $e = -1 + 1/\Phi$ , with the logarithm of  $\mathcal{P}$ :

$$e = e_0 - C_c \ln \left( \frac{\mathcal{P}}{\mathcal{P}_0} \right) \quad (1.5)$$

Relation 1.5, written with somewhat arbitrary reference values  $e_0$  and  $\mathcal{P}_0$ , applies to materials such as clays [12] and also to cohesive powders, over rather wide interval of void ratios ( $e$  varying by factors of 2 or even 4). It also applies to critical states, characterized by a specific value of stress ratio  $\sigma_3/\sigma_1$ , and the compression curve is often modeled with the same slope  $C_c$  (the compression index). For soils such laws are generally regarded as applicable in the range 10 kPa to 1 MPa, relevant for most geotechnical applications. Relation 1.5 only applies to growing pressures. The irreversibility of the plastic compression phenomenon implies that it does not apply to pressure values lower than the highest pressure reached in the past, or *preconsolidation pressure*. Similar observations on sands are reported, but the change of density is considerably lower, and it is also remarked that irreversible compression is to a large extent due to grain crushing and damage.

## 1.2 Grain-level mechanics and microstructure

This section is devoted to the description of grain interactions and of microstructural and micromechanical variables pertaining to granular materials. We first deal with cohesionless systems. We introduce the contact mechanics models (Sec. 1.2.1) used in numerical simulations of granular assemblies, and then the variables characterizing contact networks and the relations between microscopic and macroscopic descriptions (Sec. 1.2.2). Then we discuss grain-level cohesion models, capillary forces and their effects on all previously introduced features of granular micromechanics in Sec. 1.2.3.

### 1.2.1 Contact mechanics

In order to understand the microscopic origins of the mechanics of granular assemblies, we need to specify the appropriate grain interaction models. Those have several origins, and do not have the same physical status. Neither do they equally influence the mechanics of the material on the macroscopic scale. We focus here on the choice of models that are implemented in our own simulations, with a few words of justification. Most choices are identical to the ones used in [1, 104].

#### Normal contact forces

Such forces are essentially due to elastic repulsion. Contact elasticity is well studied and documented, at least for smooth, regular shaped grains with well-defined tangent planes and curvatures all over their surfaces – in which case the Hertz theory applies [72].

Let us consider two interacting particles of diameter  $a_1$  and  $a_2$  and masses  $m_1$  and  $m_2$  interacting in their contact with an elastic force. The normal deflection  $h$  in the contact point

of two spheres with the center to center distance  $d$  is defined as,

$$h = (a_1 + a_2)/2 - d \quad (1.6)$$

In a two dimensional case, the normal elastic force is proportional to the normal contact deflection as  $N = K_N h$ , in which  $K_N$  is a normal stiffness constant. For 3D spheres it can be calculated, and Hertz's law [72] gives

$$N = \frac{\tilde{E}}{3} \sqrt{a} h^{3/2}. \quad (1.7)$$

In this equation,  $a = 2a_1 a_2 / (a_1 + a_2)$  is the harmonic mean of diameters and  $\tilde{E}$  is a notation for  $E/(1 - \nu^2)$ , where  $E$  is the Young modulus of the grains and  $\nu$  their Poisson ratio. The normal stiffness  $K_N$  can be defined as the rate of the change of the force with normal relative displacement as

$$K_N = \frac{dN}{dh} = \frac{\tilde{E}}{2} \sqrt{a} h^{1/2} = \frac{(3a)^{1/3}}{2} \tilde{E}^{2/3} N^{1/3} \quad (1.8)$$

In addition to the normal elastic force a damping force might be used in numerical simulation models, although its physical origin is less known in general. The viscous force opposes the relative normal velocity  $\delta v = \dot{h}$  and is given by

$$N^\nu = \alpha_N(h) \dot{h} \quad (1.9)$$

In generically disordered systems, this damping force might be attributed to the viscoelastic properties of the material which the grains are made of [21], but it is most often used as a computational trick to ease the approach to mechanical equilibrium states in the practice of numerical simulation of granular assemblies. In such cases, it is of course necessary to assess the influence of this choice of a damping model on the investigated mechanical properties. One may choose the damping coefficient as a fixed fraction  $\zeta$  of the critical damping coefficient in the linear spring of stiffness constant  $K_N(h)$  (as in [1, 104]):

$$\alpha_N(h) = 2\zeta \sqrt{m^*} K_N = \zeta (2m^* \tilde{E})^{1/2} (ah)^{1/4}, \quad (1.10)$$

where  $m^* = m_1 m_2 / (m_1 + m_2)$  is the reduced mass of the pair of particles of masses  $m_1$  and  $m_2$ . Interestingly, such a choice, in spite of the nonlinearity of the contact law, results in a velocity-independent normal restitution coefficient in binary collisions [21].

### Tangential contact forces: elasticity and friction

Just like a normal relative displacement entails a normal elastic force, a tangential relative displacement of the contact region gives rise to a tangential elastic force. The tangential relative displacement, denoted as  $\mathbf{u}_T$ , in a small motion of contacting grains 1 and 2, is the difference of displacements of the contact point (or center of the contact region), if regarded as following the rigid body motion of grain 1, or if regarded as following the rigid body motion of grain 2. Regarding the surfaces of the grain as frictional, with friction coefficient  $\mu$ , the ratio of the tangential to the normal component of the stress vector at any point of the contact surface is requested not to exceed  $\mu$ , and sliding might occur where this bound is reached. A standard result of contact mechanics between smooth surfaces [72] is that any non-vanishing  $\mathbf{u}_T$ , imposed at constant deflection  $h$ , gives rise to some slip in part of the contact surface (initially on an external annulus). The resulting contact mechanics, as studied in a classical paper by Mindlin and Deresiewicz [94], is very complex and hysteretic, with the distribution of tangential stresses in the contact region sensitive to the history of  $\mathbf{u}_T$ . Some authors [148] attempted to retain some of this complexity in a numerically tractable



contact model. However, a more simplified version of the Mindlin-Deresiewicz results will be implemented in our simulations, as in quite a few numerical works [1, 85]. In many cases of interest, the model for tangential stiffness has little influence on macroscopic material properties. Even elastic moduli [3] were observed to be hardly affected by a greater refinement in the choice of the model for  $K_T$ . The simplified model uses the following incremental relation between tangential elastic force  $\mathbf{T}$  and relative tangential displacement  $\mathbf{u}_T$ , involving a tangential stiffness  $K_T$  which depends on deflection  $h$  (or, equivalently, on normal elastic force  $N$ ):

$$d\mathbf{T} = K_T d\mathbf{u}_T, \quad (1.11)$$

with

$$K_T = \frac{2 - 2\nu}{2 - \nu} K_N = \frac{1 - \nu}{2 - \nu} \tilde{E} \sqrt{ah}^{1/2}. \quad (1.12)$$

The expression of (1.12) corresponds to the value of  $K_T$  in the absence of any tangential relative displacement  $\mathbf{u}_T$ . To enforce the Coulomb condition with friction coefficient  $\mu$  this relation is to be modified. Whenever the elastic force component  $\mathbf{T}$  given by Eq. 1.11 is to exceed  $\mu N$ , it is immediately projected back onto the circle of radius  $N$  in the tangential plane. Furthermore, the norm of  $\mathbf{T}$  should be reduced in proportion to the stiffness coefficient  $K_T$  when  $N$  decreases, as advocated by Elata & Berryman [41], to avoid spurious increases of elastic energy. Finally, the tangential force should follow the material motion and satisfy the objectivity rule [77]. Its intensity is assumed constant in any rolling relative motion, while its direction follows the normal vector in its rotations, and spins around it by an angle equal to the average of the pivoting angle of the two grains in contact [1].

As for normal forces, an additional viscous contribution to the tangential force could be introduced, involving a damping coefficient  $\alpha_T(h)$ .  $\alpha_N(h)$  and  $\alpha_T(h)$  were observed not to influence the mechanical properties in quasistatic conditions or in dense, inertial flows [125]. They do nevertheless affect the results of some assembling procedures [42].

Many simulations of granular materials are carried out in which no attempt is made to accurately model the elastic part of the contact law. The normal repulsive force, with an intensity growing with  $h$ , is then regarded as a suitable numerical trick to prevent solid particles from overlapping. The *contact dynamics* simulation method [112, 70] deals with nominally rigid, undeformable grains (although small overlaps have to be tolerated). The advantage of using more realistic elastic deflections, as in (1.7), is that elastic properties of granular materials can be predicted in a simulation and confronted to experimental results [3]. The relevance of contact deflections for different rheological regimes [127] is briefly discussed in Sec. 1.3.

### Friction and rolling friction

In many situations of interest, the Coulomb inequality,

$$\|\mathbf{T}\| \leq \mu N, \quad (1.13)$$

and the value of friction coefficient  $\mu$  it contains, plays a more important role than contact elasticity and relations of force components  $N$ ,  $\mathbf{T}$  to relative displacements at contacts.

It has also been observed that *rolling friction* significantly affects the mechanics of granular assemblies. Rolling friction originates in surface roughness, causing intergranular contacts to occur through several asperities. Contacts, having a finite extension (but small compared to the grain diameter), may then transmit torques  $\mathbf{\Gamma}$ , which are limited <sup>2</sup> by an inequality, similar to (1.13):

$$\|\mathbf{\Gamma}\| \leq \mu_R N. \quad (1.14)$$

---

<sup>2</sup> $\mathbf{\Gamma}$  is a net torque at the center of the contact region itself. The contact force produces a torque at the center of the contacting grains, but not in the contact itself [55, 44].

By construction, the *rolling friction coefficient*,  $\mu_R$  is a length (of the order of the distance between contacting asperities).

In three-dimensional models, one should in general distinguish between rolling torque *stricto sensu*, for which  $\mathbf{\Gamma}$  is in the tangential plane, and *pivoting* (or *twisting*) torque, for which  $\mathbf{\Gamma}$  is normal to the contact. These different components may involve different “friction coefficients” (or lengths).

### 1.2.2 Contact networks and internal states of granular assemblies

We now recall some of the most useful variables describing the internal state of granular assemblies, and some of their important properties.

#### Stress tensor

The Cauchy stress tensor,  $\underline{\underline{\sigma}}$ , is related to microscopic variables in a granular sample by a useful formula [29], as follows.  $\Omega$  denoting the sample volume, it expresses  $\underline{\underline{\sigma}}$  as the sum of a kinetic term, involving velocities  $\mathbf{v}_i$  of the  $N$  grains,  $1 \leq i \leq N$  ( $\mathbf{v}_i$  is defined in the frame of reference of the center of mass of the whole system) contained in  $\Omega$ , and a second term involving contact forces  $\mathbf{F}_{ij}$  transmitted from grain  $i$  to grain  $j$  in all contacts, and  $\mathbf{r}_{ij}$ , the *branch vector*, pointing from the center of  $i$  to the center of  $j$ :

$$\underline{\underline{\sigma}} = \frac{1}{\Omega} \left[ \sum_{i=1}^N m_i \mathbf{v}_i \otimes \mathbf{v}_i + \sum_{i<j} \mathbf{F}_{ij} \otimes \mathbf{r}_{ij} \right]. \quad (1.15)$$

In quasistatic deformation, when the system is in mechanical equilibrium, the kinetic term vanishes and the stress tensor is given by the static term involving forces.

#### Coordination number

The coordination number  $z$  in a granular material is defined as the average number of force-carrying contacts per grain. If  $N_c$  is the number of force-carrying contacts between  $N$  grains, then the coordination number is  $z = 2N_c/N$  – as product  $zN$  counts each contact twice. One important constraint on  $z$  (with important consequences on mechanical properties of granular packings) that the community became aware of in the past 20 years is that it has an upper bound, in generically disordered systems, well below the values it may reach in ideal, regular arrangements like perfect crystals. Thus, disordered packings of spherical balls, in the limit of small contact deflections (rigid contact limit), satisfy [124, 100, 38, 1]

$$z \leq 6. \quad (1.16)$$

This is well below the value  $z = 12$  corresponding to ideal FCC or HCP lattices (or hybrids thereof), which represent the highest possible solid fraction,  $\Phi = \pi/(3\sqrt{2}) \simeq 0.74$  [7].

Some grains, in granular materials subjected to stresses from sample boundaries, do not carry any load and are referred to as *rattlers*. Depending on grain size distribution, density and assembling conditions, the proportion  $x_0$  of such rattlers in granular packings varies from a few percent to large values for some granular classes (e.g., small grains inside the interstitial voids of a force-carrying packed assembly of larger particles). The coordination number of the force-carrying structure (the sample from which rattlers are eliminated) is  $z^* = z/(1 - x_0)$ , and inequality 1.16 actually applies to  $z^*$  (a stronger constraint). On applying external forces to every grain, as in a material under gravity, one may identify a subset of grains which are shielded from the ambient stress level (e.g., not feeling the weight of the layers piled above): such grains are similar to the rattlers.



The origin of constraint (1.16) is a general property of disordered assemblies of rigid, *frictionless*, particles, in which the contact structure should be devoid of force indeterminacy (or hyperstaticity) [124]. As it is in fact a property of generically disordered geometries, it also applies to frictional grains – which most often have coordination numbers strictly below this upper bound [1], which tend to decrease for higher friction coefficients.

In equilibrated assemblies, a minimum value of  $z^*$  is necessary to maintain stability, which leads to

$$z^* \geq 4 \tag{1.17}$$

in packings of frictional spheres. Lower bound (1.17) is based on a simple counting argument (as many force components as there are equilibrium equations), assuming *mechanism motions*, or non-vanishing velocities (and angular velocities) such that relative motions of all contacting grain pairs consist in rolling without sliding, should not exist, because they would lead to instabilities (absence of velocity indeterminacy or “hypostaticity”<sup>3</sup>). This is apparently very nearly true in sphere packings (save for the role of 2-coordinated grains, see [1]). Values approaching lower bound (1.17) in assemblies of frictional spherical grains have only been reported in the limit of very large friction coefficients [1].

Coordination numbers, understandably, tend to increase with contact deflections under growing stress [87, 2], due to the closing of narrow gaps between neighbouring grains, and to decrease in out-of-equilibrium situations such as inertial flows [31], for which the contact network is strongly perturbed.

### Relation between pressure and average force

The coordination number might be used, in a system of spheres of diameter  $a$  in mechanical equilibrium, to write down a useful, exact relation between the average normal contact force,  $\langle F^N \rangle$  and the trace of the stress tensor, or the average pressure  $\mathcal{P} = \frac{1}{3} \text{tr} \underline{\underline{\sigma}}$ . Neglecting contact deflections, we might write  $\mathbf{r}_{ij} = a \mathbf{n}_{ij}$  in (1.15), and,  $\mathbf{n}_{ij}$  denoting the normal unit vector pointing in contact  $i$ – $j$ , the scalar product between force and branch vector is  $F^N \mathbf{n}_{ij} \cdot a \mathbf{n}_{ij} = a F^N$ . Upon replacing the sum over contacts by an average value and introducing the definitions of  $z$  and  $\Phi$  we obtain

$$\mathcal{P} = \frac{z\Phi}{\pi a^2} \langle F^N \rangle. \tag{1.18}$$

A generalized form of (1.18) is written in [118] for moderately polydisperse spheres.

### Force disorder

The smaller the coordination number and the degree of force indeterminacy, the greater the importance of packing geometry and the lesser the importance of contact laws in the determination of equilibrium forces. The bounded value of  $z^*$  and the relative sparsity of contacts is at the origin of the peculiar force patterns observed in granular materials, and most easily visualized in two dimensions. Experiments with photoelastic particles, initiated by Dantu [32], and also employed in some more recent studies [97, 86], exploit the birefringent properties of some material under stress to visualize the transmission of forces in 2D assemblies of parallel cylinders. The technique may enable quantitative analyses [6]. Fig. 1.4 displays a picture of photoelastic disks under oedometric compression, in which the brighter particles bear the stronger forces [86]. This strong force heterogeneity, characterized with the near alignment

---

<sup>3</sup>Isostaticity, or the simultaneous absence of force and velocity indeterminacy, is a remarkable property of force-carrying contact networks in equilibrated assemblies of (i) rigid, (ii) frictionless and cohesionless, (iii) spherical grains, holding in that case before both inequalities should be written with the same exact bound [124]. It does not apply in general if any one of conditions (i), (ii) and (iii) is not satisfied. Inequalities similar to (1.16), with adequate values of the upper bound, apply generally to frictionless grains.

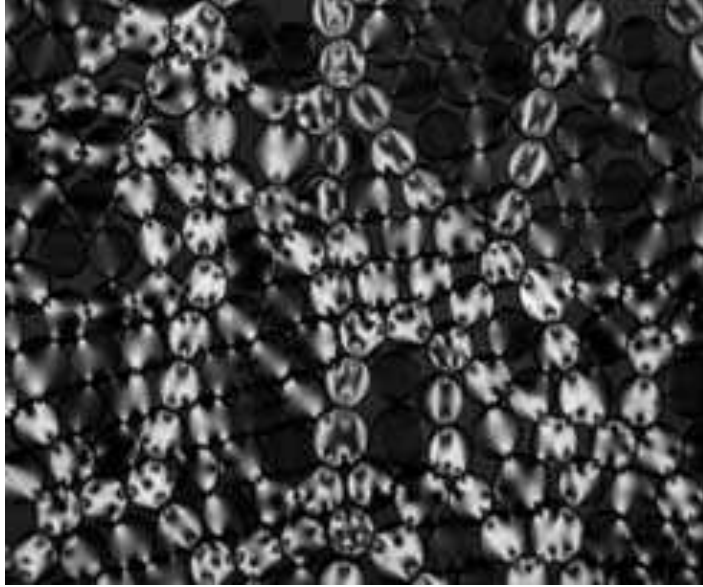


Figure 1.4: Force network in compressed disk assembly [86].

of the larger forces over lengths of several diameters, or *force chains*, hints that macroscopic mechanical properties are not easily obtained by averaging contact behaviour. Those patterns, and the corresponding distributions of force values, were also largely documented in numerical works [115, 114]. Fig. 1.5 displays a pattern of the force chains of a dry assembly of disks under isotropic compression, as obtained in simulations of an assembly of polydisperse disks.

Some probability distribution functions (pdf) of normal force component values are shown in Fig. 1.6. Those pdfs were measured in 3D simulations of sphere packings. The normal force  $f$  is normalized by the mean force  $\bar{f}$  [114]. The figure shows that the distribution of forces is very wide, with strong forces several times as large as the mean force observed with notable frequency. The distribution of the strong force network is often observed to decrease exponentially for large values [114, 139].

### Contact network and force anisotropies

In addition to the force intensity and its distribution, the orientation of the contact and forces have a significant influence on mechanical properties of granular material. The angular distribution of contacts is usually described with the probability distribution function  $E(\mathbf{n})$ , which determines the probability of finding a contact along the direction of unit vector  $\mathbf{n}$ . And the angular distribution of force intensities can be described with function  $\langle F \rangle_{\mathbf{n}}$ , which determines the average intensity of force in the direction of  $\mathbf{n}$ . The observations on the force network of sheared granular materials reveals the existence of anisotropy on the angular distributions of both contacts and forces (Fig. 1.7). The anisotropy of contact orientation is usually referred to as *structural* or *geometrical anisotropy* while the *mechanical anisotropy* refers to the force anisotropy. Many recent studies employed different mathematical approaches to investigate the anisotropy properties of granular materials and extract the mechanical properties from the characteristics of force networks [106, 8, 43, 111, 122]. Under deviatoric loads, the contact networks and the forces in granular materials adopt anisotropic distributions. In a triaxial or a shear test the anisotropy in the angular distribution of contacts and forces correlates with the anisotropy of stress. Fig. 1.7 illustrates the orientation and intensity of contact forces in simple shear tests under controlled normal stress [43]. The anisotropy is very conspicuous in

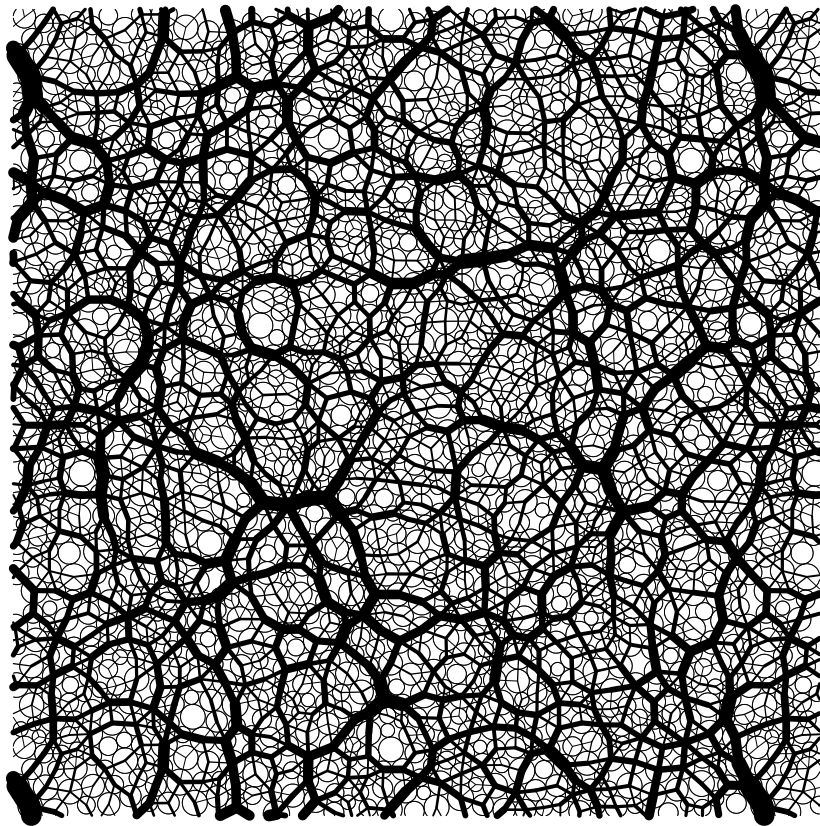


Figure 1.5: Force network in 2D simulation of dry granular assembly under isotropic load. The thickness of lines represent the intensity of normal forces. Note the rattlers and the periodic boundary condition.

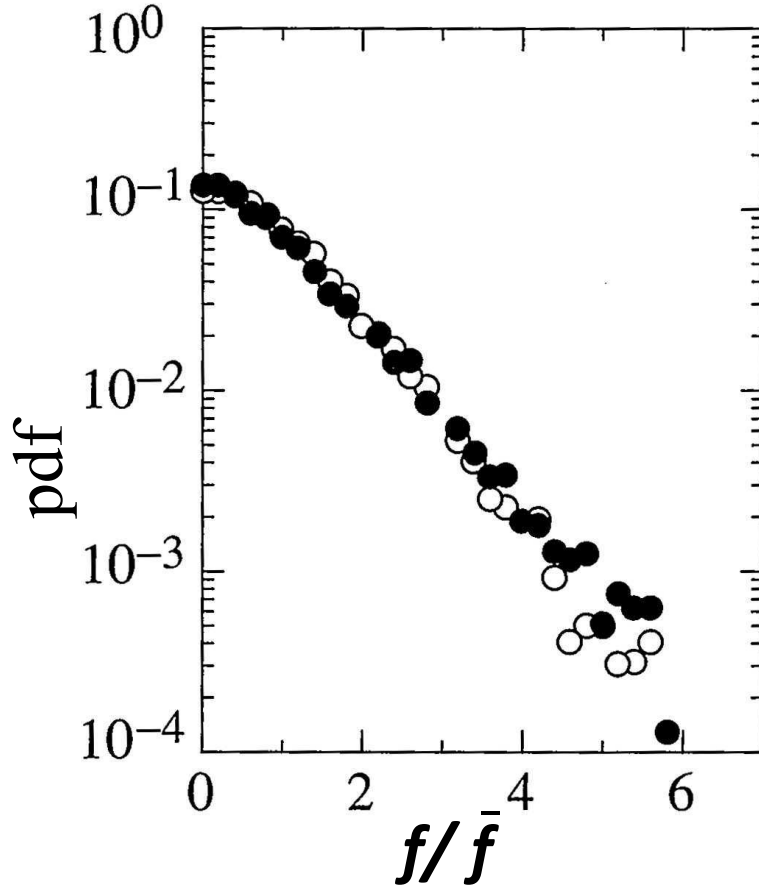


Figure 1.6: Distribution of normal contact forces in 3D packing simulation of spheres in equilibrium [114] for two different values of friction coefficient,  $\mu = 0.1$  (white symbols) and  $\mu = 0.4$  (black symbols). This figure is extracted from [6].

that case, especially for the stronger forces [115].

Structural anisotropies might be characterized by *fabric* tensors. The second rank fabric tensor is defined as the volume average of the dyadic product of contact normals[69] as

$$\underline{\underline{\mathbf{F}}} = \langle \mathbf{n} \otimes \mathbf{n} \rangle. \quad (1.19)$$

Different components of fabric tensors quantify the tendency of contacts to be preferentially oriented in certain directions. For example, in the plane shear flow of Fig. 1.7,  $F_{12}$  is negative (if axes  $x$  and  $y$  respectively oriented from left to right and from bottom to top on the figure), corresponding to a statistically favoured contact orientation at angle  $3\pi/4$  with respect to direction of flow  $x$ . The shear flow, on average, tends to create more contacts in this direction, for which the macroscopic strain corresponds to the largest compression; and the compression effect in existing contacts also tends to increase force values. These properties will be discussed in more detail in Sec.2.3.3, where we write down explicit relations between shear stresses and anisotropy parameters.

### 1.2.3 Cohesive and wet granular assemblies

#### Cohesive grains

Due to molecular interactions, a small attraction always exists between two macroscopic bodies of solid material [68]. The net force due to this effect becomes important when the size



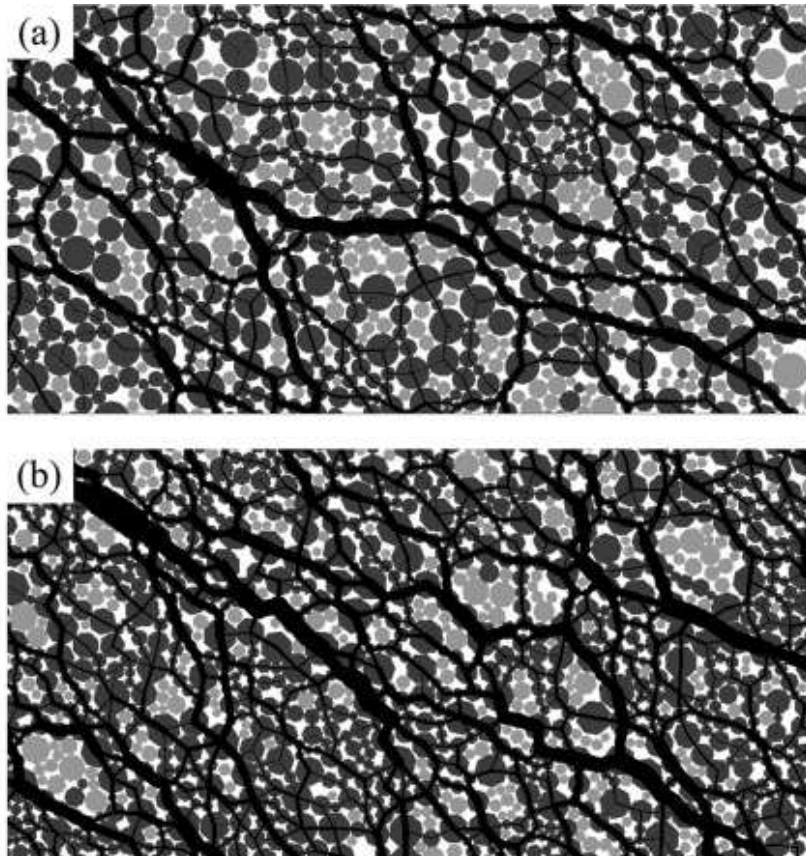


Figure 1.7: Snapshots of the force network under shear in (a) a system composed of disks with rolling friction ( $\mu_r = 0.05$ ) and (b) a system composed of octagonal particles. The line thickness is proportional to the normal force (from [43]).

of particles is small enough (e.g., in the micron range) and their range is limited to molecular scales (nanometers). Such cohesion forces, sometimes referred as adhesive forces [6], are the origin of macroscopic cohesion in some materials, such as clays and powders. Several approaches have been used to calculate the adhesive force between macroscopic bodies [83, 71, 35]. Based on a simple energy balance, the adhesive force between two elastic spheres of radius  $R$  in vacuum can be expressed as [6]:

$$F_{adh} = 2\pi\gamma_s R,$$

in which  $\gamma_s$  is the surface energy of the solid in vacuum. This approximation shows that the adhesive force is proportional to the radius and surface tension of the particles. More accurate calculations show that this force is different for soft and rigid particles. The DMT model, proposed by Derjaguin *et al.* [35], confirms the above approximation for the adhesive force between two rigid spheres, while the JKR model suggests  $(3/2)\pi\gamma_s R$ , for soft spheres [71]. In the presence of asperities of micrometric scale, because of the nanometric range of adhesive forces, some asperity size, instead of the particle diameter, should determine  $F_{adh}$  [26, 48].

### Capillary forces

A liquid wetting the grains, if present as a small quantity in the intergranular voids, will preferentially accumulate near the contacts or the narrow interstices, forming liquid bridges that join contacting grains or near neighbours. The formation of those bridges, assuming the

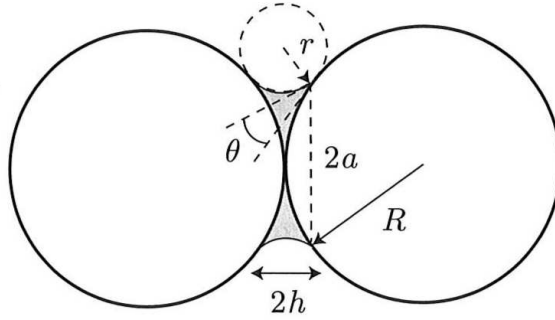


Figure 1.8: Schematic view of two smooth spheres with radius  $R$ , interacting through a liquid bridge (from [6]).

form of the meniscus shown in Fig. 1.8, may be spontaneous if the liquid has exchanges with its vapour, present in the surrounding atmosphere. According to the Young-Laplace law [80], the pressure difference between the two sides of a curved liquid-vapour or liquid-void interface is determined by the surface tension  $\Gamma$  and principal radii of curvature  $R_1$  and  $R_2$  as

$$p_i - p_e = \Gamma \left( \frac{1}{R_1} + \frac{1}{R_2} \right), \quad (1.20)$$

the radii being positive if region  $i$  (at pressure  $p_i$ ) is inside the curvature, region  $e$  (at pressure  $p_e$ ) outside. In the case of the capillary bridge near the contact point of two spheres with radius  $R$ , shown in Fig. 1.8, assuming the principal radii of curvature are by  $a$  and  $r$ , defined on the figure, one should have, for the pressure inside the meniscus, relative to the outside, atmospheric pressure:

$$P = \Gamma \left( \frac{1}{a} - \frac{1}{r} \right). \quad (1.21)$$

As the diameter  $a$  of the meniscus is much larger than its meridian radius of curvature  $r$ ,  $P$  is negative. The liquid is sucked towards the contact region. Angle  $\theta$  is the equilibrium contact angle between the liquid and the grain surfaces. For perfectly wettable materials, this contact angle is zero.

The capillary force between spheres in Fig. 1.8 is approximately equal to the suction force  $\pi a^2 P$ . Assuming  $a \gg r$ , the pressure difference is given by  $\sim -\Gamma/r$ . Since the meniscus compared to the grain size is small, one may also assume  $h \ll R$  ( $2h$  is the distance between grain surfaces) and then we have  $r \sim h/\cos\theta$ . Finally with the help of the geometrical relation  $a^2 \simeq 2hR^2$  we obtain the following expression,

$$F_{\text{cap}} \simeq 2\pi\Gamma R \cos\theta. \quad (1.22)$$

showing that the capillary force between two spheres in contact is proportional to surface tension  $\Gamma$  and particle radius  $R$ , but is remarkably independent of the volume of meniscus  $V$ . It should be mentioned here that the effect of gravity on the curvature of the liquid bridge and on the capillary force is negligible when the grains are small enough. The capillary length  $l_c$  determines the length scale above which gravity plays a significant role in the capillary force. It is defined as  $l_c = \sqrt{\Gamma/g\rho}$ , where  $g$  is the gravitational acceleration and  $\rho$  is the density of the liquid. For water  $l_c \approx 2.7$  millimeters.

To go beyond this first estimate of the capillary force, one needs to find the exact shape of the meniscus, as a constant curvature surface (so that the liquid is at constant pressure). On writing down (1.21), we already implicitly resorted to the *toroidal approximation*, which assumes the bridge profile is a circular arc in a meridian plane. The resulting force by this

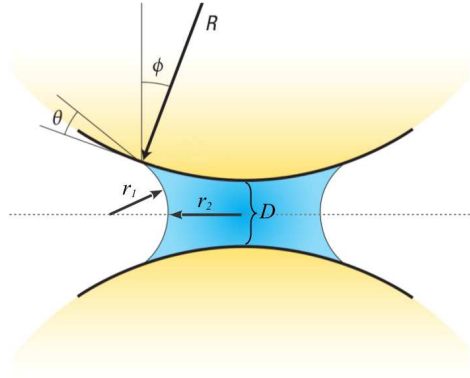


Figure 1.9: Liquid bridge between two spheres.

approximation can be calculated either on defining radius  $a$  as the distance of the triple line to the axis of revolution, or using the gorge (neck) radius of the bridge. The gorge method appears to be more accurate, with a relative error below 10% compared to exact numerical solutions [82] – an acceptable accuracy in practice. The capillary force between two spheres of radius  $R$  at distance  $D$  is given by the sum of two terms, calculated at the neck of the liquid bridge: first, the attractive force due to axial surface tension  $\Gamma$ , and, secondly, the hydrostatic force due to capillary pressure  $P$ . It is given by [82, 108]

$$F_{\text{Gorge}} = \pi r_2^2 \Delta P + 2\pi r_2 \Gamma = \pi \Gamma r_2 \left[1 + \frac{r_2}{r_1}\right], \quad (1.23)$$

in which  $r_1$  and  $r_2$ , respectively denoting the radius of the meridian profile and the radius at the neck (Fig. 1.9) are given by

$$\begin{cases} r_1 &= \frac{D/2 + R(1 - \cos \varphi)}{\cos(\varphi + \theta)}, \\ r_2 &= R \sin \varphi - [1 - \sin(\varphi + \theta)]r_1. \end{cases} \quad (1.24)$$

The filling angle  $\varphi$  cannot be calculated explicitly and an iterative procedure must be used to calculate it as a function of the other parameters. A simpler but less accurate expression is proposed by Maugis [89], by which the capillary force is expressed as a function of the meniscus volume  $V$  and the separation distance  $D$  as below,

$$F^{\text{Cap}} = 2\pi \Gamma R \cos \theta \left[1 - \frac{1}{\sqrt{1 + \frac{2V}{\pi R D^2}}}\right]. \quad (1.25)$$

Fig. 1.10 compares the result of the toroidal approximation and the Maugis approximation with a parametrized form of the numerical solution as proposed by Soulié *et al.* [141]: ,

$$F^{\text{Cap}} = \pi \Gamma R \left(C + \exp\left(A \frac{D}{R} + B\right)\right), \quad (1.26)$$

with

$$\begin{cases} A &= -1, 1(V^*)^{-0.53} \\ B &= (-0.148 \ln(V^*) - 0.96)\theta^2 - 0.0082 \ln(V^*) + 0.48 \\ C &= 0.0018 \ln(V^*) + 0.078 \end{cases} \quad (1.27)$$

in which  $V^* = V/R^3$ .

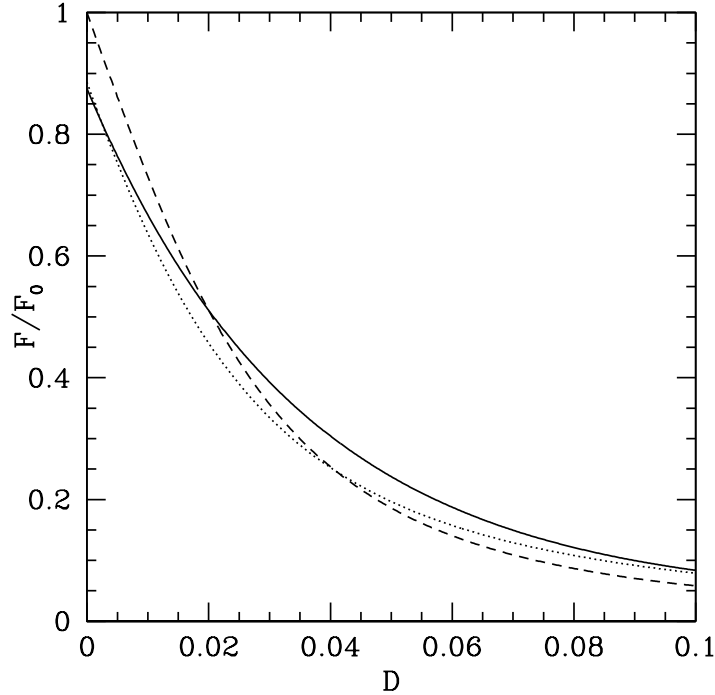


Figure 1.10: Capillary forces predicted by the Maugis formula (dashed line, and the toroidal approximation (solid line) compared to the accurate Soulié formula (dotted line), for meniscus volume  $V = 10^{-3}a^3$ .

Those solutions are only valid, for given volume  $V$ , as long as  $D$  does not exceed a rupture distance  $D_{\text{rup}}$  [63], given by

$$D_{\text{rup}} = \left(1 + \frac{\theta}{2}\right)(V^{1/3} + 0.1V^{2/3}). \quad (1.28)$$

An experimental study by Pitois *et al.* [108] shows that the rupture distance also varies with the separation velocity.

Another important feature of capillary forces due liquid bridge is the existence of a *hysteresis* in liquid bridge formation, that is to say, the liquid bridge between particles forms just after that they come into contact, but it pinches off when a certain finite separation,  $D_{\text{rup}}$ , is reached [63].

#### 1.2.4 Wet granular materials

Adding a small amount of water to a granular material strongly affects its mechanical properties, such that it can be sculptured into quite stable structures, for instance a sand castle. Even the humidity in the atmosphere may cause tiny liquid bridges to form at the contact points between particles. The particles connected with a liquid bridge attract each other by capillary force. For real particles, when due to asperities on their surfaces, the molecular interactions scale down to small adhesive forces, the capillary forces are large and dominant. Unlike nano-scale ranged adhesive forces, they can apply from an interparticle distance of the order of the particle size. Such unique properties of capillary interactions lead to significant changes in mechanical properties of granular materials in the presence of the liquid in their interstitial spaces. It is well known that the mechanical properties of wet granular materials depends on the amount of liquid in the system. Based on the liquid content, wet granular materials classify in different regimes [95, 76]:





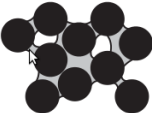

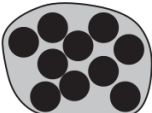
Liquid content	State	Schematic diagram	Physical description
No	Dry		Cohesion between grains is negligible.
Small	Pendular		Liquid bridges are formed at the contact points of grains. Cohesive forces act through the liquid bridges.
Middle	Funicular		Liquid bridges around the contact points and liquid-filled pores coexist. Both give rise to cohesion between particles.
Almost saturated	Capillary		Almost all the pores are filled with the liquid, but the liquid surface forms menisci and the liquid pressure is lower than the air pressure. This suction results in a cohesive interaction between particles.
More	Slurry		The liquid pressure is equal to, or higher than, the air pressure. No cohesive interaction appears between particles.

Figure 1.11: Schematic diagrams for classification of wet granular materials with various amount of liquid. The black circles represent the grains and the grey region represent the interstitial liquid (from [95]).

- **Pendular state:** When a small amount of liquid is added to the granular material, the liquid initially collect near the contact point of particles, and a three phase system composed of liquid, solid and interstitial fluid, forms. In this regime the liquid content is as large as the liquid bridges form without any coalescence of menisci and the capillary forces are limited to pair-wise interactions.
- **Funicular state:** As the liquid content is increased further, the neighbour liquid bridges start to coalesce. The liquid fills some pores and multiple grains can be in contact with a volume of liquid.
- **Capillary state:** At higher values of liquid content most of the pores fill with liquid and large contiguous wet clusters forms.
- **Slurry state:** In this regime all the pore space are fully saturated and the particles are completely immersed in the liquid.

Fig. 1.11 schematically displays different states of wet granular materials. The capillary force in the first 3 regimes is important while it is negligible in the slurry state. Here, in this dissertation, we only focus on the properties of wet granular materials in the pendular state.

### The role of roughness

Eq. 1.22 shows that the capillary force between two spheres in contact is independent of the volume of meniscus. However, this relation is obtained for smooth particles and in the presence of the surface roughness the capillary force varies with the volume of the liquid

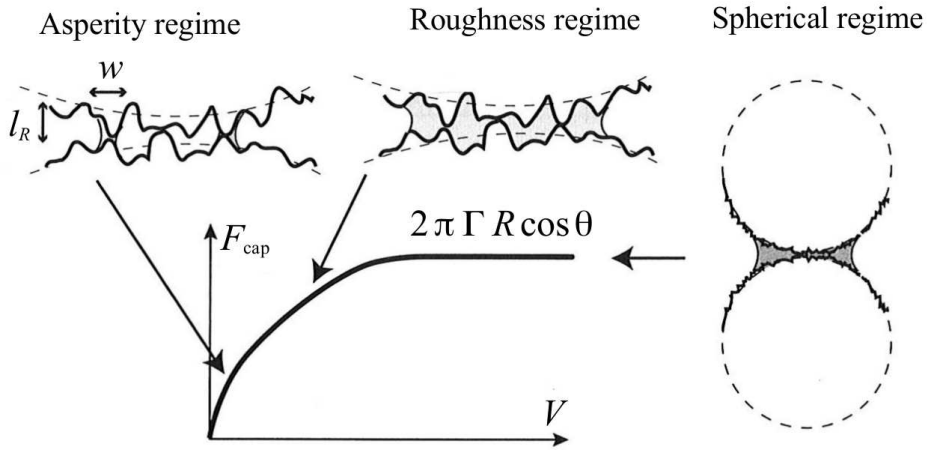


Figure 1.12: Different regimes of roughness and the variations of capillary force  $F_{\text{cap}}$  with the Volume of liquid  $V$  in different regimes (from [6]).

bridge. For very small liquid contents, it is obvious that before a liquid bridge forms, the crevices on the grain surface must first be filled. In respect of the meniscus volume and the size of the asperities, the capillary force may be classified in three different regimes [59, 63, 6], as illustrated in Fig. 1.12.

The roughness can be characterized with its amplitude  $l_R$ , a typical lateral scale  $w$  and the roughness exponent  $\chi$ , with  $0 < \chi \leq 1$ . The first regime called *asperity regime*, corresponds to very small liquid volumes,  $V < l_R w^2$  ( $h < l_R$ ), when only micro-capillary bridges form between asperities. The capillary force in this case is given by,

$$F^{\text{Cap}} \sim \frac{\Gamma w^2}{l_R} \left( \frac{V}{l_R w^2} \right)^{\frac{2-\chi}{2+\chi}}. \quad (1.29)$$

For rough surface where  $\chi \rightarrow 1$ , the capillary force is proportional to the cubic root of the meniscus volume. Larger liquid volume (or equivalently when  $\chi \rightarrow 0$ ) correspond to the *roughness regime*, in which the interstitial space is filled with liquid, but the volume is still so small that the curvatures of the particles play no role. Then the capillary force will be proportional to the volume as

$$F^{\text{Cap}} \sim \frac{\Gamma V}{l_R^2}. \quad (1.30)$$

Finally for still larger liquid volumes  $V > l_R^2 R$  ( $h > l_R$ ), the *spherical regime* is obtained: the lateral extent of the liquid is large so that the microscopic curvature of the particle becomes important and the surface roughness becomes negligible. The capillary force in this regime is correctly predicted by Eq. 1.22.

### Liquid content, limit of pendular state

Depending on the amount of the liquid in the system, and on its resulting spatial distribution, wet granular materials are classified in different states. Different definitions for the liquid content are possible. Some authors use the liquid volume fraction or  $V_l/\Omega$  (the total volume of liquid,  $V_l$ , divided by the total sample volume  $\Omega$ ) [63, 74]. With  $N_b$  liquid bridges of volume  $V$ , between  $N$  particles of diameter  $a$ , the coordination number of liquid bridges is  $z = 2N_b/N$  and the solid fraction is  $\Phi = \pi N a^3/6\Omega$ . Then the liquid content  $W$  is given by

$$W = \frac{V_l}{\Omega} = \frac{3z\Phi V}{\pi a^3} \quad (1.31)$$

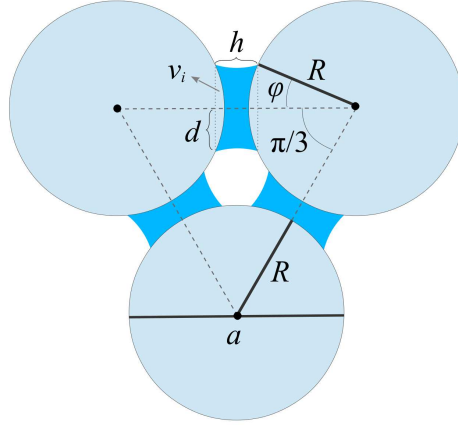


Figure 1.13: Three spheres connected with liquid bridges. They do not intersect as long as filling angle  $\varphi$  is smaller than  $\pi/6$ .

Other publications (see e.g., [118]) define the liquid content in terms of masses. It is also possible [95, 130] to use saturation  $S_w$  instead of liquid content. Saturation is defined as the ratio of the liquid volume to the total pore volume and is simply related to liquid content as  $S_w = W/(1 - \Phi)$ .

To estimate the minimum liquid content required for liquid bridge formation, we should consider that the maximum amount of liquid which can be stored in asperities of a particle is about  $4\pi R^2 l_R$ . Therefore, for a typical value of the roughness amplitude  $l_R \approx 500$  nm and a typical value of the particle diameter  $a = 500$   $\mu\text{m}$ , the volume of liquid bridge should be larger than  $1.6 \times 10^{-3} a^3$ . With the help of Eq. 1.31 and the typical values  $z = 6$  and  $\Phi = 0.5$ , the lower threshold of liquid content in the pendular state is about  $5 \times 10^{-3}$ . However, by the experimental measurements [63], for the same values of the roughness amplitude and particle size, it is determined to be  $W_{\min} = 7 \times 10^{-4}$ , which is smaller than our estimation.

The upper threshold of the liquid content in the pendular regime, as menisci start to coalesce, might also be estimated, as follows. Fig. 1.13, in which the closest possible menisci on one common spherical grain are depicted, shows that the filling angle  $\varphi$  should be smaller than  $\pi/6$ . The volume of the liquid is approximately the volume of a cylinder with radius  $d$  and height  $h$ , excluding two small volumes  $v_i$ . For contacting particles so far,  $h = 2R(1 - \cos \varphi)$ , and so

$$\begin{aligned} V &= \pi d^2 h - 2v_i, \\ &= \frac{2\pi R^3}{3} (2 \cos^3 \varphi - 3 \cos^2 \varphi + 1). \end{aligned} \quad (1.32)$$

So the volume of the meniscus when  $\varphi = \pi/6$  is about  $10^{-2} a^3$ , which yields  $W_{\max} \approx 0.03$ . A similar value for the upper limit of liquid content in the pendular state is determined by experiments [63].

## Mechanical properties of wet granular materials

Capillary cohesion is known to strongly influence the strength and flow properties of granular materials. It is observed in many numerical and experimental studies that in the presence of small amount of an interstitial liquid, the yield stress of the material strongly increases. The experiments reported by Fournier *et al.* [50] on sheared granular materials over a wide range of liquid content  $W$  (Eq. 1.31) show that the shear strength rapidly increases as  $W$  is increased from zero, and approaches a maximum for  $W \approx 10^{-3}$ , which coincides with the transition from asperity regime to spherical regime (see Sec. 1.2.4). The shear strength

remains nearly constant for larger saturations, up to  $W \approx 0.04$ , close to the transition to the funicular state. It decreases for larger values of  $W$  and finally goes to zero at  $W \approx 0.35$  [50].

The influence of water content on unsaturated granular materials is mostly studied through the Coulomb cohesion parameter which represents the shear strength at zero confining pressure (see Eq. 1.1). Richefeu *et al.* [118] studied the Coulomb cohesion in pendular state, both numerically and experimentally, for different values of liquid content. They observed that the Coulomb cohesion increases with liquid content and saturates to a maximum value. A constant value of friction angle  $\varphi (= \tan^{-1} \mu^*)$ , about  $33^\circ$  is reported, regardless of the level of liquid content.

In soil mechanics, mechanical properties of water-saturated soils are usually described with the help of the *effective stress* concept, originally proposed by Karl von Terzaghi [147]. Terzaghi’s principle states that “all measurable effects of a change of stress of the soil, that is compression, distortion and change of shearing resistance, are exclusively due to changes in the effective stress.” [99]. The effective stress is defined as

$$\sigma'_{ij} = \sigma_{ij} - u_w \delta_{ij}, \quad (1.33)$$

with  $u_w$  the pore water pressure and  $\delta_{ij}$  Kronecker’s delta. This principle was extended to unsaturated soils by Bishop [13] as

$$\sigma'_{ij} = (\sigma_{ij} - u_a \delta_{ij}) + \chi(u_a - u_w) \delta_{ij}, \quad (1.34)$$

in which  $u_a$  is the pore air pressure and  $\chi$  is the effective stress parameter attaining a value of one for saturated soils and zero for dry soils. Such models are based on regarding the capillary force effect as an isotropic pressure. However, recent studies by Scholtès *et al.* [131, 130] show that this assumption is not valid. These authors numerically simulated the triaxial compression of unsaturated granular materials. In these studies, the components of the stress tensor are split into two terms: the contributions of contact forces  $\sigma_{ij}^c$  (effective stress), and an isotropic stress due to capillary interactions  $\sigma_{ij}^{\text{cap}}$ , assuming an isotropic distribution of liquid bridges in the material. The additive influence of capillary forces in stress tensor is verified for an initial isotropic configuration, although deformation creates a slight anisotropy in liquid bridge distribution. Consequently, the contribution of capillary forces to the total stress is not an isotropic pressure, which is not consistent with the Bishop form of the effective stress, or any expression ignoring the deviatoric effect of the forces in liquid bridges.

The significant influence of the hydraulic hysteresis on the mechanical behaviour of wet granular materials is reported in a recent publication by Shamy & Gröger [40]. They numerically studied the shear flow of wet granular material, during the wetting and drying stages. In a wetting stage, as the saturation increases from low to high levels, liquid bridges only form between particles in contact. But in a drying stage, the liquid bridges are already present between particles, which are not necessarily in contact. They observed a different material response for equal saturations on the imbibition and on the drainage curves, thereby showing the important role of hydraulic hysteresis on rheological properties of unsaturated soils.

Mani *et al.* [88] have studied the liquid migration within the shear band in a wet granular material in pendular state. Both experimentally and numerically, they showed that the liquid content decreases within unsaturated shear bands, contrary to what have been seen in saturated materials. This effect may be important in shearing tests, since the fluid depletion in shear bands may strongly decrease the shear strength of the material.

### 1.3 Discrete simulations of granular materials (DEM)

First proposed by Cundall and Strack [30] by adapting the molecular dynamics simulation method, initially developed for molecules [5], to assemblies of solid grains, the “discrete ele-

ment method” (or DEM) is based on the integration of the equation of motion simultaneously for all grains. The kinematics of the grain is that of a collection of rigid bodies, each of them with six degrees of freedom in 3D, and the corresponding equations for the linear and angular momentum balance involve the contact forces, as modeled in Sec. 1.2.1, and their moments. While the grains have the kinematics of rigid, undeformable objects, they might slightly deform at their contacts, as described in Sec. 1.2.1. Implementations of DEM or molecular dynamics are described in a number of treatises [5, 116, 109], in which various numerical integration schemes are proposed, and technical issues, such as the choice of an appropriate time step, are discussed.

Instead of a complete presentation of the method, we introduce here some specific procedures, among the less often described in the literature, that will prove useful for our specific study, and that we find useful to explain and illustrate (Sec. 1.3.3). We also recall the complete list of dimensionless control parameters in the simulations carried out in order to probe the material constitutive laws (Sec. 1.3.2), and their known influence (or absence thereof, according to the investigated rheological regime), thereby justifying our own choices implemented in the forthcoming chapters.

### 1.3.1 Some characteristic material states

#### Critical state

DEM computations have successfully reproduced the approach to the critical state, an “attractor” to which stress and density curves originated from initial configurations of different solid fraction all converge in triaxial compression (Fig. 1.14), or in simple shear tests [113]. Many results have now accumulated on the properties of the critical state for various systems.

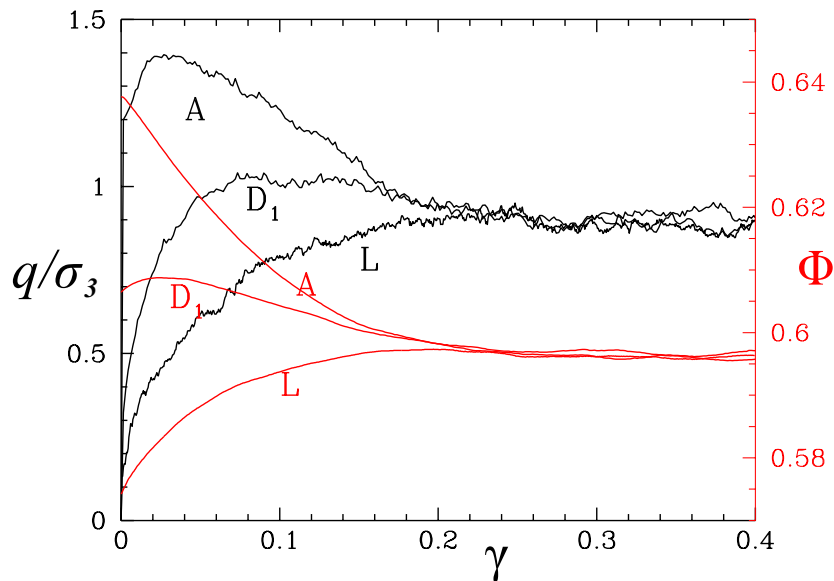


Figure 1.14: DEM simulation of triaxial compression test on spherical bead assemblies. Solid fraction and deviatoric stress as functions of axial strain for different initial states. Note the different scales on left (deviator) and right (solid fraction) vertical axes.

For instance, it is known [81] that the macroscopic friction coefficient  $\mu^*$  in the critical state is larger than its microscopic, intergranular analog  $\mu$  for small  $\mu$  (in particular,  $\mu^* \simeq 0.1$  for  $\mu = 0$  in bead packs [104]), but reaches, as a function of  $\mu$ , a plateau, near  $\mu = 0.4$  ( $\mu^* \simeq 0.35$ ).

Remarkably [113, 123], the critical state is also defined in terms of internal variables (coordination number, fabric...).

### Loose configurations of adhesive particles.

Adhesive particles tend to form tenuous aggregates, which may support some confining stress, as illustrated for a 2D model [54] in Fig. 1.15. It is also observed that the equilibrated

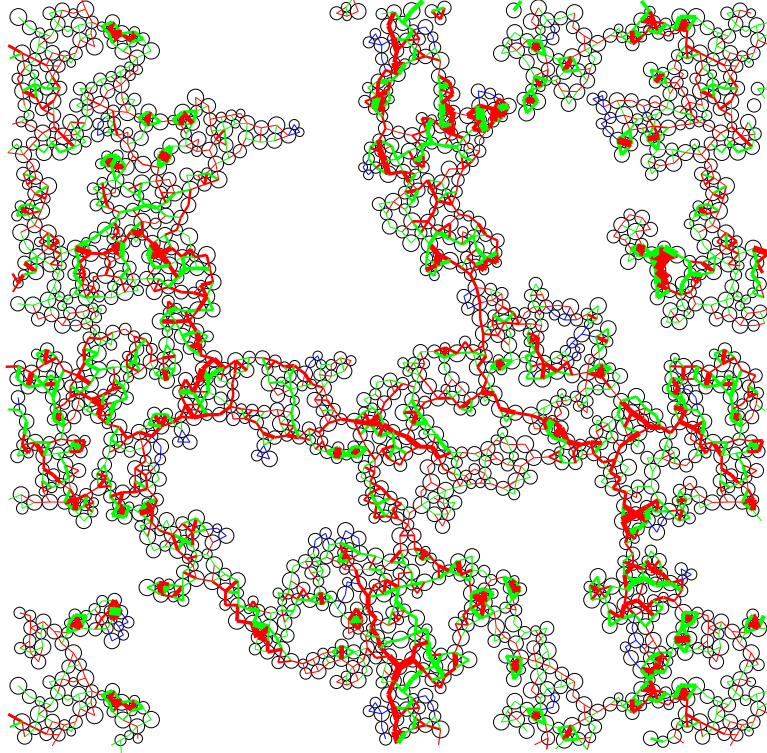


Figure 1.15: Loose cohesive assembly of disks, from [54]. Forces are encoded as line thickness, with compressive ones in red, tensile ones in green. Blue lines mean that the normal contact force is equal to zero (by compensation of adhesion and elasticity).

configurations of cohesive packing are sensitive to the applied pressure  $P$ , relative to the maximum adhesive contact force  $F_0$  (tensile strength) [54]. Defining the dimensionless number *reduced pressure*,  $P^* = Pa/F_0$ , structures like the one of Fig. 1.15 are stable for very small  $P^*$ . Note the striking difference with Fig. 1.5. They collapse on increasing the pressure, and satisfy constitutive relation (1.5) in some pressure range [55].

### 1.3.2 Dimensional analysis

The list of parameters governing rheological characterization tests in granular materials generally comprises, in addition to the material parameters, some pressure (or confining stress)  $P$  and a shear rate (or some other strain rate),  $\dot{\gamma}$ . These combine with particle diameter  $a$ , mass  $m$ , interparticle friction coefficient  $\mu$ , restitution coefficient  $e$  (or damping coefficient  $\zeta$ ),



contact stiffnesses ( $K_N$  and  $K_T$ ), tensile strength  $F_0$  of cohesive grains (we assume gravity can be neglected). Dimensional analysis provides a convenient approach to characterize the material behaviour with only a few dimensionless parameters.

$\mu$ , and  $\zeta$  or  $e$ , are already dimensionless. While friction coefficient  $\mu$  has a significant influence on the rheological properties of the material, the coefficient of viscous dissipation  $\zeta$ , which is related to restitution coefficient  $e$ , is observed to have negligible influence on the properties of dense flows [31, 104]. In addition to those parameters, by dimensional analysis, the mechanical properties of a granular system, subjected to a shear rate  $\dot{\gamma}$ , and normal stress  $P$ , depends only on 2 (or 3 in the presence of cohesive forces) more dimensionless numbers [127].

### Stiffness number

The importance of contact deformation is characterized by *stiffness number*  $\kappa$ . Comparing normal stiffness  $K_N$  to the stress level  $P$ , it is defined such that the average contact deflection  $h$ , in contacts, satisfies [109, 126],

$$h/a \sim \kappa^{-1} \quad (1.35)$$

Since the average normal force in the contact of spherical particles is proportional to  $Pa^2$ , for the Hertzian law (Eq. 1.7) we obtain,

$$\kappa = \left( \frac{\tilde{E}}{P} \right)^{2/3}. \quad (1.36)$$

The limit of  $\kappa \rightarrow +\infty$  corresponds to rigid grains, for which the material properties should not depend on  $\kappa$  any more. In this limit, the small deflections at contacts, of the order of  $\kappa^{-1}a$ , do not significantly modify the structure of the granular assembly in comparison to one composed of ideally rigid grains. Practically  $\kappa \gtrsim 10^4$  might be considered to be stiff enough, while a value of the order of  $10^2$  is too small.

### Inertial number

The *inertial number*,  $I$ , characterizes the importance of inertial effects in a dense granular flow [67, 52, 31]. It is defined as the ratio of the inertial time  $\sqrt{m/aP}$  (the time needed for a particle of mass  $m$ , accelerated by force  $Pa^2$ , to move on a distance  $a$ ) to the shearing time  $\dot{\gamma}^{-1}$ , as [109]

$$I = \dot{\gamma} \sqrt{\frac{m}{aP}} \quad (1.37)$$

The inertial number provides a classification of flow regimes. For very small values of  $I$ , when  $I \rightarrow 0$ , we approach the quasistatic regime. Large values  $I \gtrsim 1$  correspond to agitated, “gaseous” regime and the inertial regime lies in between [6]. (Some authors use other equivalent expressions, e.g., Savage or Coulomb number  $\rho a^2 \dot{\gamma}^2 / P$  (with particle density  $\rho$ ), which is simply  $I^2$  [6]).

### Reduced pressure

The reduced pressure  $P^*$ , as already mentioned in connection with Fig. 1.15, characterizes the intensity of adhesion forces compared to confining forces, and for 3 dimensional systems is defined as [109]

$$P^* = \frac{Pa^2}{F_0}, \quad (1.38)$$

in which  $F_0$  is a force scale for the intensity of adhesive forces (usually maximum attractive force). Typically for surface tension of water  $\Gamma_w = 73 \text{ mJ/m}^2$ , particle diameter  $a = 0.1 \text{ mm}$

and the atmosphere pressure, one gets  $P^* = 43.6$ .  $P^* \rightarrow +\infty$  corresponds to cohesionless systems, and when  $P^* \gg 1$ , the confining forces are dominant and the effects of cohesive forces are negligible. In the case  $P^* \ll 1$ , the cohesion forces dominate, which may strongly affect the material properties. The stiffness number for Hertzian contacts should then be determined by replacing the typical force  $Pa^2$  by  $F_0$  [109], thereby defining:

$$\kappa_0 = \left( \frac{\tilde{E}a^2}{F_0} \right)^{2/3} = \kappa P^{*2/3}. \quad (1.39)$$

Similarly, instead of inertial number  $I$ , the effect of inertia could be characterized by [109]:

$$I_a = \dot{\gamma} \sqrt{\frac{ma}{F_0}}. \quad (1.40)$$

### Influence of dimensionless control parameters, in different regimes.

	$I$	$\kappa (> 10^3)$	$e$ or $\zeta$	$\mu$	$\mu_R/d$	$P^*$
Assembling process	Y	N	Y	Y	Y	Y
Solid, strain type I, $I < 10^{-3}$	N	Y	N	Y	Y	Y
Solid, strain type II, $I < 10^{-3}$	N	N	N	Y	Y	Y
Critical state, $I < 10^{-3}$	N	N	N	Y	Y	Y
Dense flows, $10^{-3} < I < 0.1$	Y	N	N	Y	Y	Y
Collisional regime, $I > 0.1$	Y	N	Y	Y	Y	Y

Table 1.1: Influence of the dimensionless parameters on the mechanical behaviour in different regimes. (Y=Yes, N=No)

Table 1.1 (extracted from [126, 127]) sums up the state of the art on the rheological regimes for which parameters influence the material behaviour. It is based on numerical results obtained with 3D sphere assemblies or 2D disk systems, with limited polydispersity. While the influence of  $\kappa$ , if large enough, is limited to a certain regime of small strains (of type I, i.e., due to contact deflections, as opposed to type II, due to network rearrangements [128]), and restitution coefficients mainly affect the strongly agitated flows (as in granular gases, but also in the assembling stage), parameters  $\mu$ ,  $I$  and  $P^*$  are the ones governing dense flows.

### 1.3.3 Implementation of DEM for plane shear flow

The simplest geometries to study granular material rheology is the plane shear flow. Consider a granular material confined between two rough plates (Fig. 1.16). The flow of the material can be obtained by imposing a constant shear rate  $\dot{\gamma} = v_1/L_2$ , or a constant shear stress  $\tau \equiv \sigma_{12}$  on the top plate. Most literature results were obtained on imposing the wall velocity and measuring the shear stress [4]. Some are carried out controlling the shear force applied to the moving wall in order to study the flow thresholds [149]. We will see that it is more convenient to control the pressure [6, 31],  $P \equiv \sigma_{22}$ , onto the top plate and second and measure solid fraction  $\Phi$ , rather than keeping the volume constant [22]. To exploit fully the ability of the simulation set-up to achieve arbitrary large shear strains, it is convenient to use periodic boundary conditions in the direction of the flow, and in the transverse (vorticity) direction. Furthermore, the wall effects might be entirely suppressed, if the system is also periodic in the direction of the velocity gradient.



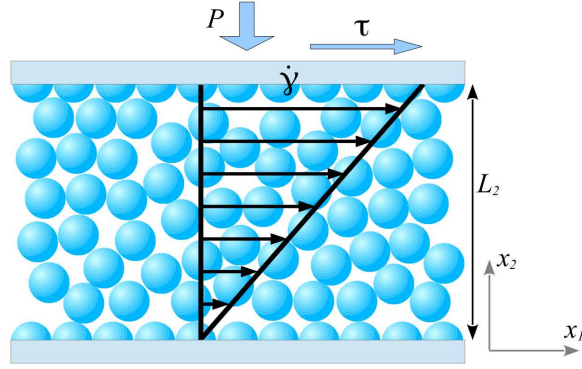


Figure 1.16: Plane shear flow.

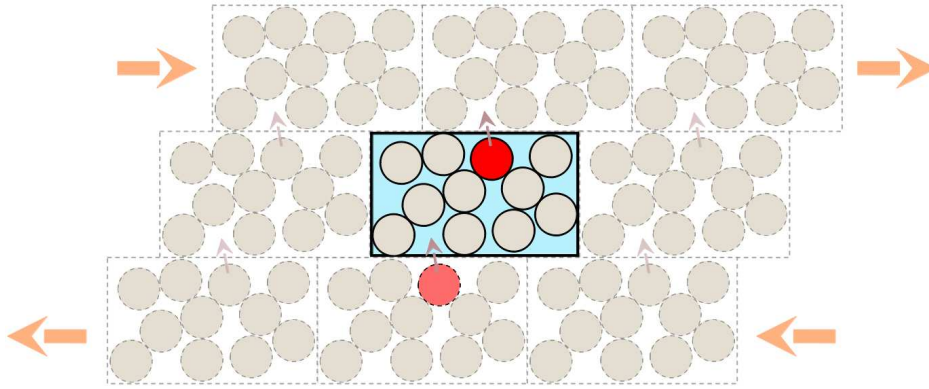


Figure 1.17: Sketch of Lees-Edwards boundary condition. Main cell is surrounded by its copies.

### Boundary condition and stress control

The *Lees-Edwards* periodic boundary condition, as illustrated in Fig. 1.17, uses a rectangular parallelepiped simulation cell that does not get distorted in the shear flow. Among the periodic replica of the central cell, those that are immediately above or below, along axis  $x_2$ , move with velocity  $\pm\dot{\gamma}L_2$  relative to the main cell, and the resulting shift along direction 1 should be taken into account as particles enter or leave the central cell (Fig. 1.17).

In order to control normal stress  $\sigma_{22} = P$  the size of the box in the same direction,  $L_2$ , should be allowed to vary. One method, used in [1, 104], inspired by the Parrinello-Rahman molecular dynamics scheme [103], is the following. Lengths  $L_1$  and  $L_3$  of cell edges parallel to velocity direction and vorticity, are kept constant. Position vectors  $\mathbf{r}_i$  of particle centers are written as

$$(1 \leq i \leq N) \quad \mathbf{r}_i = \underline{\underline{\mathbf{L}}}\cdot\mathbf{s}_i, \quad (1.41)$$

in which  $\underline{\underline{\mathbf{L}}}$  is a square  $3 \times 3$  diagonal matrix with diagonal components  $(L_1, L_2, L_3)$ , and  $\mathbf{s}_i$  is the rescaled position vector in a cubic box with unit edge lengths.

$$(1 \leq i \leq N) \quad \mathbf{v}_i = \underline{\underline{\mathbf{L}}}\cdot\dot{\mathbf{s}}_i + \dot{\underline{\underline{\mathbf{L}}}}\cdot\mathbf{s}_i. \quad (1.42)$$

Note that coordinates 1 and 3 of the second term are identically zero (constant  $(L_1$  and  $L_3)$ ). The equation of motion in rescaled coordinates for each particle, with  $\mathbf{F}_i$  the total force exerted on particle  $i$ , now reads

$$(1 \leq i \leq N) \quad m_i\ddot{\mathbf{s}}_i = \underline{\underline{\mathbf{L}}}^{-1}\cdot\mathbf{F}_i. \quad (1.43)$$

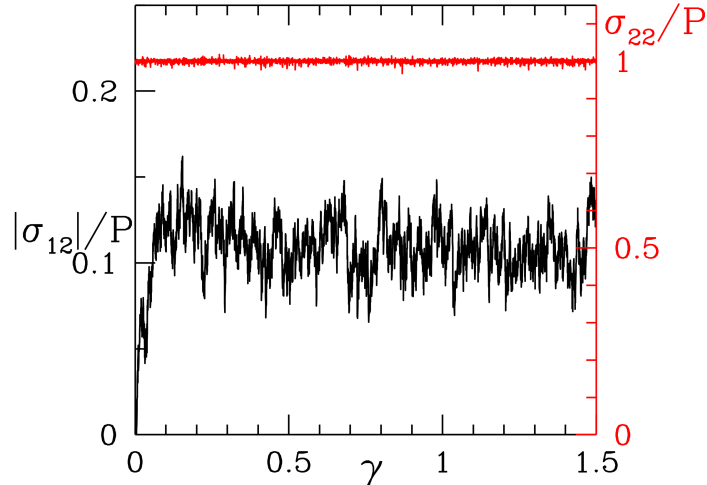


Figure 1.18:  $\sigma_{12}$  (left axis, in black) and  $\sigma_{22}$  (right axis, in red) as functions of shear strain  $\gamma$ . Results of [104], 3D simulations of rigid frictionless grains, under a constant normal stress  $P$ , with  $I = 3 \times 10^{-5}$ .

In the original Parrinello-Rahman method, this equation also includes other terms, involving  $\dot{\underline{\mathbf{L}}}$ , because of the Hamiltonian, conservative form of dynamics one should implement in molecular systems. But these terms have almost no influence on the behaviour of a dissipative system, and they can be neglected in a granular material simulation, in which energy conservation is not an issue [1]. Eq. 1.43 should also be supplemented by the angular momentum balance equation, for the grain rotations.

We also need to calculate the acceleration corresponding to the fluctuations of the system size in  $x_2$  direction. The total normal stress in  $x_2$  direction is given by  $\sigma_{22} - P$ , in which  $P$  is the controlled normal stress and  $\sigma_{22}$  is the internal normal stress given by Eq. 1.15.

$$M\ddot{L}_2 = \frac{\Omega}{L_2}(\sigma_{22} - P) = \frac{1}{L_2} \left[ \sum_{i=1}^N m_i (\dot{s}_i^{(2)})^2 + \sum_{i<j} F_{ij}^{(2)} r_{ij}^{(2)} \right] - \frac{\Omega}{L_2} P. \quad (1.44)$$

$M$  is a generalized mass associated with the degree of freedom  $L_2$ . Its value, a fraction of the total sample mass [1], should be chosen in such a way that condition  $\sigma_{22} = P$  is satisfactorily maintained. Eq. 1.43 and Eq. 1.44 provides all the necessary elements for modeling the dynamics of a sheared sample – the fixed shear rate being imposed through the boundary condition.

### Steady state and measurements

The steady state, in shear flow, is reached when the strain is large enough, so that the flow properties do not change further and are independent of the initial configuration. The critical state, discussed in Sec. 1.1.3, is a special case of steady state, in the quasistatic limit of  $I \rightarrow 0$ . One can approach a steady state for any shear rate, which depends on inertial parameter  $I$ . Fig. 1.18 displays typical evolutions of stress components  $\sigma_{12}$  and  $\sigma_{22}$ , with shear strain  $\gamma$ , in simulated shear flow. The steady state is apparent as corresponding to the plateau value of  $\sigma_{12}$ , after the initial shear stress increase with strain, for  $\gamma \gtrsim 0.1$ . In the steady state the shear stress merely fluctuates about a mean value. These results are measured in shear flow [104] under prescribed pressure  $P$ . The nearly constant value of  $\sigma_{22}/P$  confirms that the normal stress is well-controlled.

The approach to the steady state is usually detected with a small set of basic state variables, among which are shear stress  $\sigma_{12}$  and solid fraction  $\Phi$ . Such quantities should be measured by averaging over the time series, excluding the initial transient, e.g.,

$$\mu^* = \left\langle \frac{|\sigma_{12}|}{\sigma_{22}} \right\rangle_t \quad \text{or} \quad \Phi = \langle \Phi \rangle_t. \quad (1.45)$$

In practice, some of these observables exhibit rather large fluctuations: thus, the typical fluctuations of  $\sigma_{12}$ , in Fig. 1.18, exceed 30% of the mean value. A proper evaluation of the average value requires careful statistical approaches and error estimates. A convenient method to estimate the statistical uncertainty on the measurements of averages over finite time series, is the *blocking* (or *renormalization group*) technique presented in [47]. This procedure amounts to break the whole time series, of duration  $T$ , into  $n$  subsets or “blocks” extending over smaller time intervals  $T_1 = T/n$ , evaluate averages over each one, check that the variance of the values of such average scales as  $1/T_1$  if  $T_1$  is large enough, and then extrapolate to the complete steady state time series ( $n = 1$ ). This yields error bars on measurements of averages in finite systems which should not be confused with the quadratic average of fluctuations of the observable quantity. The method identifies the minimum size of independent blocks. It does not involve any approximation and gives the correct answer when it exists provided the analyzed series is sufficiently long. In practice, due to intrinsic long-lasting correlations in granular systems, quite long runs are necessary [104].

## 1.4 Dense flow: the “ $\mu^*(I)$ rheology”

### 1.4.1 From numerical results to constitutive modeling

Simulations of model granular materials in steady uniform shear flows [31] under prescribed normal stress  $P$  contributed to identify a classification of flow regimes, under controlled normal stress, in terms of inertial parameter  $I$  (as recalled in Sec. 1.3.2, in relation with the definition of  $I$ ), which proved particularly convenient. For a given material (and a certain value of  $\mu$ , the intergranular friction coefficient), its state in steady uniform shear flow, according to Tab 1.1, only depends on  $I$ , provided  $\kappa$  remains large. Thus, measurements of shear stress  $\sigma_{12}$ , or, equivalently, since  $\sigma_{22}$  is kept constant, of effective friction coefficient  $\mu^* = \sigma_{12}/\sigma_{22}$ , on the one hand; and of solid friction  $\Phi$ , on the other hand, as functions of  $I$ , provide essential constitutive laws, referred to as the friction law and the density law<sup>4</sup>:

$$\begin{cases} \mu^* &= \mu^*(I, \mu) \\ \Phi &= \Phi(I, \mu) \end{cases} \quad (1.46)$$

Fig. 1.19 expresses those laws in a model 2D system, with  $\mu = 0.4$ , suggesting a linear form for  $I$  dependences of  $\mu^*$  and  $\Phi$ :

$$\begin{cases} \Phi(I) &= \Phi_{\max} - \alpha I \\ \mu^*(I) &= \mu_{\min}^* + \beta I \end{cases} \quad (1.47)$$

for some interval of  $I$  (say  $0.04 \leq I \leq 0.2$ ), with  $\mu_{\min}^* = 0.25$ ,  $\beta = 0.3$  and  $\Phi_{\max} = 0.81$ ,  $\alpha = 1.1$ . The results, as announced, do not notably depend on  $e$ .  $\mu_{\min}^*$  and  $\Phi_{\max}$  coincide with the internal friction and the solid fraction of the material in the quasistatic critical state.

The change in the material state  $I$  increases from the quasistatic limit to 0.3 is illustrated by Fig. 1.20, in which a gradual depletion of the force-chain network of quasi-static states is

---

<sup>4</sup>sometimes called dilatancy law – but this might be confusing, as Reynolds dilatancy does not correspond to an increase of volume upon increasing the shear rate, but, rather, to an effect of shear strain in static granular assemblies.

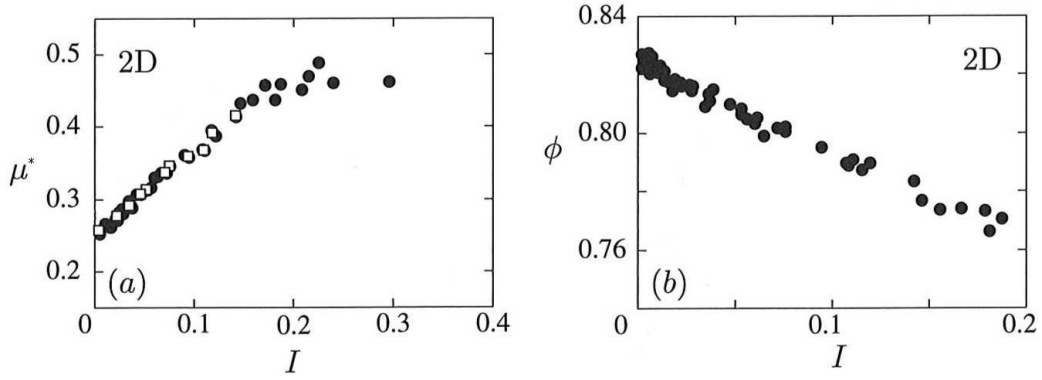


Figure 1.19: Variation of  $\mu^*$  (a), and  $\Phi$  with  $I$ , in a 2D simulation [31] of disks, with  $\mu = 0.4$  and two different values of restitution coefficient:  $e = 0.1$  (filled circles) and  $e = 0.9$  (open squares).

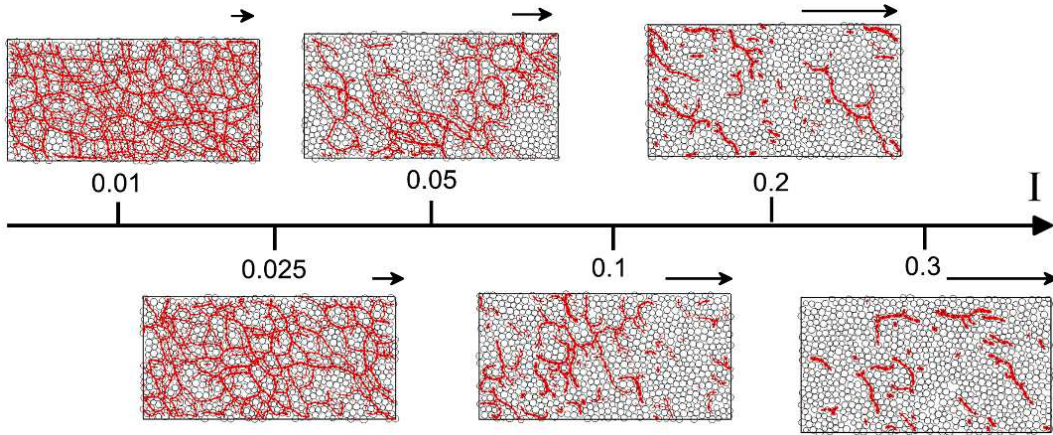


Figure 1.20: Influence of inertial number  $I$  on contact network. (Obtained by DEM simulation in [121]).

witnessed, while increasingly isolated, strong binary interactions resemble at larger  $I$  values collisional momentum transport characterizing granular gases. The linear variations with  $I$  of  $\Phi$  and  $\mu^*$  were reported to cross over to different power laws in the quasistatic limit, for small  $I$  [62, 104]. The simple classification of states, and parametrization of laws, with the sole number  $I$  assumes  $\kappa$  to be large enough ( $\kappa > 5000$  is, most often, sufficiently rigid). When grains deform with larger contact deflections in the flow, various flow regimes are charted, depending on two parameters [22, 23]. The variable most sensitive to a decrease in stiffness parameter  $\kappa$  [31] is the coordination number. Fig. 1.21 reveals a weak dependence of  $z$  on  $\kappa$  while it varies significantly with  $I$ .  $z$  decreases for larger values of  $I$ , where a similar behaviour of solid fraction  $\Phi$  is also reported [104]. Note that the isostatic value  $z^* = 6$  is retrieved in quasistatic limit (see footnote p. 12).

Constitutive laws of type (1.46) or (1.47) proved apt, once implemented locally in various flow geometries, to quantitatively predict velocity fields [49]. The results reported in [73] are particularly striking in that respect. Having first measured  $\mu^*(I)$  in inclined planes experiments (a simple case in which  $\mu^*$ , and hence  $I$ , is constant in the flowing layer, save for boundary effects), Jop *et al.* applied it (in suitably generalized tensorial form) to model the rather complex velocity field in the flow of a granular layer between rough parallel lateral walls on top of an erodible bed (with gradients in several directions). The resulting predictions,

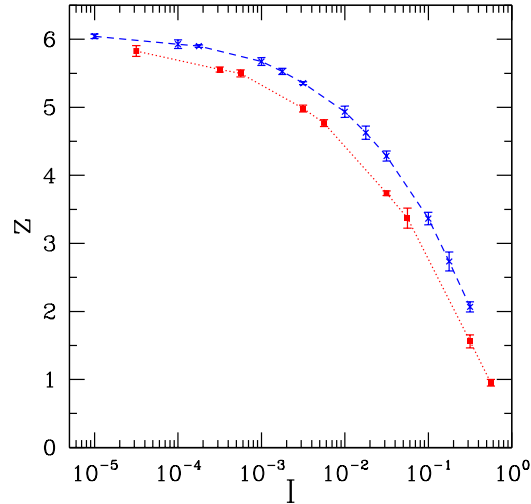


Figure 1.21: Coordination number  $z$  as a function of inertial number  $I$ , for stiffness number  $\kappa = 39000$  (red square dots, dotted line) and  $\kappa = 8400$  (blue crosses, dashed line) in simulations of frictionless beads [104].

involving no adjustable parameter, proved remarkably accurate.

#### 1.4.2 Pressure controlled versus volume controlled behaviour

In a pressure-controlled shear flow, the system size  $L_2$  is allowed to fluctuate in order to maintain the normal stress constant,  $\sigma_{22} = P$ . In a more traditional approach, the volume is kept constant rather than the normal stress [22].

The first advantage of pressure-controlled configurations is that this method permits to approach quasistatic values of solid fraction and internal friction when  $I \rightarrow 0$ . Such a flow is not possible in volume-controlled tests, unless for  $\Phi = \Phi_c$ . For solid fractions below the critical value, the volume increase is due to inertial effect and the flow is not quasistatic. For solid fractions larger than  $\Phi_c$ , the material cannot flow without imposing large enough contact deflections to particles, which may damage the grains or the apparatus. When  $\Phi$  approaches  $\Phi_c$  in steady shear flow, with fixed values of  $\Phi$  and  $\dot{\gamma}$ , considering that  $I$  approaches zero for  $\Phi \rightarrow \Phi_c$ , it leads to a divergence of  $P$  and  $\tau$  ( $\sim \mu^* P$ ). So when  $\Phi$  is used as a control parameter, the value  $\Phi = \Phi_c$  appears to be a singular point [81]. Ideally rigid grains ( $\kappa \rightarrow +\infty$ ), at  $\Phi = \Phi_c$ , would jam sooner or later [81]. With stiff, but not perfectly rigid grains, the singularity is slightly smoothed out, but one expects normal and shear stresses to have large fluctuations close to  $\Phi_c$ . This is indeed apparent in Fig. 1.22a. However, the amplitude of the fluctuation of ratio  $\tau/P$  remain finite, similar to those obtained in constant pressure tests [106](Fig. 1.22a). Fig. 1.22 compares the fluctuations of stress components and solid fraction in volume-controlled and pressure-controlled configurations. The fluctuations of ratio  $\tau/P$  in both cases are similar, although the fluctuations of  $\Phi$  in the constant pressure test are much smaller than the fluctuations of  $P$  in the constant volume test. Those fluctuations regress in the large system limit [104]. Although both procedures are equally valid and determine the same internal friction coefficient, the pressure-controlled test avoids the singular fluctuations of stress, and should be more convenient.



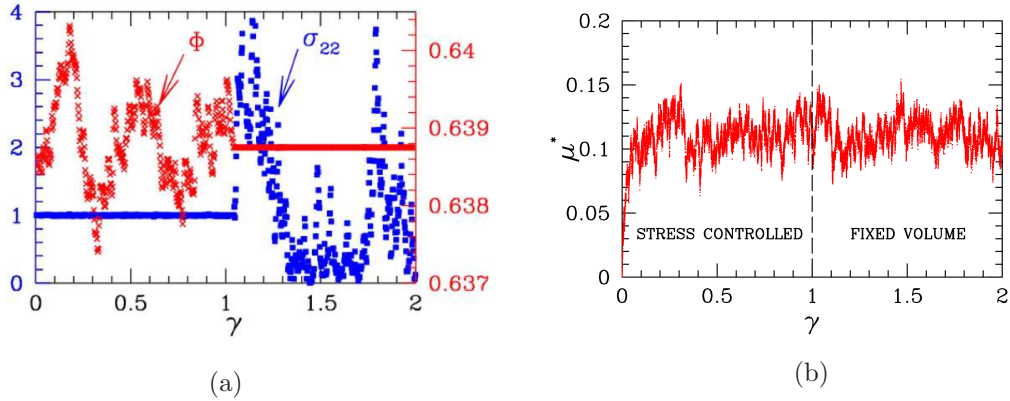


Figure 1.22: Fluctuations of solid fraction and stress components in a pressure-controlled simulation versus volume-controlled simulation. (a) For  $\gamma < 1$ ,  $P = \sigma_{22}$  is controlled while  $\Phi$  fluctuates. For  $\gamma > 1$ ,  $\Phi$  is controlled and  $P$  fluctuates. (b) Fluctuations of  $\tau/P$  for constant pressure (left) and constant volume (right). The figures are extracted from [107, 105].

### 1.4.3 Dense flow of cohesive grains

Cohesive forces are known to strongly influence the flow properties of granular materials. Macroscopic friction coefficient  $\mu^*$  strongly increases in the presence of attractive interactions [118, 143]. This is usually described by the Coulomb criterion [111, 118], Eq. 1.1, in which  $c$  represents the macroscopic intensity of cohesion. The experimental studies on the flow of powder in a rotating drum show that dense flows cannot be achieved using too small grains such as fine powders [27, 28]. However, dense cohesive flows can be experimentally observed with large enough grains such as wet glass beads [145], or with natural snow [121]. Fig. 1.23 represents internal friction  $\mu^*$  and solid fraction  $\Phi$  as functions of inertial number  $I$ , for dense flow of 2D cohesive grains. The results were obtained by Rognon *et al.* [122], in simulations of steady plane shear flow. Instead of the reduced pressure  $P^*$ , a *cohesion number*  $\eta$ , defined as  $\eta = 1/P^*$  was used in that study. The curves show the usual behaviour of granular materials, such that  $\mu^*$  increases and  $\Phi$  decreases at growing  $I$ . Moreover, the results show that for smaller values of  $P^*$ , the solid fraction decreases and the internal friction increases, an important effect for  $P^*$  below 0.1.

Rognon *et al.* also observed that, despite the decrease of solid fraction, the coordination number  $z$  increases for smaller values of  $P^*$ . The absence of a general relation between density and coordination number in cohesive grain assemblies has also been reported in isotropic cohesive disk packings [54, 55]<sup>5</sup>. Variations of  $\Phi$  and of  $z$  in opposite directions reveal the agglomeration of cohesive grains. As adhesive particles stick to one another, the coordination number increases, while the formation of loose aggregates increases the porosity of the granular structure. The aggregation of cohesive grains is observed in many other numerical studies and experiments [120, 144, 90, 20, 150].

## 1.5 Dense suspensions

Dense suspensions [142, 57] of solid particles are present in many natural and industrial processes, with examples in civil engineering (fresh cement or bituminous road pavement

<sup>5</sup>There is no general relation between  $\Phi$  and  $z$  with cohesionless grains either [1] although their variations are often correlated.

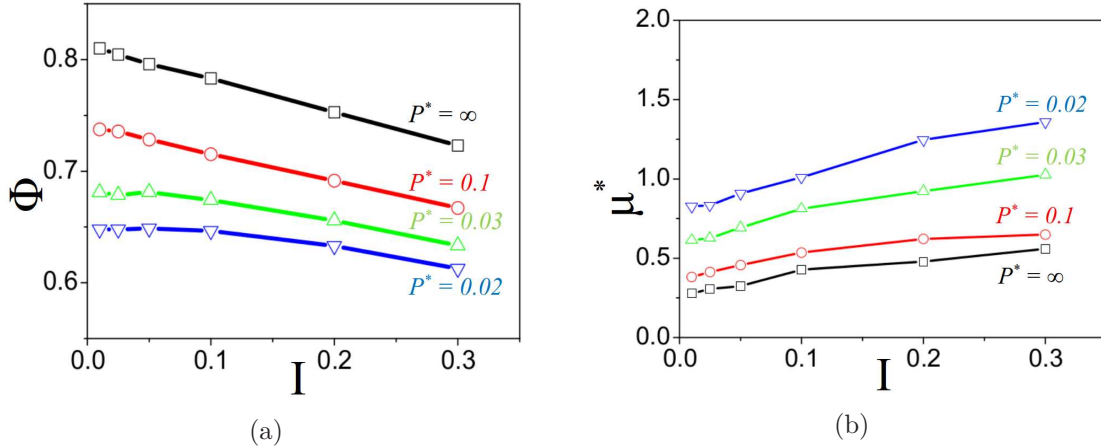


Figure 1.23: Macroscopic friction coefficient  $\mu^*$  and solid fraction  $\Phi$  versus  $I$  for different values of  $P^*$ . The results are obtained by 2D simulations of the shear flow of cohesive grains [122]. Note that  $\eta$  in the original paper is replaced by  $P^*$ .  $P^* = \infty$  indicates the results for the simulation of dry grains.

materials), biology (blood), food processing...

Here we limit our discussion to suspensions of rigid, non-Brownian particles, with no distant interaction other than hydrodynamic, in a Newtonian viscous incompressible liquid, with shear viscosity  $\eta_0$ . Most reported experimental works studied model systems in which spherical, nearly monodisperse grains were mixed in a liquid of equal density [14]. We refer to this class of suspension as granular suspensions, or granular pastes.

### 1.5.1 Scope, basic properties

#### Granular suspensions

As compared to dry granular materials, granular suspensions share similar static aspects: in particular, the grains, should they come into solid contact, should interact by elastic and frictional forces, as described in Sec. 1.2.1. The dynamics are however dominated by viscosity, rather than inertia. We focus on the *limit of vanishing Reynolds number*. Defined in terms of particle diameter  $a$ , liquid viscosity  $\eta_0$ , liquid mass density  $\rho$  and shear rate  $\dot{\gamma}$  as

$$\mathcal{Re} = \frac{\dot{\gamma} a^2 \rho}{\eta_0} \quad (1.48)$$

the Reynolds number [80] compares viscous and inertial terms in the Navier-Stokes equations. In the limit of  $\mathcal{Re} \rightarrow 0$ , inertia plays no part, and the velocity field in the liquid is described by the Stokes equation:

$$\begin{aligned} -\vec{\nabla} p_f + \eta_0 \Delta \mathbf{v} &= 0 \\ \vec{\nabla} \cdot \mathbf{v} &= 0, \end{aligned} \quad (1.49)$$

involving some pressure field  $p_f$  in the liquid domain. Velocity field  $\mathbf{v}$  should satisfy the condition of continuity on all solid grain surfaces – on each point  $\mathbf{r}$  of the boundary of grain  $i$ , whose center of mass, at point  $\mathbf{R}_i$  has velocity  $\mathbf{V}_i$ , and of angular velocity  $\Omega_i$ , it should coincide with the rigid body form

$$\mathbf{v}(\mathbf{r}) = \mathbf{V}_i + \Omega_i \wedge (\mathbf{r} - \mathbf{R}_i). \quad (1.50)$$



It is legitimate to neglect Brownian motion for very large *Péclet number*, usually defined (with  $R = a/2$  the particle diameter) as

$$\mathcal{P}e = \frac{6\pi\eta_0 R^3 \dot{\gamma}}{k_B T}, \quad (1.51)$$

in which  $k_B$  is Boltzmann's constant and  $T$  denotes the absolute temperature. The diffusion coefficient for a Brownian sphere of radius  $R$  in a liquid of viscosity  $\eta_0$  being  $D = \frac{k_B T}{6\pi\eta_0 R}$  [60],  $\mathcal{P}e$ , as defined in (1.51), is the ratio of the characteristic diffusion time of one particle on distance  $R$ ,  $\tau_D = R^2/D$ , to the shearing time,  $1/\dot{\gamma}$ .  $\mathcal{P}e$  is very large for particles with  $R > 10 \mu\text{m}$  and liquids with  $\eta_0 \geq 10^{-2} \text{ Pa}\cdot\text{s}$ , with shear rate in the  $10^{-1} \text{ s}^{-1}$  or above. As to colloidal forces (see Sec. 1.2.3) they are usually negligible for such particles.

### Diphasic aspects and the homogeneity issue

Apart from viscous hydrodynamic effects, suspensions differ from granular materials in their *diphasic* character. In general, one should describe, in macroscopic constitutive laws, both the motion of the suspending liquid and that of the grains, with such phenomena as sedimentation, filtration flow, or particle migration [57]. Sedimentation might be avoided on using neutrally buoyant particles [14]. In a steady flow, one should have a constant concentration field – but not necessarily uniform, which motivated recent rheometric experiments [102, 16] to track a local constitutive law relating the effective suspension viscosity to the strain rate and the density at some point in the flow where all these data are simultaneously available. Various experimental techniques might be used, such as Particle Image Velocimetry [16] or Magnetic Resonance Imaging [102]. For lack of such local information, many measurements of the effective viscosity of a suspension should be regarded with suspicion.

### Macroscopic constitutive laws

The behaviour one is generally interested in is expressed by the effective viscosity  $\eta$  of the suspension, measured (locally !) as the ratio of the shear stress to the shear rate. Let us consider a Couette (simple shear) flow, and assume, for simplicity, the material to be homogeneous, and the shear rate  $\dot{\gamma}$  uniform. Defining, conventionally, direction 1 as that of the flow, direction 2 as that of the velocity gradient (thus  $\dot{\gamma} = \frac{\partial v_1}{\partial x_2}$ ), so that the vorticity is in direction 3, one measures:

$$\eta = \frac{\sigma_{12}}{\dot{\gamma}}. \quad (1.52)$$

as a function of solid fraction  $\Phi$  and of  $\dot{\gamma}$ . The suspension is said to be *shear thinning* if  $\eta$  is a decreasing function of  $\dot{\gamma}$ , and *shear thickening* if it grows with  $\dot{\gamma}$ . Newtonian liquids, of course, have shear-rate independent viscosities. Brownian suspensions are usually shear thinning. Some shear-thickening might be observed in non-Brownian suspensions at high enough shear rate, due to inertial effects [81, 45]. But suspensions of hard particles with no Brownian motion should exhibit no dependence of  $\eta$  on  $\dot{\gamma}$ , provided  $\mathcal{R}e$  remains very small. This may be understood from simple dimensional analysis [142]. The viscosity ratio  $\eta/\eta_0$  should only depend on dimensionless parameters:

$$\frac{\eta}{\eta_0} = f(\Phi, \mathcal{R}e, \mathcal{P}e) \quad (1.53)$$

and all dependence on  $\dot{\gamma}$  should disappear in the double limit of  $\mathcal{R}e \rightarrow 0$  and  $\mathcal{P}e \rightarrow \infty$ . One may also invoke an invariance argument [81]: hard particle interactions introduce no characteristic time, and changing  $\dot{\gamma}$  amounts to going along the same trajectories in configuration space, with a rescaled time.

### Normal stresses and particle stresses

One also records the first and the second *normal stress differences*, defined as<sup>6</sup>

$$\begin{aligned} N_1 &= \sigma_{11} - \sigma_{22} \\ N_2 &= \sigma_{22} - \sigma_{33} \end{aligned} \tag{1.54}$$

Those quantities are difficult to measure, and their values are still discussed in the literature [14]. Unlike Newtonian fluids, suspensions of hard non-Brownian objects have non-vanishing normal stress differences, which relate to the formation of an anisotropic structure in shear flow [14, 15]. This anisotropy gradually changes sign upon changing the sign of  $\dot{\gamma}$ . Upon such a reversal, the apparent viscosity goes through a minimum  $\eta_{\text{iso}}$  that is believed to correspond to an isotropic structure.

In general the absolute values of normal stresses  $\sigma_{ii}$  have no intrinsic meaning, because the pressure  $p_f$  of the incompressible liquid is determined by the flow conditions, rather than its constitutive relations. One sometimes accesses to the so-called particle normal stresses, defined as (for the considered simple shear flow, in which all components of the strain rate vanish except 12 and 21)

$$\sigma_{ij}^p = \sigma_{ij} + p_f \delta_{ij} - \eta_0 \dot{\gamma} (\delta_{i1} \delta_{j2} + \delta_{i2} \delta_{j1}). \tag{1.55}$$

if the liquid pressure is measurable.

### Viscosity divergence in the jamming limit

The effective viscosity grows with solid fraction  $\Phi$  and is observed to diverge at some maximum value  $\Phi^*$  above which no flow is possible, due to solid particle jamming. This divergence is usually fitted as a power law [75],

$$\frac{\eta}{\eta_0} \sim \left(1 - \frac{\Phi}{\Phi^*}\right)^{-\alpha}. \tag{1.56}$$

Values near 2 are often reported for exponent  $\alpha$  [142, 17, 16]. As to the viscosity of the isotropic suspension, it is reported to diverge with a smaller exponent,  $\alpha \simeq 1$  [14].

Although apparently simple, suspensions of non-Brownian, non-colloidal hard spheres thus possess a number of rheological properties that are not entirely understood. One difficulty is the assessment of the nature and the role of interparticle contacts. Different contact or near-contact properties should explain the different values of solid fraction  $\Phi^*$  reported in the literature: about 0.605 in [102], 0.54 in [16]... But, in general, little is known about the small-scale interactions, governing possible combinations between solid contacts and hydrodynamic interactions. One particular difficulty, which Sec. 1.5.2 will deal with in more detail, is the *lubrication* phenomenon, by which the hydrodynamic force between two particles separated by a narrow interstice of thickness  $h \ll a$ , for given relative normal velocity, diverges as  $1/h$ . Such a hydrodynamic coefficient  $A/h$ , with  $A$  a constant, implies, for a given force  $F$  pushing two particles towards each other, the differential equation

$$\frac{dh}{dt} = -\frac{F}{A}h, \tag{1.57}$$

whence for finite force an exponential decay of  $h$ , but no contact ( $h = 0$ ) in a finite time. This effect results from the local, asymptotic form in which the Stokes equations may be approximated to in narrow channels between quasi-parallel solid surfaces [58, 61]. At close

---

<sup>6</sup>The sign convention here is that of fluid mechanics, i.e., tensile stresses are positive.

approach, surfaces are no longer smooth and quasi-parallel, so the  $1/h$  singularity is cut off when  $h$  is of the order of a length  $l_R$  – a characteristic size of surface asperities – and thus solid contacts may occur within finite times. In most practical cases,  $l_R/a$  is of order  $10^{-4}$  to  $10^{-2}$ . Numerical simulations, in which all microscopic ingredients of the model are fully controlled, should provide useful information on the effect of  $l_R$  and other modeling choices (implementation of solid contact models) on macroscopic material properties.

## 1.5.2 Micromechanical modeling and simulations

### Hydrodynamic interactions and hydrodynamic resistance matrix

The most remarkable property of Stokes equations (1.49) is their linearity. A linear operator  $\underline{\underline{\Xi}}$  thus relates viscous drags  $\mathbf{F}^H$  to velocities  $\mathbf{V}$ , as

$$\mathbf{F}^H = -\underline{\underline{\Xi}} \cdot \mathbf{V}, \quad (1.58)$$

which defines the *hydrodynamic resistance matrix*  $\underline{\underline{\Xi}}$  [61]. On writing (1.58), it is most convenient to include all velocities and angular velocities of particles in  $\mathbf{V}$ , along with some other kinematic parameters, such as, e.g., strain rate  $\dot{\epsilon} = -\dot{L}_2/L_2$ , if we are interested in a deformable box as in the simulations of normal stress controlled shear flows.

The basic assumption of Stokes flow ( $\mathcal{R}e = 0$ ) requires external forces  $\mathbf{F}^{\text{ext}}$  to be balanced by hydrodynamic ones:

$$\mathbf{F}^{\text{ext}} + \mathbf{F}^H = 0, \quad (1.59)$$

whence a determination of velocities:

$$\mathbf{V} = \underline{\underline{\Xi}}^{-1} \cdot \mathbf{F}^{\text{ext}}, \quad (1.60)$$

(1.60) is the equation of motion for viscous suspensions. External forces in (1.60) might be identified by their power, and thus the force conjugate to strain rate  $\dot{\epsilon}$  is just  $\Omega \Sigma_{22}$ , the product of the system volume by the applied normal stress in direction 2. Eq. 1.60 is complicated because of the dependence of the hydrodynamic resistance matrix on particle positions. The Stokesian Dynamics simulation method [18] uses multipole developments of velocity fields to evaluate  $\underline{\underline{\Xi}}$ , or its inverse, the mobility matrix  $\underline{\underline{\Xi}}^{-1}$ , in suspensions of spherical particles. The intrinsically long ranged nature of hydrodynamic interactions, and their complex, many-body structure (those forces are not pairwise additive) entail considerable difficulties in the simulation of suspensions, a field in which the progress in numerical performance appears much slower than in DEM simulations of granular assemblies. As an example, the more calculations of [135], which benefited from an efficient numerical implementation of the ‘‘Stokesian dynamics’’ method [136], are limited to 512 particles in the range  $0.5 \leq \Phi \leq 0.6$  and higher concentrations were not explored.

### The assumption of lubrication force dominance

Given that large hydrodynamic couplings between close neighbours should provide the dominant forces, Melrose and Ball [92] – see also [11, 93] – proposed to keep only the asymptotic form of such near-neighbour hydrodynamic interactions ( $h \ll a$ ), thereby considerably simplifying the model. As we are going to implement our version of this approach in Chapter 3, we introduce it in more detail here. In this approach one ignores the long ranged part of hydrodynamic interactions and resorts to the ‘‘pair drag frame invariant’’ model of [11] and [137], in which hydrodynamic forces are pairwise additive and only couple pairs of particles separated by a distance  $h$  lower than some threshold  $h_c$ .  $h_c$  is arbitrarily chosen, but the sensitivity of the results to its value can be assessed. The hydrodynamic force exerted by

particle  $i$  onto its neighbour  $j$  linearly depends on the *relative* velocity  $\delta\mathbf{V}_{ij}$ , defined as the difference between the velocities of the mid-gap point, on the line joining centers, regarded as moving with solids  $i$  or with solid  $j$ . Those relative velocities are in turn determined by velocities  $(\mathbf{V}_i)_{1 \leq i \leq N}$  of the bead centers, and rotation velocities  $(\omega_i)_{1 \leq i \leq N}$  of the beads. Denoting as  $\mathbf{R}_{ij}$  ( $\mathbf{R}_{ji}$ ) the vector joining the center of  $i$  (respectively, of  $j$ ) to the mid-gap point (i.e., the middle point between centers if  $i$  and  $j$  have equal diameters), one has:

$$\delta\mathbf{V}_{ij} = \mathbf{V}_i + \omega_i \wedge \mathbf{R}_{ij} - \mathbf{V}_j - \omega_j \wedge \mathbf{R}_{ji}. \quad (1.61)$$

Forces are approximated by the dominant, lubrication terms in the limit of small interstices  $h_{ij}$  between the surfaces of neighbouring particles  $i$  and  $j$  [11]. If  $\mathbf{n}_{ij}$  denotes the normal unit vector pointing from  $i$  toward  $j$ , then

$$\mathbf{F}_{ij} = [\xi_N(h_{ij}) \mathbf{n}_{ij} \otimes \mathbf{n}_{ij} + \xi_T(h_{ij}) (\mathbf{1} - \mathbf{n}_{ij} \otimes \mathbf{n}_{ij})] \cdot \delta\mathbf{V}_{ij} \quad (1.62)$$

Expression (1.62) actually contains the leading order and some next to leading order terms in the limit of  $h_{ij} \rightarrow 0$ , as coefficients  $\xi_N$  and  $\xi_T$  (which both vanish for  $h > h_c$ ) diverge in the limit of  $h \rightarrow 0$  [11]:

$$\begin{aligned} \xi_N(h) &= \frac{3\pi\eta_0 a^2}{8h} \\ \xi_T(h) &= \frac{\pi\eta_0 a^3}{8} \ln\left(\frac{a}{2h}\right). \end{aligned} \quad (1.63)$$

Let us note at this stage, for future use, that combining Eqs 1.57 and 1.63, one gets a characteristic squeezing time for interparticle gaps under normal force  $F$  as (ignoring numerical factor  $3\pi/8$ )

$$\tau_S(F) = \frac{\eta_0 a^2}{F} \quad (1.64)$$

Total hydrodynamic forces and moments on particle  $i$  are then given by

$$\begin{aligned} \mathbf{F}_i^H &= \sum_j \mathbf{F}_{ji} \\ \mathbf{\Gamma}_i^H &= \sum_j \mathbf{R}_{ij} \wedge \mathbf{F}_{ji} \end{aligned} \quad (1.65)$$

Relations (1.63) stem from calculations with the lubrication approximation within the interparticle gap, as recalled by [11]. (1.63) is admittedly a simplified form of the complete pair drag interaction specified in this reference, as some terms comparable to  $\xi_T(h)$  have been discarded. In the study of Chapter 3, we shall mostly resort to a model with only normal forces, i.e. take  $\xi_T(h) = 0$ , as the  $1/h$  divergence will dominate the hydrodynamic resistance matrix anyway. This choice, as in other numerical studies [93], may greatly simplify the model, especially if all other interaction forces are also purely normal. Since the rotation of spheres with central force interactions can be ignored, the number of degrees of freedom  $N_f$  decreases from  $N_f = 6N$  to  $N_f = 3N$ .

### Lubrication singularity and contact problem

The form of  $\xi_N(h)$  is a source of serious numerical problems at high particle concentration [11]. Confronted with those numerical difficulties, different groups chose to introduce various forms of repulsive forces, keeping interparticle gaps within tractable range. One possibility is to allow true intergranular contacts to occur, by cutting off the divergence of resistance matrix element  $\xi_N(h)$  close to contact [140]. One may, thus, use the function depicted in Fig. 1.24. For  $h \leq h_{\min}$ , the graph of function  $\xi_N(h)$  is replaced by its tangent in  $h_{\min}$ . For  $h \geq h_{\max}$

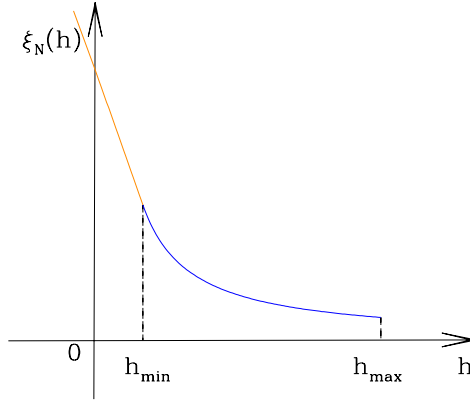


Figure 1.24: Resistance matrix element  $\xi(h)$  coupling normal approach velocity to normal force in particle pair, separated by distance  $h$ .

the hydrodynamic coupling coefficient is set to zero – the asymptotic expression (1.63) is no longer valid, and the remaining  $\xi(h)$  is deemed negligible. The weaker logarithmic divergence of  $\xi_T$  can be dealt with in the same manner. Once particles have come into contact, one may simply add the contact forces, as modeled in Se. 1.2.1 to the hydrodynamic ones. This is justified if the change in the geometry of the contact region is small enough and does not significantly perturb the velocity in the liquid region contributing to the hydrodynamic force.

### Viscous jamming and hydroclusters

Non-hydrodynamic forces, however small, are reported to become important at high volume fractions  $\Phi$  [19]. Particle interactions at short distance, which many numerical simulation studies have introduced in the model [39, 138, 135, 93], are difficult to control in laboratory experiments, a likely explanation for the variety of results reported as to the divergence of  $\eta$  as  $\Phi$  approaches some maximum  $\Phi_m$  [142]. Reported values of  $\Phi_m$  may differ from the random close packing solid fraction,  $\Phi_{RCP}$ .

Several authors contend that the basic model, without lubrication cutoff, is pathological in the sense that no steady state could be achieved in simple shear [92, 10]. Such behaviour is attributed to the formation of large clusters of particles separated by very narrow interstices. Those “hydrodynamic clusters” should be very difficult to deform and reportedly cause the cessation of flow as they percolate. A jamming transition would thus occur below  $\Phi_{RCP}$ , as predicted in a theoretical approach based on a kinetic model for rod-shaped clusters [46]. Hence the statements, repeatedly made in the recent literature [91, 39, 135], that interparticle forces are indispensable to observe continuous shear flow, and that shear-thickening is due to the decreasing capacity of other forces, as hydrodynamic ones increase with  $\dot{\gamma}$ , to limit the size of the hydrodynamic clusters and overcome the jamming tendency of purely hydrodynamic interactions.

### 1.5.3 The “granular” approach to suspension rheology

The recent progress in the modeling of dry granular flows, with the development of the approach of Sec. 1.4, inspired a new point of view [25, 17] on the rheology of dense assemblies of particles interacting at their contacts. One may, instead of measuring a viscosity in shear flow at constant solid fraction, characterize the material rheology by the shear resistance of the particle arrangement under a given normal (particle) stress, i.e. an internal friction coefficient. The normal-stress controlled Couette apparatus of Fig. 1.25 was designed to carry out such experiments, in which the granular phase may dilate or contract, depending on the

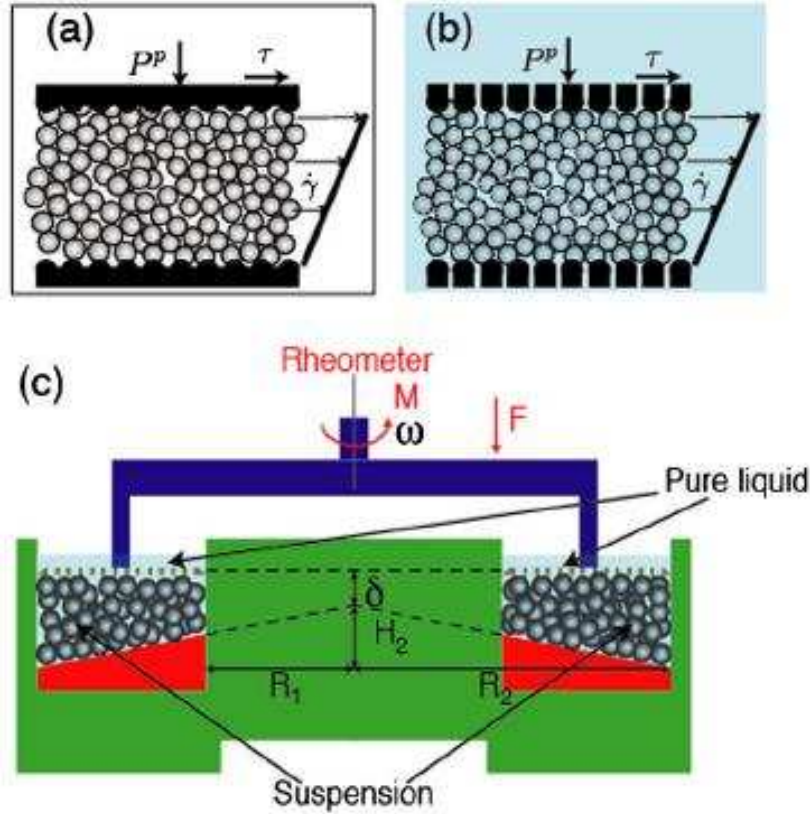


Figure 1.25: Rheometric device (c) used in [17] to study (a) pressure imposed shear flow of granular materials, or (b) particle pressure imposed shear flow of suspensions, for which the vertically mobile lid applying the confining pressure is permeable to the interstitial liquid.

density necessary to support  $P_p$  under the imposed strain rate  $\dot{\gamma}$ ... Thus the analogy to dry granular materials in pressure-controlled shear flow is complete if we define an analog of inertial number  $I$ . Introducing the *viscous number*  $\mathcal{V}i$ , based on the squeezing time defined with the typical grain-level force  $P_p a^2$ :

$$\mathcal{V}i = \dot{\gamma} \tau_S (P_p a^2) = \frac{\eta \dot{\gamma}}{P_p} \quad (1.66)$$

one may use it as the inertial number of dry grains. Characterizing the suspension with a friction law and a density law, as functions of parameter  $\mathcal{V}i$  offers the same advantages as the  $\mu^*(I)$  rheology for dry grains. In particular, the quasi-static limit is approached for small  $\mathcal{V}i$ . Then the applied particle pressure has plenty of time to squeeze the fluid in narrow gaps, and the behaviour should be dominated by intergranular contacts. The material should have a quasistatic plastic flow, with contact forces supporting the load... in other words, one recovers the critical state in that limit.

The coincidence of the same critical state in the quasistatic limit for dry, frictional grains and dense granular paste, in which a lubrication cutoff enables grains to touch one another, was observed in a simple numerical model in 2D, of the Ball-Melrose (lubrication dominance) type [107]. This is shown in Fig. 1.26, for the internal friction coefficient. In the experimental study reported in [17], using the pressure-controlled Couette cell of Fig. 1.25, the quasi-static value of the solid fraction and of the internal friction coefficient coincided with the critical state value for dry grains.

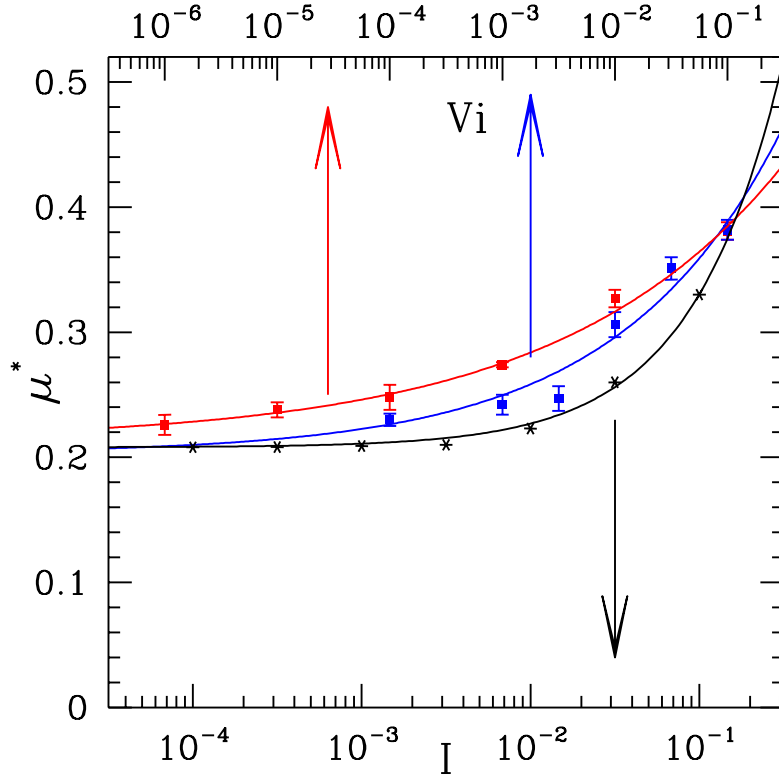


Figure 1.26: Macroscopic friction coefficient  $\mu^*$  for dry granular material (polydisperse disks in 2D, with intergranular friction coefficient 0.3), versus  $I$  (black curve, bottom axis); and for a model suspension of the same grains, versus  $\mathcal{V}i$  (upper axis), with  $h_{\min} = 10^{-2}a$  (red curve) and with  $h_{\min} = 10^{-4}a$  (blue curve).

These results are amenable to the more classical form of a relative viscosity and normal particle stresses as functions of  $\Phi$ . Thus one may write

$$\frac{\eta(\Phi)}{\eta_0} = \frac{\sigma_{12}}{\eta_0 \dot{\gamma}} = \frac{\mu^*(\mathcal{V}i)P_p}{\eta_0 \dot{\gamma}} = \frac{\mu^*}{\mathcal{V}i}, \quad (1.67)$$

which shows the effective viscosity to diverge at the critical solid fraction  $\Phi_c$ , when  $\mathcal{V}i \rightarrow 0$ . Good measurements of high viscosities close to  $\Phi_c$  showing  $\alpha \simeq 1.9$  in (1.56) are reported in [17].





## Chapter 2

# Shear flow of wet granular materials: capillary effects

In this chapter we study the rheological behaviours of non-saturated model granular materials in the pendular regime. We use a 3D discrete element method to simulate the plane shear flow of wet granular material under a controlled normal stress (see Sec. 1.3.3). We focus on steady state rheology under constant shear rate. The particles are spherical, mono-sized, frictional and nearly rigid and they interact by contact forces as well as capillary attraction through menisci. Our simulations are carried out in the range identified in Sec. 1.2.4 as corresponding to the pendular state in realistic materials. We rather characterize the level of liquid in the material with saturation  $S_w$ , which is proportional to liquid content as,  $S_w = W/(1 - \Phi)$ . The pendular state, for a typical value of the solid fraction,  $\Phi = 0.5$ , corresponds to the interval  $1.5 \times 10^{-3} \lesssim S_w \lesssim 0.06$ .

In Section 2.1 we first briefly discuss the model and the choice of parameters, relying on Chap. 1. The macroscopic properties of the material are studied in Sec.2.2. After a discussion of the conditions in which steady homogeneous flows can be observed, the corresponding constitutive laws are identified, the main global effects of different interaction types are investigated and the influence of model parameters tested. Both the intensity of the capillary forces, even in conditions of rather large  $P^*$  in which they do not dominate stresses in the system, and their small, yet finite range, are observed to significantly affect wet granular rheology. In the second part of this chapter, Sec. 2.3, we investigate the corresponding internal material states in steady shear flow and relate the important rheological effects of capillary forces to the relevant internal variables introduced in Sec. 1.2.2. Sec. 2.4 presents a synthesis of the essential results.

### 2.1 Model material and simulation technique

We simulate normal stress-controlled plane shear flows with periodic boundary conditions and the Lees-Edwards technique, as described in Sec. 1.3.3 (Fig. 1.16). The imposed flow parameters are shear rate  $\dot{\gamma}$  and normal stress  $\sigma_{22}$ , simply denoted as  $P$  in the sequel (not to be confused with the average pressure  $\mathcal{P}$ ). The system size in direction  $x_2$  can fluctuate in order to control normal stress  $\sigma_{22} = P$ .

The particles,  $N$  spherical mono-sized grains with diameter  $a$ , have Hertz-Mindlin contact elasticity and friction, as described in Sec. 1.2.1, with deflection modulus  $\tilde{E}$  and friction coefficient  $\mu$ .

In the presence of liquid bridges, the capillary forces are calculated within the Maugis

approximation (see Sec. 1.2.3):

$$F^{\text{Cap}} = \begin{cases} -F_0 & h \leq 0 \\ -F_0 \left[ 1 - \frac{1}{\sqrt{1 + \frac{2V}{\pi a h^2}}} \right] & 0 < h \leq D_0 \\ 0 & h > D_0 \end{cases} \quad (2.1)$$

In Eq. 2.1, the maximum attractive force is  $F_0 = \pi \Gamma a \cos \theta$ , in which  $\Gamma$  is the liquid/air surface tension, and  $\theta$  is the contact angle, chosen equal to zero (we consider the case of perfect wetting). For all pairs in contact the capillary force is set to its maximum value  $F_0$ .  $V$ , in Eq. 2.1, is the volume of the meniscus and  $D_0$  is the rupture distance. For  $\theta = 0$ ,  $D_0$  is the cubic root of the volume ( $D_0 = V^{1/3}$ ). The model has hydraulic hysteresis: the liquid bridge forms right after two particles touch, and disappears for interparticle gaps larger than  $D_0$ .

The equation of motion of particles and the method implemented to control the normal stress are discussed in Sec. 1.3.3. The Gear predictor-corrector scheme of order 3 [5] is used to solve the second-order equations of motion. The simulations produce raw data in the form of time series that should be averaged over, in steady state, to obtain accurate statistics and macroscopic results. All the macroscopic and microscopic observables measured in the sequel (except instantaneous velocity profiles in Sec. 2.2.2) are averages over such time series. To estimate the statistical uncertainty in those measurements, we use the ‘‘blocking’’ (or ‘‘renormalization group’’) technique (see Sec. 1.3.3). Due to intrinsic long-lasting correlations in the system we need to impose quite large shear strains to the sample to obtain enough statistically uncorrelated data. For instance, for the main results with  $I = 0.562$ , the imposed shear strain is  $\gamma > 400$ , and for  $I = 10^{-3}$  it is, in most cases, larger than 50.

### 2.1.1 Control Parameters

The control parameters in our system are those listed and discussed in Sec. 1.3.2: inertial number  $I$ , reduced pressure  $P^*$ , number of particles  $N$ , local friction coefficient  $\mu$ , stiffness number  $\kappa$ , level of viscous damping  $\zeta$  and saturation  $S_w$ . From the results synthesized in Tab. 1.1, we expect the influence of  $\kappa$  and  $\zeta$  on macroscopic mechanical properties of the material to be negligible. (Let us mention, though, that all our simulations use a strong dissipation,  $\zeta = 0.98$ ). In order to enable comparison of macroscopic elastic properties with experimental results we set stiffness number  $\kappa = 8400$ , which corresponds to glass beads with Young modulus  $E = 70$  GPa and Poisson ratio  $\nu = 0.3$  under pressure  $P = 100$  kPa. This value is also constant in our simulations and high enough for its value to be irrelevant (as the characteristic properties of rigid grains are accurately approached). This leaves us with two important control parameters,  $I$  and  $P^*$ .

Let us now recall the expression of the saturation introduced in Sec. 1.2.4:

$$S_w = \frac{3z\Phi}{\pi(1-\Phi)} \frac{V}{a^3} \quad (2.2)$$

The appearance of coordination number  $z$  and solid fraction  $\Phi$  in Eq.2.2 precludes a direct control of  $S_w$ . We may only estimate its value for a given meniscus volume  $V$  and typical values of  $z$  and  $\Phi$ . In Sec. 2.3.1, we shall show that the variation of  $S_w$  with  $P^*$  and  $I$  does not significantly affect the results, within the range of investigated material states.

We choose volume  $V$  in order for the saturation to remain within the interval corresponding to the pendular state ( $3 \times 10^{-4} \lesssim V/a^3 \lesssim 10^{-2}$ ).

In most simulations we use  $V/a^3 = 10^{-3}$  (corresponding to  $D_0 = 0.1a$ , Eq. 1.28), but other values of  $V/a^3$ , between  $10^{-2}$  and  $10^{-6}$ , are also tested. In order to investigate the

influence of the attractive force range, we also carried out some simulations with a truncated Maugis interaction, setting the cut-off distance  $D_0$  to values zero or  $0.01a$ , while keeping the same meniscus volume  $V/a^3 = 10^{-3}$  in Eq. 2.1.

The main results are obtained over a wide range of  $I$  from  $10^{-4}$  to 0.562, and for several values of  $P^*$  between 0.436 and 10, in addition to the dry case with  $P^* = \infty$ . Tab. 2.1 gives the values of parameters used in the present study.

$\kappa$	8400
$\mu$	0.3
$N$	4000 (occasionally 8000)
$I$	from $10^{-4}$ to 0.562 by factors of $\sqrt{10}$
$P^*$	0.436 ; 1 ; 2 ; 5 ; 10 ; $\infty$
$V/a^3$	$10^{-3}$ ( $10^{-6}$ )

Table 2.1: List of dimensionless parameter values:  $N$  particles of diameter  $a$ , interacting with friction coefficient  $\mu$ , forming menisci of volume  $V$  at contacts, are subjected to normal stress-controlled shear flow for which inertial number  $I$ , reduced pressure  $P^*$  (evaluated with normal stress  $\sigma_{22}$ ) and stiffness parameter  $\kappa$  take values as prescribed.

In addition to the simulations mentioned above, the effect of capillary force model is studied, by replacing the Maugis approximation with the accurate parametrized capillary force law suggested by Soulié *et al.* (Eq. 1.26). We also carried out one simulation without hydraulic hysteresis, assuming the liquid bridges to form before approaching particles come into contact, as soon as the distance is lower than  $0.1a^3$ . Our standard choice for the number  $N$  of particles in the sample is 4000, with a few tests, motivated by the localization issue, with twice as many.

## 2.2 Macroscopic analysis

The strong influence of the capillary forces on the shear strength is perhaps the most reported property of wet granular materials. However, the investigations are mostly limited to the quasistatic behaviours and the influence of shear rate on the mechanical properties is less studied. In the following sections we investigate the global behaviour of a system of wet grains in steady state shear flow. First, we examine the approach to the steady state and the homogeneity of the flow, for which we establish a method to measure the intensity of the localization in the granular medium. Then, we study the rheological properties from a macroscopic point of view. We especially focus on the influence of inertial number  $I$ , and reduced pressure  $P^*$ , on macroscopic friction coefficient  $\mu^*$ , and solid fraction  $\Phi$ . In order to understand the effect of the liquid bridges on the mechanical properties of the material, we investigate the contribution of different forces to the stress components. At the end of this section we present the results for the normal stress differences and the sensitivity of the macroscopic results to the force model and the choice of the parameters.

### 2.2.1 Steady state, macroscopic measurements

To establish the constitutive laws of the flow of wet granular material, we impose a large enough shear strain to the sample in order to approach the steady flow regime in which

we can measure the macroscopic quantities by taking an average over the time series of results. So it is essential to ensure that the flow, at least from a macroscopic point of view, is homogeneous and time-invariant. On the other hand we also need to watch carefully that the normal stress  $\sigma_{22}$  is well-controlled.

The evolution of solid fraction  $\Phi$  with strain  $\gamma$  is shown in Fig. 2.1a. We start from an initial configuration with a large solid fraction close to the random close packing value ( $\Phi_{\text{RCP}} = 0.64$ ).  $\Phi$  decreases until approaching its steady state value and then it fluctuates about its mean value in steady state. Fig. 2.1b shows the evolutions of  $\sigma_{22}$  and  $\sigma_{12}$  with  $\gamma$ . It checks that the normal stress  $\sigma_{22}$  is well controlled since after approaching the steady state, it fluctuates about its mean value equal to the prescribed normal stress  $P$ . The shear stress  $\sigma_{12}$  exhibits a fast increase at the beginning of the deformation up to a maximum value, and then as the solid fractions decreases it starts to decrease monotonically toward its steady state value. To calculate the mean values, due to the large fluctuations of the results especially in the shear stress (about 20% of the mean value in the example of Fig. 2.1), we need to employ an appropriate method to estimate the errors carefully. We use the “blocking method” (see the discussions on “steady state and measurements” in Sec. 1.3.3) to calculate the error bars. This usually requires a very long simulation to obtain enough statistically uncorrelated data.

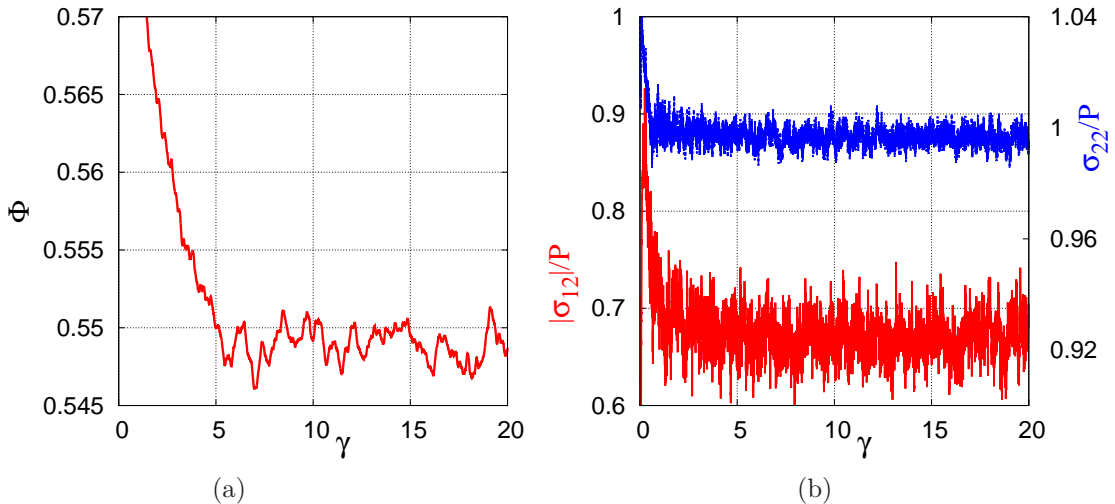


Figure 2.1: (a) Solid fraction  $\Phi$ , (b) shear stress  $|\sigma_{12}|$  (left axis in red) and normal stress  $\sigma_{22}$  (right axis in blue) versus shear strain  $\gamma$ . Note that the scale in the left and right axes in graph (b) are different. Time series is obtained with  $P^* = 1$ ,  $I = 0.1$  and  $N = 4000$  when the rupture distance is  $D_0 = 0.1$ .

## 2.2.2 Localization

In the flow of granular materials *localization* is a fundamental phenomenon in which the deformation becomes concentrated within one or several narrow bands within the granular material. In soil mechanics and geomechanical researches it is reported to be a common feature of those materials [146, 36]. In recent DEM studies of dense flow of dry grains, localization in the bulk is mostly reported in the quasistatic limit and for high enough confining pressure [4, 31, 104]. However, these observations show that the shear bands are not persistent. They usually spontaneously appear and disappear in the bulk of the material, so that they cannot disturb the homogeneity of the flow on average [104].

### Instantaneous velocity profile

Instantaneous velocity profile  $v^s(\equiv \langle v_1(x_2) \rangle_s)$  is calculated by averaging over the velocities of particles in  $x_1$  direction within the slices of thickness  $0.01L_2$  as below:

$$v^{si} = \frac{1}{m^{si}} \sum_j m_j^{si} \mathbf{v}_j \cdot \mathbf{e}_1, \quad (2.3)$$

in which  $v^{si}$  is the average velocity in slice  $i$ ,  $\mathbf{v}_j$  the velocity of particle  $j$ ,  $\mathbf{e}_1$  the unit vector in direction  $x_1$ ,  $m_j^{si}$  the fraction of the mass of the particle  $j$  which is located in slice  $i$  and  $m^{si}$  is the total mass in slice  $i$ .

Our simulations of the shear flow of wet grains show that localization might happen in the presence of strong capillary forces (in our simulations for  $P^* = 0.1$ ), even for fast flows. We observe that for all  $I \geq 0.178$  the velocity gradient completely concentrates within a shear band. In Fig. 2.2a, corresponding to  $P^* = 0.1$  and  $I = 0.562$ , the strain is strongly localized from the beginning, within a shear band of thickness  $H \lesssim 2a$  (with  $a$  the particle diameter), and this localization pattern persists for all values of strain  $\gamma$ .

For  $P^* = 0.1$  and  $I = 0.178$ , in the case shown in Fig. 2.2b, the velocity profile for all  $\gamma < 250$  is nearly linear but a fast strain localization transition takes place at this value of  $\gamma$ , and persists ever after. The shear bands are slightly thicker than in the previous case (for  $I = 0.562$ ), with  $H$  between  $2a$  and  $3a$ . They may move vertically but persist for larger deformations.

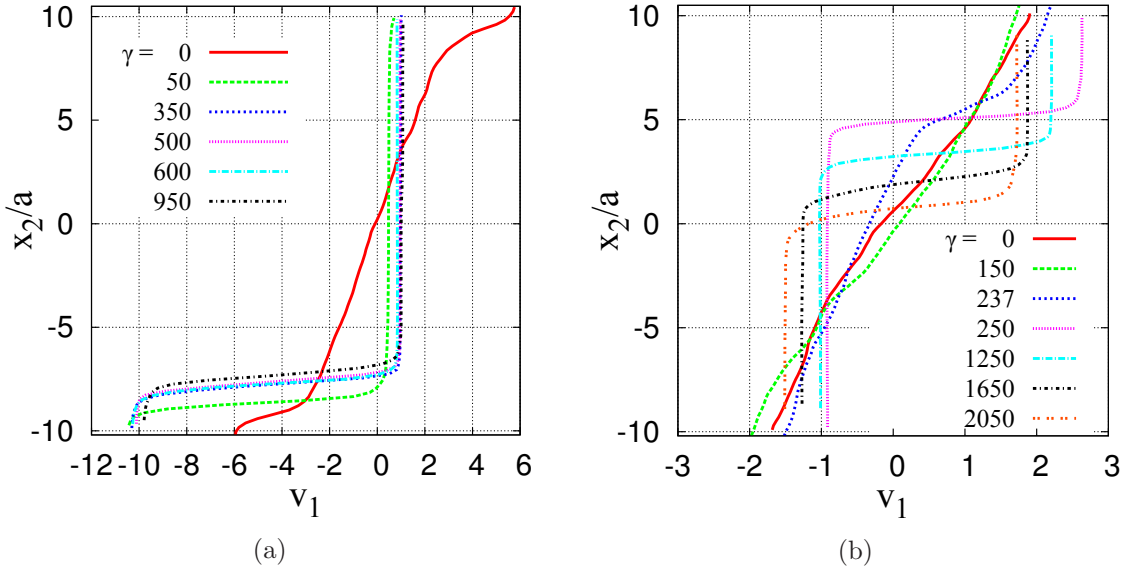


Figure 2.2: Velocity profile for  $P^* = 0.1$ ,  $I = 0.562$  (a) and  $I = 0.178$  (b) chosen for different strain intervals.

Although, due to the lack of homogeneity in the flow, it is not possible to calculate the global behaviour of the system, it is instructive to look at the evolutions of apparent macroscopic behaviour while the localization occurs. Fig. 2.3a and Fig. 2.3b respectively show shear stress  $|\sigma_{12}|$  and solid fraction  $\Phi$  as functions of  $\gamma$  for  $P^* = 0.1$  and  $I = 0.178$ . We see that, at the transition point (near  $\gamma = 250$ ), due to the failure in a shear band,  $|\sigma_{12}|$  suddenly drops from about 1.8 down to 0.8. In the presence of the shear band the system is divided into two parts, each of which moving like a rigid block, whence a strong increase of  $\Phi$  from 0.44 up to 0.49.

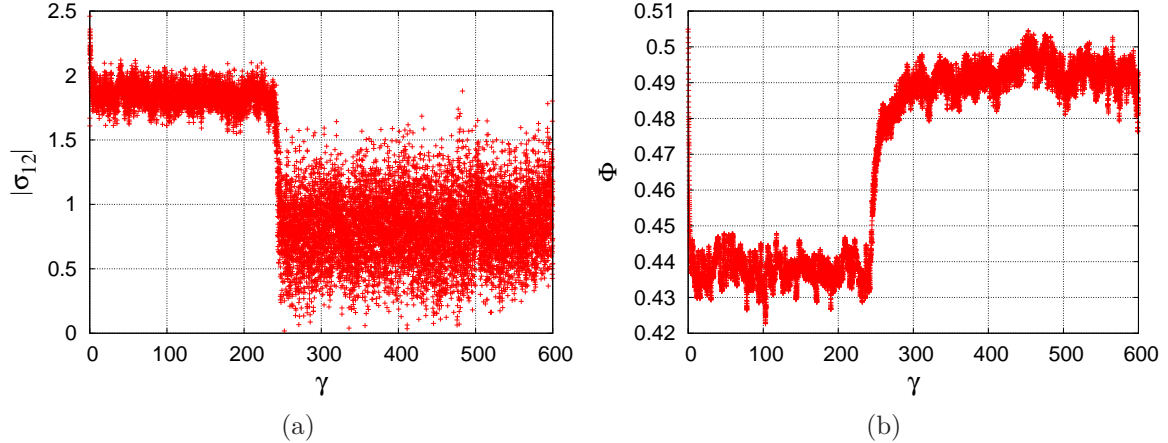


Figure 2.3: Absolute value of shear stress  $|\sigma_{12}|$  (a) and solid fraction  $\Phi$  (b) for  $P^* = 0.1$  and  $I = 0.178$  when the flow suddenly localizes at  $\gamma = 250$ .

For  $I = 10^{-1}$  when  $P^* = 0.1$  the velocity profiles are nearly linear and we do not see any sign of localization. The spontaneous shear bands may appear but they are temporary and in average the flow is homogeneous. It is in contradiction to our expectation that the localization would increase for slower flows. However, for smaller values of  $I$ , the shear bands appear more often and localization tendencies increase, in agreement with other studies on dry granular materials ( $P^* = \infty$ ) [4, 31, 104]. The velocity profile for a simulation with  $P^* = 0.1$  and  $I = 10^{-2}$  is represented in Fig. 2.4a. In this case, we detect the localization pattern regularly within the flow. The shear bands may disappear, but they form again and the typical strain rate field is not uniform. For smaller values of  $I$ , for instance  $I = 10^{-3}$  (Fig. 2.4b), the strain rate is strongly localized in a shear band with a thickness mostly between  $5a$  to  $10a$ .

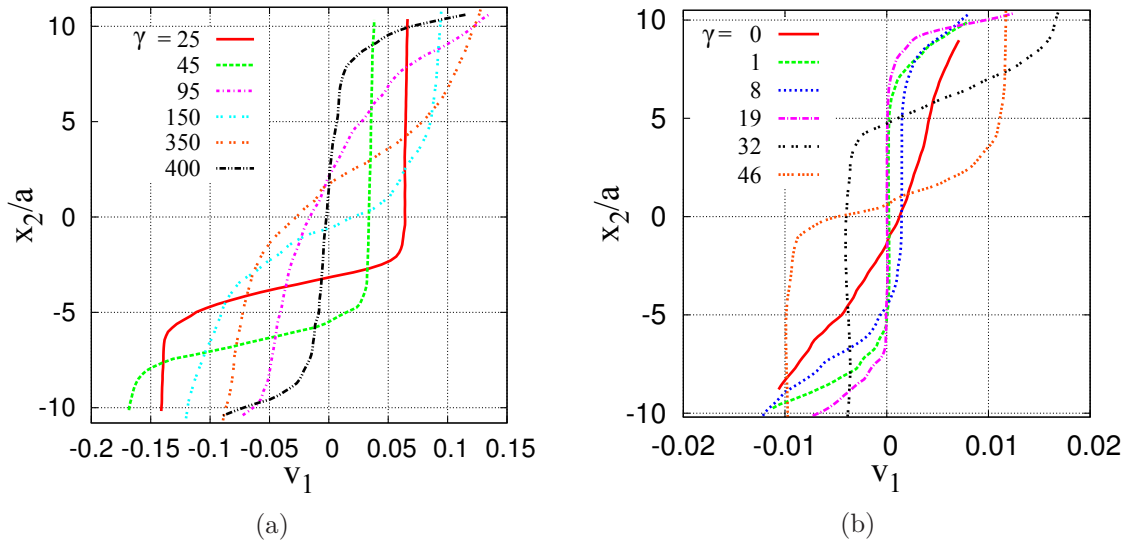


Figure 2.4: Velocity profile for  $P^* = 0.1$ ,  $I = 10^{-2}$  (a) and  $I = 10^{-3}$  (b) chosen for different strain intervals.

For all  $P^*$  larger than 0.1 the localization pattern are infrequent and temporary even in the quasistatic limit. The velocity profiles for  $P^* = 0.436$  and  $I = 10^{-3}$ , as it is represented in Fig. 2.5, is nearly linear and on average the flow is homogeneous.



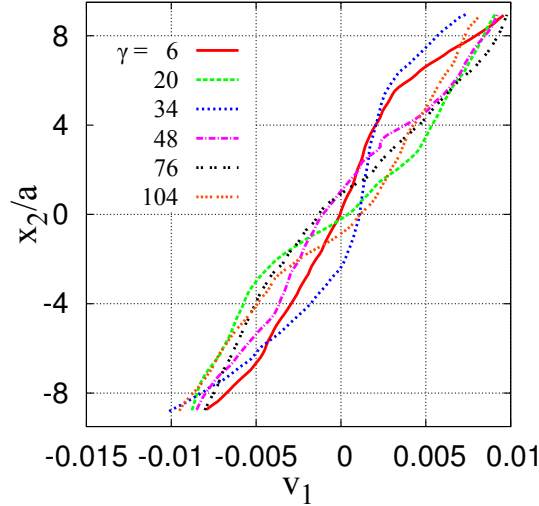


Figure 2.5: Velocity profile for  $P^* = 0.436$ ,  $I = 10^{-3}$  and different values of strain  $\gamma$ .

### Local solid fraction

Similarly we can calculate a solid fraction profile, on averaging the solid contents of slices orthogonal to the velocity gradient (the volume of one grain might be shared between different slices). Fig. 2.6 shows the velocity ( $v^s$ ) and solid fraction ( $\Phi^s$ ) profiles for two different values of shear strain,  $\gamma = 1$  and  $\gamma = 352$ , which belong to the simulation of Fig. 2.3. We see that in the homogeneous flow the distribution of mass in the system is almost uniform, but when the localization occurs  $\Phi^s$  strongly decreases within the shear bands below 0.2. It slightly increases outside the shear band especially in its vicinity.

Fig. 2.7 also displays the velocity profiles and the corresponding  $\Phi^s$  for two localized sample, in the simulations with  $P^* = 0.1$  and two different values of  $I$ . For  $I = 0.316$ , the flow localizes in a narrow shear band with  $H \approx 2a$ .  $\Phi^s$  strongly decreases down to a value smaller than 0.2 and the density of particles near the shear band increases. For  $I = 10^{-3}$  a shear band with a larger thickness ( $H \approx 7a$ ) forms and  $\Phi^s$  undergoes a smaller decrease inside the sheared zone (from 0.47 to about 0.4).

### Deviation from linear profile

The deviation from a linear profile is characterized by parameter  $\tilde{\Delta}$ , which is defined as

$$\tilde{\Delta} = \frac{1}{L_2 \dot{\gamma}^2} \int_{-L_2/2}^{L_2/2} (v_1(x_2) - \dot{\gamma} x_2)^2 dx_2 \quad (2.4)$$

Fig. 2.8 displays an ideal case of maximum localization in which the strain is localized in a plane, as if two solid blocks were sliding on each other. Considering this perfectly localized case we can calculate the maximum value of velocity deviation  $\tilde{\Delta}_{\max}$  when the velocity field is defined as

$$v_1 = \begin{cases} u & -L_2/2 \leq x_2 < X \\ w & X \leq x_2 \leq -L_2/2 \end{cases} \quad (2.5)$$

Due to the implemented periodic boundary condition  $v_1(x_2 + L_2) - v_1(x_2) = \dot{\gamma} L_2$  for any  $x_2$  or in our ideal case  $w - u = \dot{\gamma} L_2$ . Furthermore, as the system dynamics requests the total

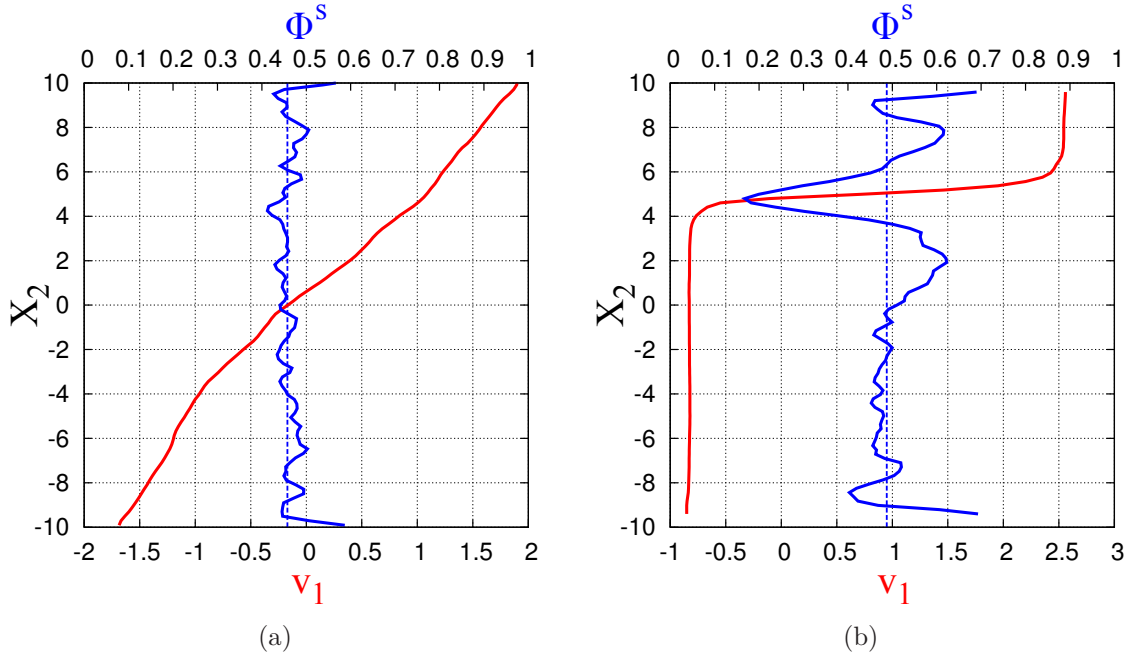


Figure 2.6: Velocity profiles (lower axis in red) and local densities of grains (upper axis in blue) for two configuration samples with shear strain  $\gamma = 1$  (a) and  $\gamma = 352$  (b) when  $P^* = 0.1$  and  $I = 0.178$ . Average solid fraction  $\langle \Phi^s \rangle$ , is shown with a vertical dashed line in blue, with a value of 0.46 in (a) and 0.49 in (b).

momentum associated with the non-affine part of the motion to vanish, provided the density might be regarded as uniform, function  $v_1(x_2)$  averages to zero:

$$\int_{-L_2/2}^{L_2/2} v_1(x_2) dx_2 = u(L_2/2 + X) + w(L_2/2 - X) = 0, \quad (2.6)$$

and then we obtain:

$$\begin{cases} u = -\dot{\gamma}L_2/2 + \dot{\gamma}X \\ w = \dot{\gamma}L_2/2 + \dot{\gamma}X \end{cases} \quad (2.7)$$

Finally using these velocities in Eq. 2.4 gives us:

$$\tilde{\Delta}_{\max} = \frac{1}{L_2^3 \dot{\gamma}^2} \left( \int_{-L_2/2}^X (u - \dot{\gamma}x_2)^2 dx_2 + \int_X^{L_2/2} (w - \dot{\gamma}x_2)^2 dx_2 \right) = \frac{L_2^2}{12} \quad (2.8)$$

Consequently, we can measure the rate of velocity deviation from linear profile, for a certain configuration with strain  $\gamma$ , by using Eq. 2.4 normalized with  $\tilde{\Delta}_{\max}$ , defining  $\Delta = \tilde{\Delta}/\tilde{\Delta}_{\max}$  as

$$\Delta(\gamma) = \frac{12}{L_2^3 \dot{\gamma}^2} \int_{-L_2/2}^{L_2/2} (v_1(x_2, \gamma) - \dot{\gamma}x_2)^2 dx_2. \quad (2.9)$$

When the strain rate is homogeneous within the shear band of height  $H$  and vanishes outside the band (Fig. 2.8), we can calculate  $\Delta$  from the same procedure in calculation of Eq. 2.8, and then we obtain:

$$\Delta = \left(1 - \frac{H}{L_2}\right)^2. \quad (2.10)$$

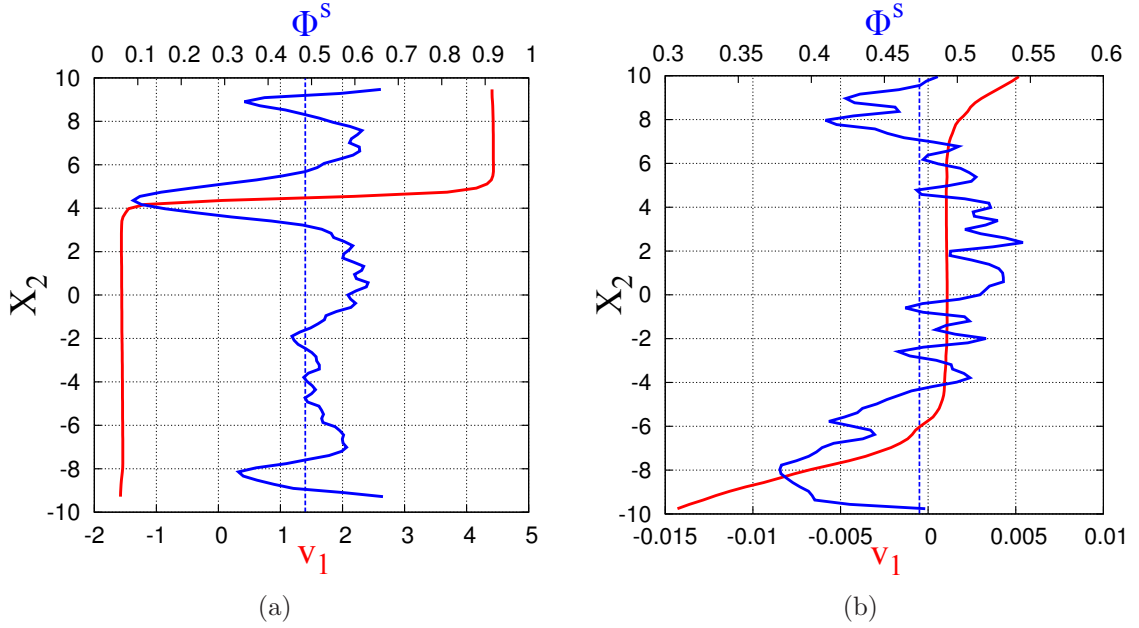


Figure 2.7: Velocity profiles (lower axis in red) and local densities of grains (upper axis in blue) for two configuration samples with  $I = 0.316$  (a) and  $I = 10^{-3}$  (b) when  $P^* = 0.1$ . Average solid fraction  $\langle \Phi^s \rangle_s$  is shown with a vertical dashed line in blue, with a value of 0.49 in (a) and 0.47 in (b).

By using this equation we can associate some equivalent band thickness  $H$  to measurements of  $\Delta$ .  $\Delta$  decreases and the flow homogeneity increases for thicker shear bands.

Fig. 2.9a displays the evolution of  $\Delta$  with strain  $\gamma$ , for the same value of  $P^*$  and  $I$  as in Fig. 2.2b and Fig. 2.3. For  $\gamma < 250$ , when the flow is homogeneous, the value of  $\Delta$  is very small, but near  $\gamma = 250$  when the localization happens it increases to a value above 0.8. Fig. 2.9b also shows the result for  $\Delta(\gamma)$  For  $I = 10^{-3}$ . We may compare these direct measurements to the values that we obtain from Eq. 2.10. In the fast flows we measured the thickness of the bands about two particles diameter (see Fig.2.2b). So, Eq. 2.10 results a  $\Delta$  about 0.8. For  $I = 10^{-3}$ ,  $H$  is mostly about 5 particles diameter (see Fig. 2.4b), which results a smaller value of  $\Delta$  about 0.6.

The evolutions of  $\Delta$  for  $P^* = 0.1$  and  $I = 10^{-2}$  is represented in Fig. 2.10a, when the velocity patterns may tend to a linear profile (see Fig. 2.4a) and consequently  $\Delta$  tends to zero for some values of  $\gamma$ , but it regularly increases to higher values, resulting a non-homogeneous flow on average.

We can estimate the localization tendency of the flow, by taking a time average of  $\Delta$ . For  $P^* = 0.1$  and fast flows, the average  $\langle \Delta \rangle_t$  is notably large, ranging from 0.7 for  $I = 0.178$  to 0.9 for  $I = 0.562$ . It drops down to 0.02 for  $I = 0.1$ , but increases for slower flows up to 0.6 when  $I = 10^{-3}$ . For all values of  $P^*$  larger than 0.1, for instance in Fig. 2.10b,  $\Delta$  is very small and the average  $\langle \Delta \rangle_t$  does not exceed from 0.05.

### Effect of system size

The influence of the system size is studied by simulating some samples of 8000 grains. In this case, the height of the sample  $L_2$ , is twice as large as in the standard sample, but  $L_1$  and  $L_3$  are the same. As we observed in Fig. 2.10a, in a sample of 4000 particles with  $P^* = 0.1$  and  $I = 10^{-2}$ ,  $\Delta$  is most often below 0.2, but it might also indicate strong localization when  $\Delta$  fluctuates between 0.4 and 0.8. The larger sample with  $N = 8000$  and the same values of  $P^*$

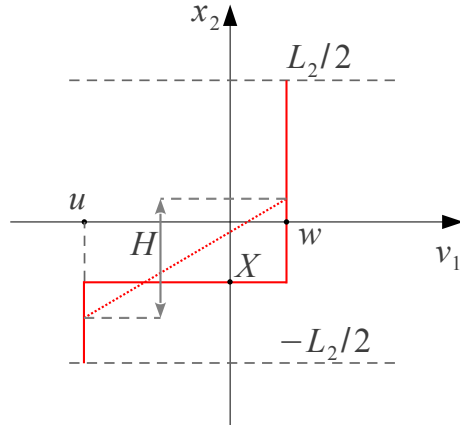


Figure 2.8: Velocity profile for two ideal cases, when the flow is localized in a plane between two solid blocks (red solid line) and when it is limited to a homogeneous flow in a shear band with thickness  $H$ .

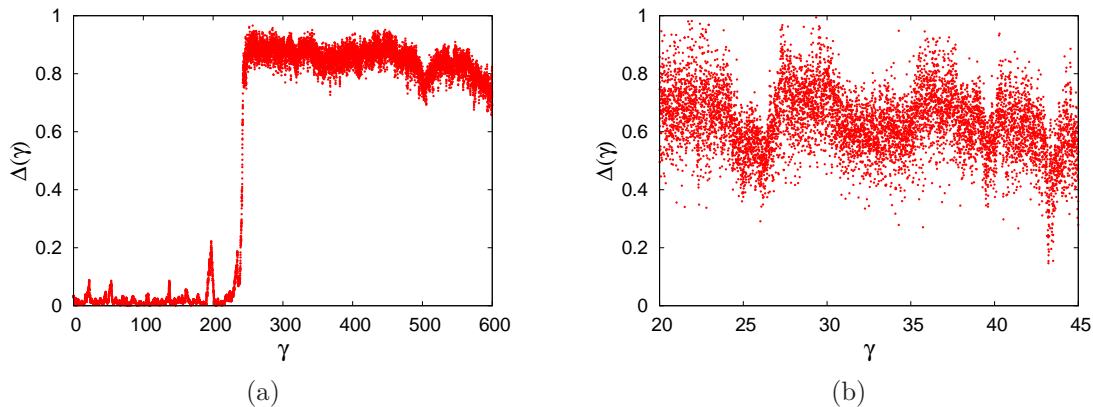


Figure 2.9: Deviation from linear profile  $\Delta(\gamma)$  versus strain  $\gamma$  for  $P^* = 0.1$ ,  $I = 0.178$  (a) and  $I = 10^{-3}$  (b).

and  $I$ , shows even a stronger localization effect, so that,  $\Delta$  fluctuates mostly between 0.6 and 1, however, it regularly decreases below 0.2. We also examined this effect for  $P^* = 0.436$ , in which  $\langle \Delta \rangle_t$  is measured about 0.1 for  $I = 10^{-2}$  and about 0.2 for  $I = 10^{-3}$ , which is larger than the results for smaller system with the same values of control parameters ( $\langle \Delta \rangle_t < 0.05$ ). For dry grains this average is below 0.02 regardless of the system size.

It should be noted that, in Eq. 2.10,  $\Delta$  varies with the system size  $L_2$  and so the increase in its value for the larger sample was expected. However, a better quantitative result needs more simulations or probably an alternative method for the measurements of the localization tendency, independent of the system size.

To summarize, in this section we studied the localization phenomena in the shear flow of wet granular material. The velocity patterns are displayed for different values of  $P^*$  and  $I$ . The deviation of the velocity patterns from the linear profile is characterized with a single number  $\Delta$ , and the localization tendency of the flow is described by the time average of this parameter  $\langle \Delta \rangle_t$ . We observed that the localization patterns are frequent and persistent for  $P^* = 0.1$  and almost all values of  $I$ . For smaller values of  $I$ , the localization patterns are more persistent and regular and the localization tendency increases. Although, unexpectedly,

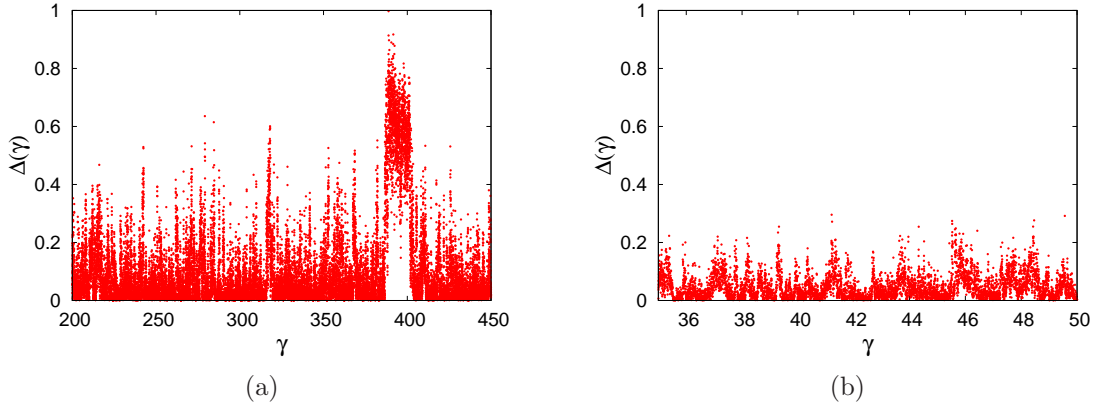


Figure 2.10: Deviation from linear profile  $\Delta(\gamma)$  versus strain  $\gamma$  for  $P^* = 0.1$ ,  $I = 10^{-2}$  (a) and  $P^* = 0.436$ ,  $I = 0.316 \times 10^{-3}$  (b).

for  $I = 0.1$  the localization tendency  $\langle \Delta \rangle_t$  decreases down to zero, for smaller values of  $I$  it increases again up to 0.6 for  $I = 10^{-3}$ . In the fast flows ( $I \leq 0.178$ ), when the flow is strongly localized, the shear bands are quite narrow  $a \lesssim H \lesssim 3a$ , but for  $I \leq 10^{-2}$  the thickness of the shear bands is larger about  $5a$  to  $10a$ . We also observed that the solid fraction  $\Phi$  increases for the flows with a large localization tendency. The local density of the particles  $\Phi^s$  strongly decreases within the shear bands, especially in the narrow bands and increases outside the shear band near the shearing zone. No localization effect is observed for  $P^* \geq 0.436$ . The velocity profiles are nearly linear and the localization tendency is below 0.05, for a system of 4000 particles. The influence of the system size is also investigated, showing that the localization tendency increases for larger systems.

As mentioned in Sec. 1.2.4, it is shown in a recent study that the liquid content decreases within unsaturated shear bands [88]. This effect might have a strong influence on shear strength of the material, and so the distribution of liquid and the dynamics of the liquid migration within the liquid bridges should be considered in simulation of wet granular materials. However, the liquid distribution in our model is quite simple and inapplicable to study this phenomenon.

Also, it should be noted that in our simulation the value of stiffness number  $\kappa$  is chosen 8400, that is determined by comparing the Hertzian elastic force to the typical force due to confining pressure  $Pa^2$  (Eq. 1.36). Since for  $P^* = 0.1$ , the maximum capillary force is ten times as large as  $Pa^2$ , it is more convenient to characterize the stiffness of particles with  $\kappa_0 = \kappa P^{*2/3}$  (Eq. 1.39). It results in a small value of stiffness,  $\kappa_0 \simeq 1800$ , which might have some influence on the flow homogeneity. However, for all other values of reduced pressure ( $P^* \geq 0.436$ ), the choice of stiffness number is quite reasonable.

### 2.2.3 Macroscopic behaviour and constitutive relations

We now focus on homogeneous steady states (excluding too small  $P^*$  values, from Sec. 2.2.2) and deduce macroscopic constitutive relations from the simulations. We investigate the rheological properties of the material for different values of the inertial number, ranging from the quasistatic limit ( $I \rightarrow 0$ ) to fast flows:  $10^{-4} \leq I \leq 0.562$ . As we discussed in Sec. 1.3.2, the macroscopic behaviour of the system depends on five dimensionless parameters,  $\zeta$ ,  $\kappa$ ,  $I$ ,  $P^*$  and  $\mu$ . Previous studies on the rheology of dry grains [31, 104] showed that the properties of steady dense flows of rigid grains are not significantly influenced by parameters  $\zeta$  and  $\kappa > 1000$ , especially in the quasistatic limit. In this study we examine the influence of the other two parameters, reduced pressure  $P^*$  and inertial number  $I$  on the rheological

behaviour, as measured for large enough system size  $N$ . Local friction coefficient  $\mu$  is kept equal to 0.3.

In analogy to some recent studies on cohesive granular materials [122, 120], the macroscopic friction coefficient is conventionally defined as the time average of the ratio of the shear stress  $\sigma_{12}$  to the normal stress  $\sigma_{22}$  in steady state:

$$\mu^* = \left\langle \frac{|\sigma_{12}|}{\sigma_{22}} \right\rangle_t, \quad (2.11)$$

in which the stress components are calculated by Eq. 1.15. It should be mentioned here that due to the large fluctuation in  $\sigma_{12}$  compared to the fluctuations in  $\sigma_{22}$ , using the ratio of average values in Eq. 2.11, instead of the average of the stress ratio, would strongly affect the measurements. We also measure the average density of the grains in steady state, by taking an average on the time series of solid fractions,  $\Phi \equiv \langle \Phi(t) \rangle_t$ .

Fig. 2.11a and Fig. 2.11b respectively show  $\mu^*$  and  $\Phi$  as functions of  $I$  for different values of  $P^*$ . The increase of  $\mu^*$  and decrease of  $\Phi$  for larger  $I$  show the usual behaviour of granular materials under shear flow, similar to other experimental and numerical studies on dry grains [31, 62, 52, 22] (see Sec. 1.4.1). In the quasistatic limit, for  $I \rightarrow 0$ ,  $\mu^*$  approaches its value in critical state  $\mu_0^*$ , which is different for each value of  $P^*$ . In the absence of the capillary forces for  $P^* = \infty$ , we measured  $\mu_0^*$  about 0.34 when the local friction  $\mu = 0.3$ . This value is slightly larger than the result by Hatano ( $\mu_0^* = 0.3$  for  $\mu = 0.4$ ) [62] and close to the result by Campbell ( $\mu_0^* = 0.26$  and  $0.36$  respectively for  $\mu = 0.1$  and  $\mu = 0.5$ ) [22], considering that  $\mu_0^*$  is a growing function of  $\mu$  with a decreasing rate [81].

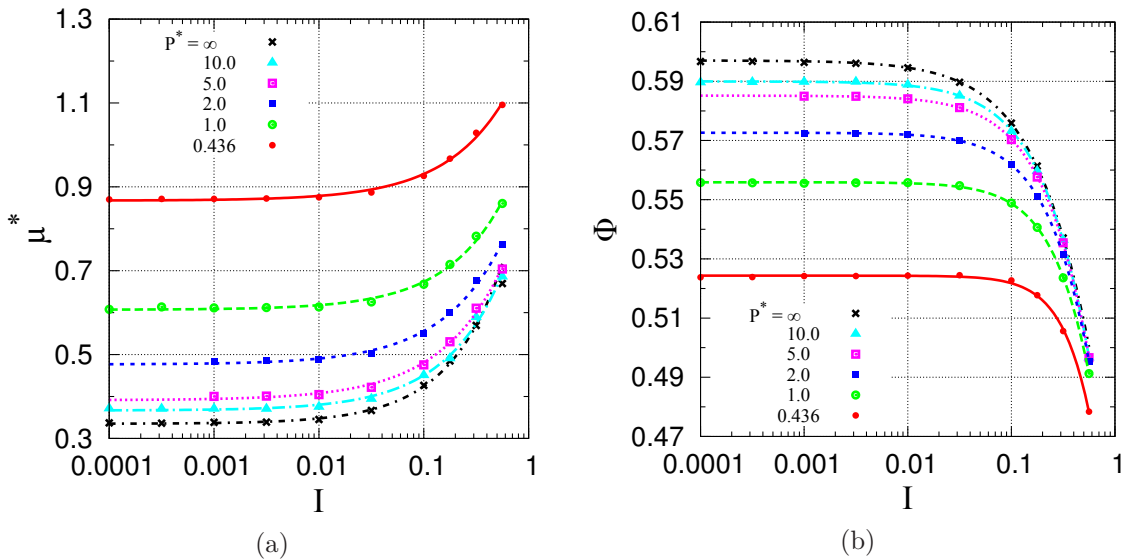


Figure 2.11: Macroscopic friction coefficient  $\mu^*$  (a) and solid fraction  $\Phi$  (b) versus inertial number  $I$  for different values of reduced pressure  $P^*$ . Intergranular friction coefficient  $\mu$  is set to 0.3.

Our results reveal a strong effect of the capillary force on the rheology, such that for  $P^* = 0.436$  when the capillary force is about twice as large as the force due to confining pressure,  $\mu_0^*$  is about 2.5 times as large as its value for dry grains. Within the same range of  $P^*$ ,  $\Phi_0$  decreases from 0.6 to 0.52, a value that cannot be observed in the absence of cohesion. These results are in contrast with the results reported for the shear flow of two dimensional cohesive grains [120, 122] (see Sec. 1.4.3), in which the large effect of cohesion on macroscopic behaviour is only reported for a value of  $P^*$  below 0.1. However, distant

interactions are absent in a cohesive system, which might have an important role in the system behaviour.

The strong effect of the capillary forces on the rheological behaviour of the granular material is also observed in other experimental and numerical studies [50, 63, 118, 40, 131]. For instance, Fournier et al. [50] measured the yield stress in an experimental setup of Poiseuille-like flow of a dense granular material, by imposing an oscillatory homogeneous shear deformation to spherical glass beads, assembled in a cylindrical cell. For a system of beads with a diameter of 200 microns, wetted by water and under absolute pressure of 800 Pa, which corresponds to  $P^* \simeq 0.7$ , their results show that the measured yield stress significantly increases in the presence of an interstitial liquid with a maximum and nearly constant value within the pendular regime (see Sec. 1.2.4).

Since the macroscopic behaviour for each value of  $P^*$  strongly depends on  $I$ , first we express the evolutions of  $\mu^*$  and  $\Phi$  as functions of  $I$ . We fit the following power law functions to the data of  $\mu^*$  and  $\Phi$ , in which  $\mu_0^*$  and  $\Phi_0$  are respectively the critical state values of the macroscopic friction coefficient and the solid fraction in the quasistatic limit:

$$\begin{cases} \mu^* = \mu_0^* + cI^\alpha \\ \Phi^{-1} = \Phi_0^{-1} + eI^\nu \end{cases} \quad (2.12)$$

Tab. 2.2 and Tab. 2.3 show the estimated values of the parameters for the fits on  $\mu^*$  and  $\Phi$  data. It should be noted that the approach to the quasistatic limit is faster for small values of  $P^*$ . As shown in Fig. 2.11, the quasistatic limit is nearly reached for  $I \leq 0.01$ . This is quantitatively expressed by the decrease of parameter  $c$  for smaller  $P^*$  values in Tab. 2.2. It is more evident for the solid fraction in Tab. 2.3 in which for smaller  $P^*$  values,  $\nu$  strongly increases while the variations of parameter  $e$  is relatively small.

$P^*$	$\mu_0^*$	$\alpha$	$c$
0.436	$0.867 \pm 0.003$	$0.76 \pm 0.04$	$0.36 \pm 0.01$
1	$0.607 \pm 0.003$	$0.79 \pm 0.05$	$0.41 \pm 0.02$
2	$0.477 \pm 0.005$	$0.76 \pm 0.05$	$0.45 \pm 0.02$
5	$0.391 \pm 0.006$	$0.73 \pm 0.05$	$0.49 \pm 0.02$
10	$0.367 \pm 0.004$	$0.79 \pm 0.04$	$0.51 \pm 0.02$
$\infty$	$0.335 \pm 0.001$	$0.84 \pm 0.02$	$0.62 \pm 0.02$

Table 2.2: Fit parameters of the power law function for  $\mu^*$  in Eq. 2.12, for different values of  $P^*$ .

$P^*$	$\Phi_0$	$\nu$	$e$
0.4360	$0.5243 \pm 2.10^{-4}$	$1.727 \pm 0.051$	$0.497 \pm 0.017$
1	$0.5559 \pm 10^{-4}$	$1.337 \pm 0.012$	$0.512 \pm 0.005$
2	$0.5726 \pm 10^{-4}$	$1.210 \pm 0.007$	$0.547 \pm 0.003$
5	$0.5851 \pm 10^{-4}$	$1.120 \pm 0.005$	$0.580 \pm 0.003$
10	$0.5900 \pm 10^{-4}$	$1.085 \pm 0.007$	$0.594 \pm 0.004$
$\infty$	$0.5970 \pm 10^{-4}$	$0.958 \pm 0.011$	$0.562 \pm 0.008$

Table 2.3: Fit parameters of the power law function for  $\Phi$  in Eq. 2.12, for different values of  $P^*$ .

Seeing that, for a rather large range of  $I$  values, the macroscopic behaviour is independent of  $I$  and is a sole function of  $P^*$ , it is reasonable to characterize the rheological behaviour in



the quasistatic limit with respect to  $P^*$ . Fig. 2.12 (a) and (b) respectively display  $\mu^*$  and  $\Phi$  as functions of  $P^*$ , in which the results for  $I = 10^{-2}$  and  $10^{-3}$  are indistinguishable. We fit the following power law functions to  $\mu^*$  and  $\Phi$  at small values of  $I$ , in which  $\mu_\infty^*$  and  $\Phi_\infty$  are respectively the quasistatic values of internal friction and solid fraction, in the limit of dry systems when  $P^* \rightarrow \infty$ :

$$\begin{cases} \mu^* = \mu_\infty^* + BP^{*-\beta} \\ \Phi = \Phi_\infty - CP^{*-\lambda} \end{cases} \quad (2.13)$$

Fig. 2.12 also shows a fit on the data of  $\mu^*$  and  $\Phi$  for  $I = 10^{-3}$ . The values of  $B$  and  $\beta$  in this fit are respectively  $0.274 \pm 0.006$  and  $0.82 \pm 0.02$  while  $C = 0.041 \pm 0.001$  and  $\lambda = 0.82 \pm 0.02$ .

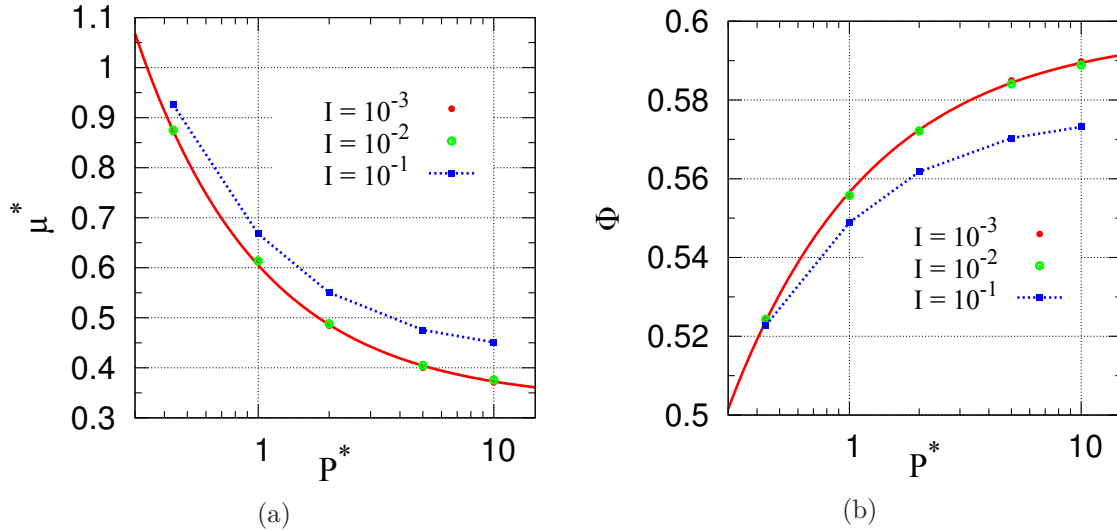


Figure 2.12: Macroscopic friction coefficient  $\mu^*$  (a) and solid fraction  $\Phi$  (b) versus reduced pressure  $P^*$ , for different values of inertial numbers  $I$ .

The influence of the sample size is investigated by comparing the results for 4000 grains to larger system with 8000 grains for  $P^* = 0.436$  and two different values of  $I$ . The measurements show that the results are independent of the system size and we obtained the same values for  $\mu^*$  and  $\Phi$  in both cases.

## 2.2.4 Contribution of different interactions to stresses

The contribution of the kinetic term in Eq. 1.15 to the shear stress is quite small. Even for the fastest flow in our simulation ( $I = 0.562$ ), this contribution does not exceed 2% of the shear stress or 5% of the normal stress components, and for  $I = 0.178$  is nearly zero for all the stress components. Therefore, in this section we only discuss the contribution of forces to the stress components, for the different values of the control parameters,  $P^*$  and  $I$ . The contribution of forces could be split in various ways, on distinguishing different forces. First we can consider the total stress as a sum of the contributions of the contacts and of the distant interacting pairs, as

$$\sigma_{\alpha\beta} = \sigma_{\alpha\beta}^c + \sigma_{\alpha\beta}^d. \quad (2.14)$$

Our results show that the contact forces have the dominant contribution to the total shear stress, mostly larger than 90%, regardless of the value of  $P^*$  or  $I$ . The contribution of distant interactions to  $\sigma_{12}$ , as represented in Fig. 2.13a, is not negligible and increases for smaller values of  $P^*$ . However, it hardly exceeds 10% of the total shear stress.

The contribution of distant interactions to  $\sigma_{22}$  is displayed in Fig. 2.13b. Due to the attractive nature of the capillary forces  $\sigma_{22}^d$  is a tensile stress. For  $P^* = 0.436$ , in the quasistatic limit, this contribution increases up to 20% in magnitude. Consequently, the contribution of contact forces to  $\sigma_{22}$  is positive and for  $P^* = 0.436$  increases up to a value of about  $1.2\sigma_{22}$ .  $\sigma_{11}^d$  and  $\sigma_{33}^d$  also have a similar trend as in Fig. 2.13b. In the quasistatic limit and for  $P^* = 0.436$ , one has  $\sigma_{11}^d/\sigma_{11} \simeq -0.16$  and  $\sigma_{33}^d/\sigma_{33} \simeq -0.25$ .

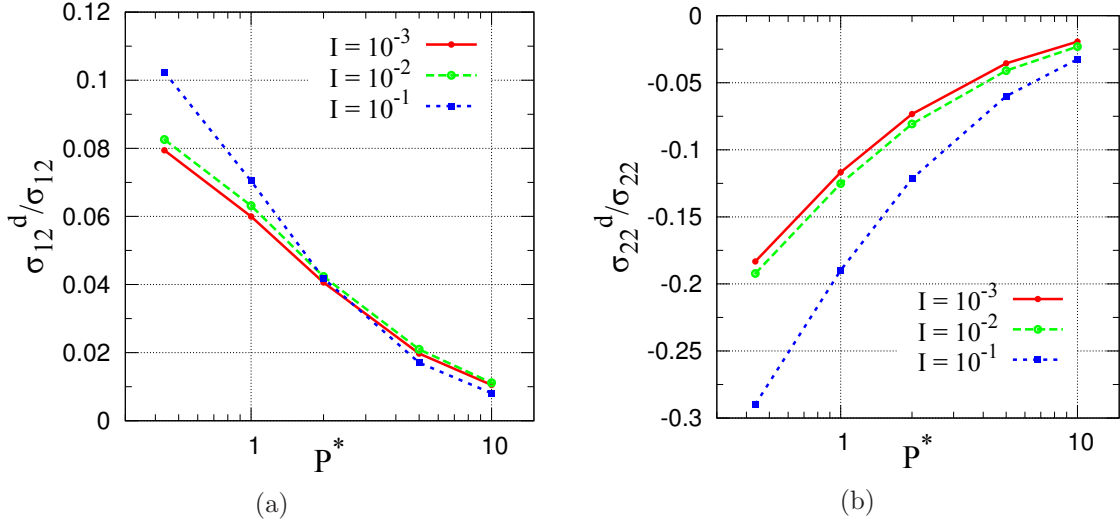


Figure 2.13: Contribution of distant interactions to shear stress  $\sigma_{12}$  (a) and to normal stress  $\sigma_{22}$  (b).

An alternative decomposition of stress components is:

$$\sigma_{\alpha\beta} = \sigma_{\alpha\beta}^{\text{cap}} + \sigma_{\alpha\beta}^{\text{Ne}} + \sigma_{\alpha\beta}^{\text{T}}, \quad (2.15)$$

in which  $\sigma_{\alpha\beta}^{\text{cap}}$  is the contribution of capillary forces (either for the contacts or the distant interacting pairs),  $\sigma_{\alpha\beta}^{\text{Ne}}$  is the contribution of normal elastic forces and  $\sigma_{\alpha\beta}^{\text{T}}$  is the contribution of tangential forces.

The normal elastic forces have the dominant contribution to the stress components. They contribute more than 90% to the shear stress, for any value of  $P^*$  and  $I$ . The contribution of tangential forces to the normal stress components is negligible but for the small values of the reduced pressure, the contribution of capillary forces is significantly large. For instance, for  $P^* = 0.436$ , all the three compressive stress components of  $\sigma_{\alpha\alpha}^{\text{cap}}$  (with  $1 \leq \alpha \leq 3$ ) are more than twice as large as their corresponding total stress component ( $\sigma_{\alpha\alpha}$ ) in magnitude, which are compensated with the large contributions of repulsive normal elastic forces  $\sigma_{\alpha\alpha}^{\text{Ne}} (> 3\sigma_{\alpha\alpha})$ . Under such strong capillary pressure, the particles are strongly compressed onto one another which enhance the tangential forces in the contacts. Fig. 2.14a shows the contribution of tangential forces to the total shear stress in which for  $P^* = 0.436$ , the ratio  $\sigma_{12}^{\text{T}}/\sigma_{12}$  increases up to 0.18. Remarkably, we see that the contribution of capillary forces to the total shear stress is negative. Fig. 2.14b displays  $\sigma_{12}^{\text{cap}}/\sigma_{12}$  for different values of  $P^*$ , which is always negative and decreases down to -0.12 for  $P^* = 0.436$ . It may appear to be in contradiction with the strong influence of capillary forces on the shear stress, discussed in Sec. 2.2.3. Although the capillary forces directly reduce the shear stress, it will be discussed in Sec. 2.3 that the structural changes in the contact network and the force chain, due to the capillary forces, strongly increase the material resistance to shear stress. We will also argue in Sec. 2.3.3 that this negative contribution and the positive contribution of distant interaction to  $\sigma_{12}$  (Fig. 2.13a) are related to the favoured orientation of the interacting pairs.

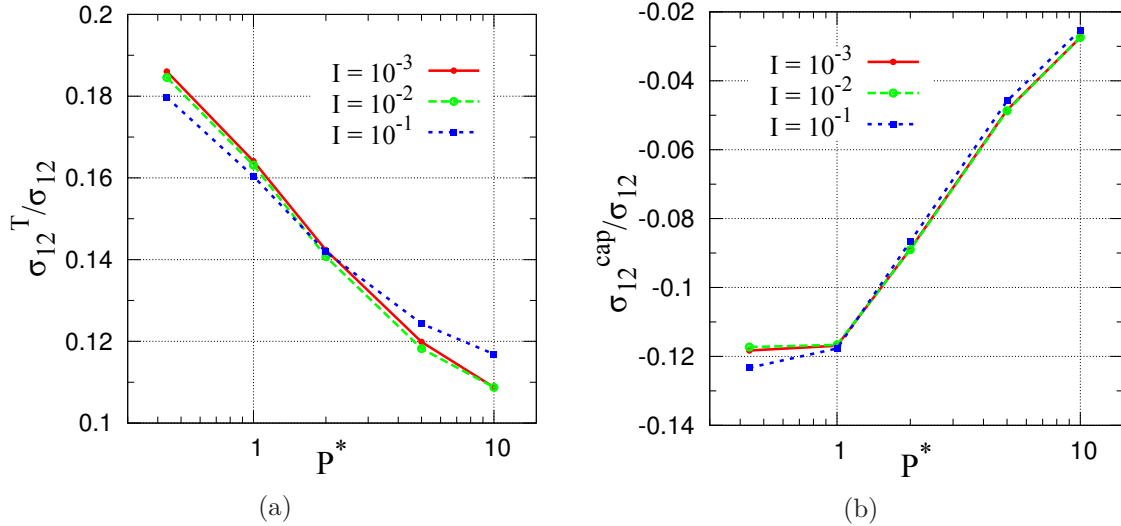


Figure 2.14: Contributions of tangential (a) and capillary (b) interactions to total shear stress  $\sigma_{12}$ .

It should be noted that the strong influence of the capillary forces on the shear strength of granular material cannot be expressed with the small contribution of distant interactions, or negative contribution of capillary forces. It is in contrast with the interpretations based on the effective stress principle (see Sec. 1.2.4), according to which the effect of the capillary forces is considered as equivalent to an additive isotropic pressure. Consequently, one needs to investigate the microstructural properties of the material in the presence of the capillary forces. This issue will be discussed in detail in Sec. 2.3.

## 2.2.5 Normal stress differences

The first and the second normal stress differences are defined as

$$\begin{cases} N_1 &= \sigma_{11} - \sigma_{22} \\ N_2 &= \sigma_{22} - \sigma_{33} \end{cases} \quad (2.16)$$

Fig. 2.15 displays  $N_1$  and  $N_2$  versus  $I$  for different values of  $P^*$ . The first normal stress difference is very small in the quasistatic limit and for large values of the reduced pressure. It increases with  $I$  and for smaller values of  $P^*$ , going through a transition from small negative values to positive values near  $I = 0.03$ , for all  $P^*$  above 2. The rate of the increase of  $N_1$  with inertial number is nearly constant for different  $P^*$  values. The measurements of the contribution of different forces show that the normal contact forces have the dominant contribution in  $N_1$ , in most cases more than 80%. The contribution of distant interactions is about 15% for  $P^* = 0.436$  and any value of  $I$ , and decreases down to zero for  $P^* = 10$ . The tangential forces contribute more than 10% in the fast flows for every value of  $P^*$ , decreasing down to 0 at the quasistatic limit. The second normal stress difference  $N_2$  also increases for faster flows and for smaller values of the reduced pressure. At the quasistatic limit, it is larger in comparison to  $N_1$  and strongly increases for smaller values of  $P^*$ . The rate of the variations of  $N_2$  decreases as the value of reduced pressure decreases. Here again the contribution of normal contact forces is dominant, more than 70% for smaller  $P^*$  values, increasing up to 85% for  $P^* = 10$ . The contribution of distant interaction is very small, even for strong capillary forces. Compared to the first normal stress difference, tangential forces have the stronger influence on  $N_2$ , about 22% for  $P^* = 0.436$ . It decreases below 15% for larger  $P^*$  values.

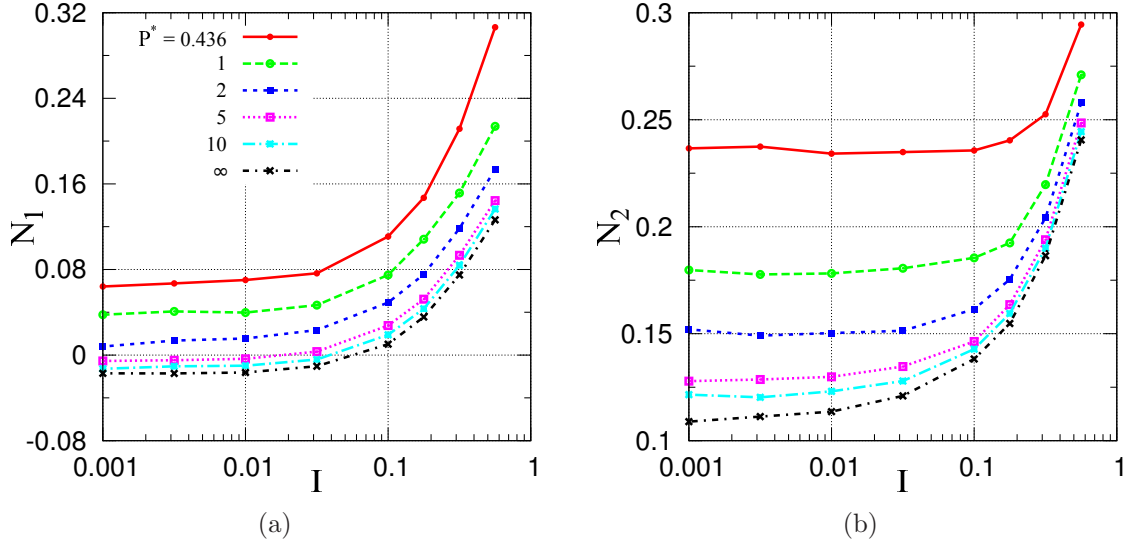


Figure 2.15: First (a) and second (b) normal stress differences as functions of  $I$  for different  $P^*$  values. The same symbols and colour codes apply to both figures.

### 2.2.6 Influence of capillary force model on macroscopic behaviour

We test here for the sensitivity of the macroscopic results to form and parameter choice for the capillary forces.

#### The Soulié formula for capillary forces

Most of our simulation results rely on the Maugis approximation for the calculations of the capillary forces. We assess the consequences of the inaccuracy of the Maugis approximation by replacing it with the Soulié formula. The latter is an accurate parametrization, carried out by Soulié *et al.* [141], of the capillary force between two smooth spheres, evaluated by numerical means (see Sec. 1.2.3). Fig. 2.16 plots the capillary forces, normalized by maximum cohesive force  $F_0$ , versus interparticle gap  $h$ , for the Maugis and Soulié models. Keeping the same values for the volume of menisci and the same rules for liquid bridge formation and rupture, we obtained the same results for the two different models, as represented in Fig. 2.17.

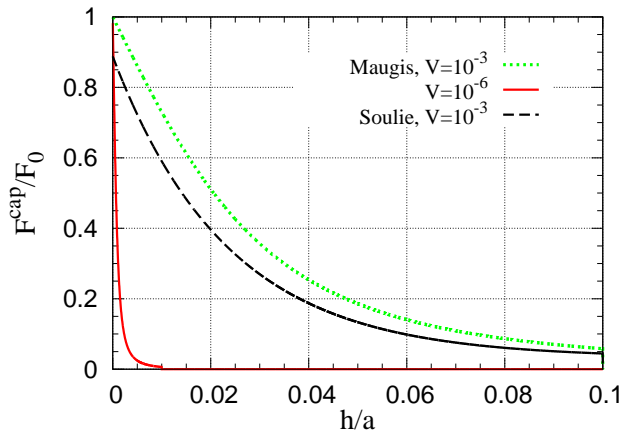


Figure 2.16: Force laws with Maugis model for two different volumes and with Soulié formula.

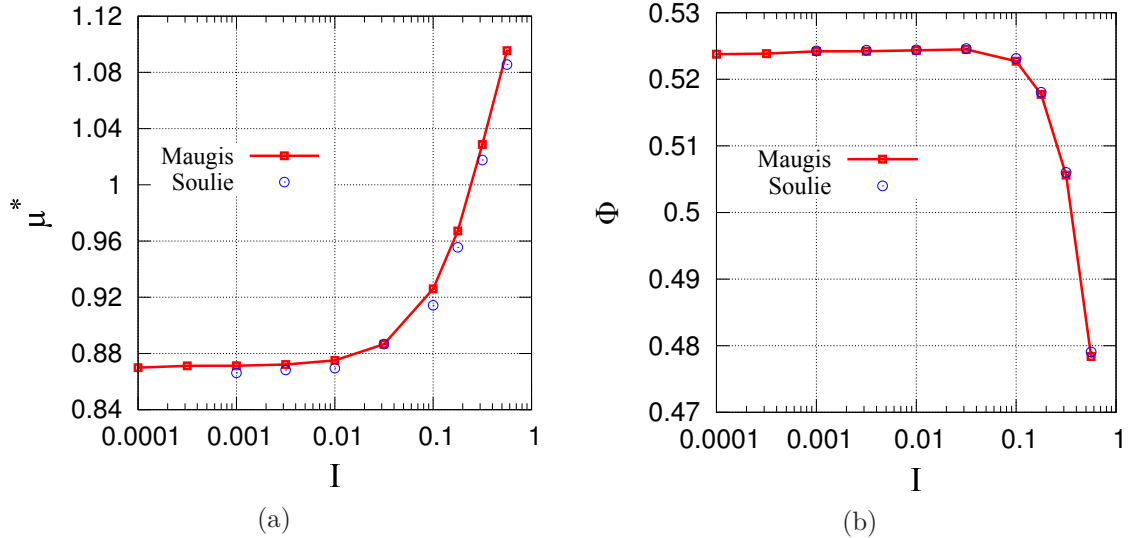


Figure 2.17: Macroscopic friction coefficient  $\mu^*$  (a) and solid fraction  $\Phi$  (b) versus inertial number  $I$  for the two different force models, Maugis and Souli , when the volume of menisci is  $V/a^3 = 10^{-3}$ .

### Influence of meniscus volume and force range

To understand the effect of the capillary attractions, it is instructive to assess the dependence of the system rheology on the meniscus volume and rupture distance. It is known from experimental studies that a liquid bridge of volume  $V$  will rupture at interparticle distance  $D_0 \approx V^{1/3}$  [151, 84]. Although it is in contrast with this experimental rule, we found it interesting to change the rupture distance while the volume of the meniscus is constant, in order to study the importance of the chosen model and the influence of the distant interactions on the rheology. Let us insist however that we used the experimental rule  $D_0 = V^{1/3}$  for the main series of results. Fig. 2.18 compares the values of the internal friction coefficient and of the solid fraction for different rupture distances when the meniscus volume is constant ( $V/a^3 = 10^{-3}$ ). Changing the force range significantly affects the macroscopic friction coefficient such that if we set the rupture distance to one tenth of its value in the standard model (Tab. 2.1),  $\mu^*$  decreases by about 10%. The  $\mu^*$  for the cohesive particles in the absence of distant interactions ( $D_0 = 0$ ) is more than 20% below the results of the standard model, but yet significantly larger than its value in cohesionless system ( $P^* = \infty$  in Fig. 2.11a). It shows that the cohesive forces and the distant interactions both have an important effect on the rheology of the granular material. It is interesting to note that although distant interactions contribute less than 10% of  $\sigma_{12}$  (Fig. 2.13a), removing them would have a much stronger influence on  $\mu^*$ . It informs us that the distant interaction also affects the microstructure. This issue will be discussed in Sec. 2.3 in detail.

Fig. 2.16 also shows the force law according to the Maugis approximation for different values of meniscus volume. Changing the volume affects the force curve and also the rupture distance given by  $D_0 = V^{1/3}$ . The effect of the meniscus volume on the microscopic behaviour is displayed in Fig. 2.19. Comparing the curves in Fig. 2.18 and Fig. 2.19 for the same values of  $D_0$ , reveals a significant effect of the volume change on the rheology. For a meniscus volume of  $10^{-6}a^3$ , compared to the standard case with  $V = 10^{-3}a^3$ ,  $\mu^*$  decreases by about 20%, and becomes similar to the result for  $D_0 = 0$  shown in Fig. 2.18a.

We therefore predict, in principle, a dependence of the wet granular material rheology on the saturation level. Of course, menisci as small as those chosen in the latter case ( $V/a^3 =$

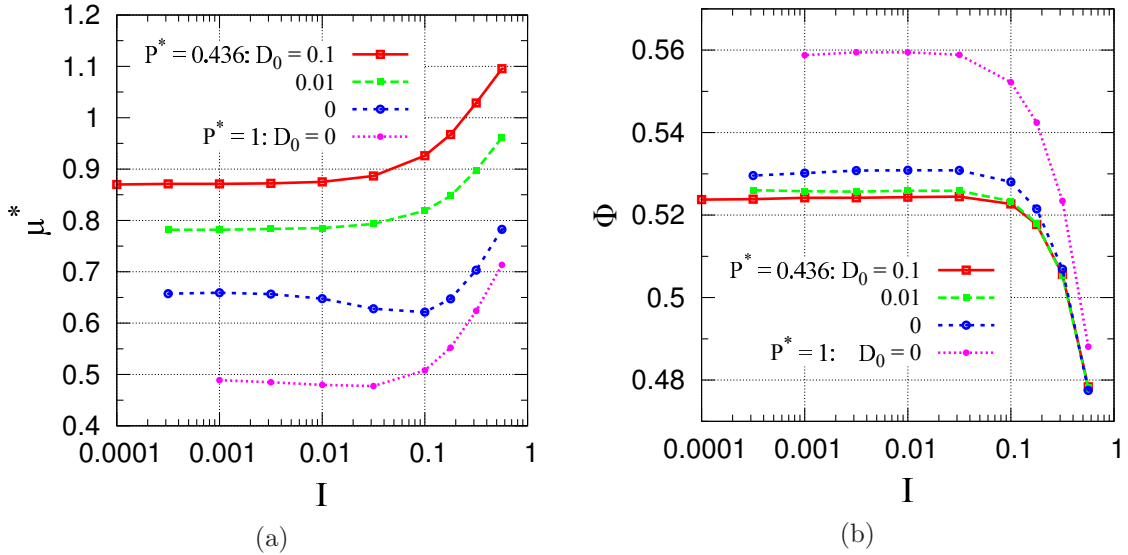


Figure 2.18: Macroscopic friction coefficient  $\mu^*$  (a) and solid fraction  $\Phi$  (b) versus inertial number  $I$  for different values of  $P^*$  and rupture distance  $D_0$ , with a constant meniscus volume  $V = 10^{-3}$ .

$10^{-6}$ ) are unlikely to exist in practice, because the saturation level would lie below the lower limit of the pendular state (see Sec. 2.1.1). Actually, in laboratory experiments, for such small amounts of water, the liquid bridges cannot form and the capillary effect is negligible [63]. To understand the effect of the saturation level within a valid range of the pendular state, we simulated two samples at upper and lower thresholds of the saturation in the pendular regime. As we discussed in Sec. 2.1.1, the valid saturation level in pendular regime approximately lies between  $1.5 \times 10^{-3}$  and 0.06. Since the saturation changes with solid fraction  $\Phi$  and coordination number  $z$ , we cannot accurately fix its value. The data in the first two columns of Tab. 2.4 show that choosing the meniscus volume between  $2 \times 10^{-4}a^3$  to  $10^{-2}a^3$  will completely cover the saturation range in the pendular state. The results for macroscopic parameters,  $\mu^*$  and  $\Phi$ , and coordination number  $z$  (see Sec. 2.3.1) for different saturation levels are presented in Tab. 2.4. A comparison of the results in the pendular state range shows that the solid fraction varies by less than 1%, while the macroscopic friction coefficient varies by about 20% in this range. We will argue in Sec. 2.3.1 that the variations of saturation level in our simulations are rather small, which results in a small change in the rheological properties.

$V/a^3$	$S_w$	$z$	$\Phi$	$\mu$
$10^{-2}$	$7.137 \times 10^{-2}$	6.863	0.520	1.071
$5 \times 10^{-3}$	$3.418 \times 10^{-2}$	6.556	0.522	1.003
$10^{-3}$	$6.305 \times 10^{-3}$	5.970	0.524	0.875
$2 \times 10^{-4}$	$1.075 \times 10^{-3}$	5.534	0.525	0.787
$10^{-6}$	$5.539 \times 10^{-6}$	4.836	0.530	0.661

Table 2.4: Effect of the meniscus volume or the saturation level on different parameters for  $I = 10^{-2}$  and  $P^* = 0.436$ .

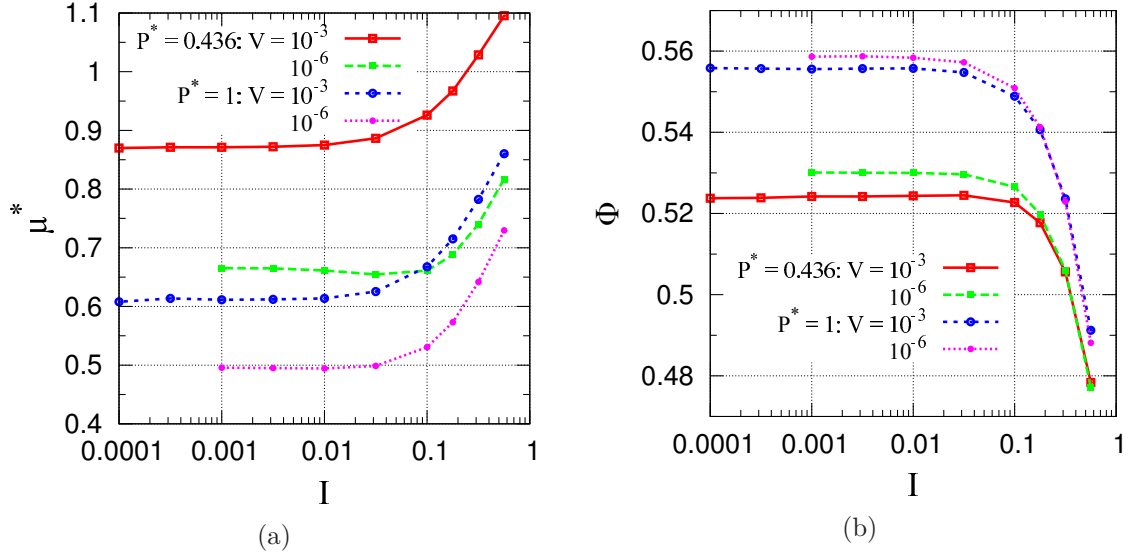


Figure 2.19: Macroscopic friction coefficient  $\mu^*$  (a) and solid fraction  $\Phi$  (b) versus inertial number  $I$  for different values of  $P^*$  and meniscus volume  $V$  (with  $D_0 = V^{1/3}$ ).

### Influence of capillary force hysteresis

As we explained in Sec. 1.2.3 the liquid bridges form in contact but break at distance  $D_0$ . We showed that reducing the interaction range might strongly change the mechanical properties. Here, we examine the influence of the hydraulic hysteresis by changing the rule: liquid bridges form and disappear at the same interparticle distance  $D_0$ .

Fig. 2.20 compares internal friction and solid fraction for different values of  $P^*$  and  $I$  with two different models: the standard model adopted in this chapter (formation of menisci at contact), and a model devoid of capillary force hysteresis, in which menisci appear as soon as non-contacting grains approach below distance  $D_0$ .

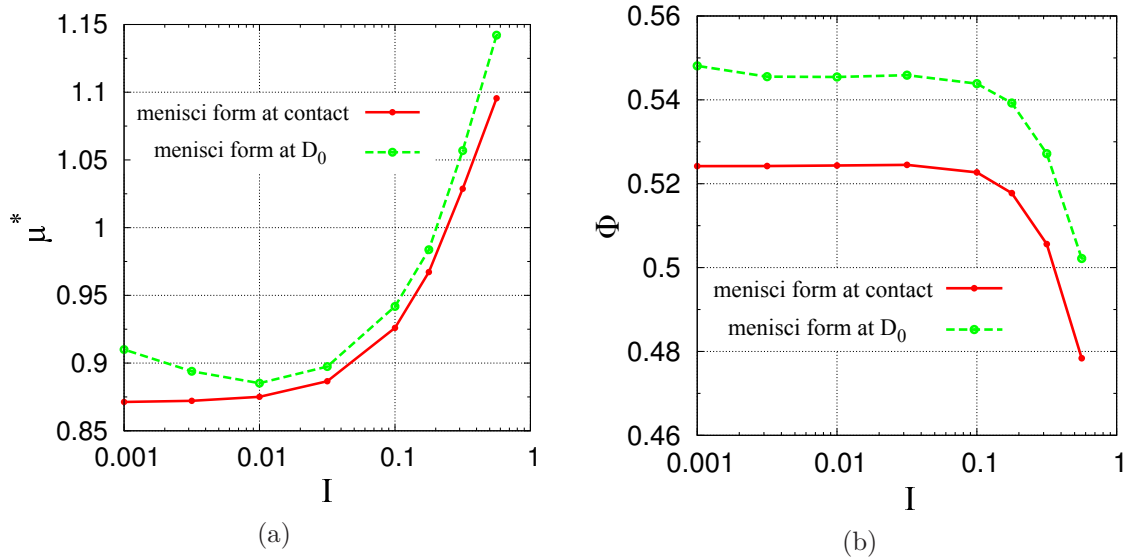


Figure 2.20: Macroscopic friction coefficient  $\mu^*$  (a) and solid fraction  $\Phi$  (b) versus inertial number  $I$  for  $P^* = 0.436$  and  $D_0 = 0.1$ , with and without capillary hysteresis.



With the new rule of meniscus formation,  $\Phi$  strongly increases, especially for small values of  $I$ . The internal friction  $\mu^*$ , for  $I \simeq 0.1$ , is close to the standard case, but larger values are obtained as  $I$  decreases. Even for the smallest values of  $I$  investigated ( $I = 0.001$ ), the material properties still depend on shear rate and no proper critical state appears to be approached in our simulations.

It should be mentioned that the strong influence of the hydraulic hysteresis on the behaviour of unsaturated granular soils is also reported in other studies [40]. It should be noted that the decreasing variation of  $\mu^*$  as a function of  $I$  in interval  $0.001 \leq I \leq 0.01$  should trigger instabilities, similar to those discussed in [133, 134], in a granular layer close to a smooth wall.

## 2.3 Microscopic analysis

In the first part of this thesis we studied the macroscopic properties of the wet granular material and we observed that the capillary forces have a strong influence on the rheological properties. The system can form loose and quite stable structures with a solid fraction quite smaller and a shear strength significantly larger than those of the cohesionless systems. We showed that such strong influence cannot be explained as an additive contribution to the stress components which may only introduce an extra isotropic pressure to the system. To find the physical origin of these phenomena, we need to study the microstructural changes due to capillary effect. In the following sections first we study the connectivity of the contact network and the contribution of contact and distant interactions to the coordination number. The force distribution and the influence of the capillary forces on the stability of the system is studied in Sec. 2.3.2. Then we measure the anisotropies in the orientations and force intensities, and the influence of control parameters on the anisotropy parameters. Finally, we show that the stronger capillary forces increase the durability of the contacts and lead to formation of large agglomeration of particles, which entails a more stable but looser structure.

### 2.3.1 Coordination number

#### Contact and distant coordination number

We define the coordination number  $z$  (Sec. 1.2.2) as a sum of two terms: the average number of contacts per grain,  $z_c$ , and the average number of liquid bridges joining a grain to non-contacting neighbours,  $z_d$ . Fig.2.21a shows that contact coordination number  $z_c$  decreases for a larger inertial number  $I$ , as previously observed in cohesionless [31, 104] systems and in cohesive ones [122]. For the smaller  $P^*$  values we see a slower decrease of  $z_c$  for larger  $I$  [122].  $z_c$  also increases as  $P^*$  decreases at constant  $I$ , as previously observed as well [122]. Note that this latter trend is opposite to that of the solid fraction (Fig. 2.12b). As the importance of adhesion relative to confinement stresses increases, looser systems are obtained, yet better coordinated. Grains tend to stick to one another, and may form loose aggregates, as in static or quasistatically compressed assemblies, for which little correlation is also observed [54, 55] between density and coordination number.

An approach to critical state for small values of  $I$  is observed, similar to those observed for macroscopic quantities (Sec. 2.2.3) and here again approaching the quasistatic limit is faster for smaller values of  $P^*$ . The curves for  $P^* = 0.436$  and  $P^* = 1$  in Fig. 2.21a show that the quasistatic limit is nearly reached for  $I = 10^{-2}$  while for  $P^* = 10$  or  $\infty$  we need to shear the system at a slower rate with  $I$  below  $10^{-3}$ .

Distant coordination number  $z_d$  varies in the opposite direction of  $z_c$  and increases with  $I$  and  $P^*$  (Fig. 2.21b). When  $I$  increases, so does  $z_d$ , as contacting pairs tend to open, but some

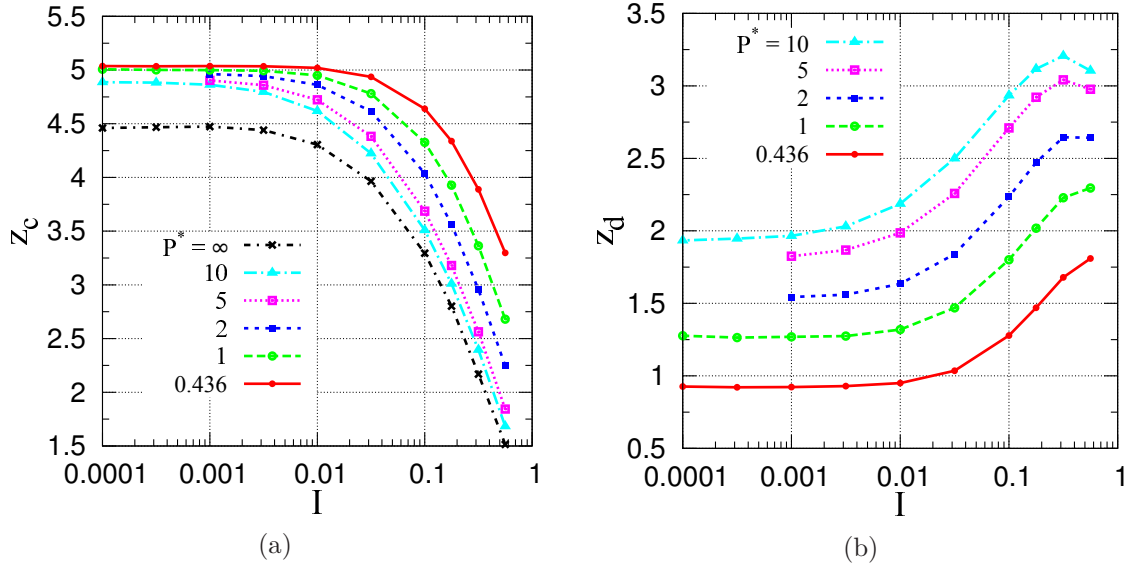


Figure 2.21: Coordination number for contacting pairs (a) and distant interactions (b).

remain bonded by liquid bridges. For stronger cohesion (smaller  $P^*$  values),  $z_d$  is correlated with the system density as observed in static packing for the number of neighbours at distance  $\leq 0.1a$  [1]. As solid fraction decreases for the smaller values of  $P^*$ ,  $z_d$  also decreases. Strictly speaking,  $z_d$  decreases for stronger capillary forces first because the particles attract their neighbours stronger and some of the distant interacting pairs come into contact. Also, in the tighter space around a particle the number of the close neighbours decreases. The variations of coordination numbers with  $P^*$  are better visualized in Fig. 2.22a. The distribution of the number of particles with  $N_c$  contact is available by Fig. 2.22b. The results for different  $P^*$  values are very similar, close to an experimental result for packed grains with density  $\Phi = 0.57$  [50]. The fraction of *rattlers* (beads carrying no force [104]) for non-cohesive system of grains is about 5%. In the cohesive case, due to the attractive forces, nearly all of the particles are captured by the force-carrying structure and the number of rattlers tends to zero. This effect is also observed in the simulation of 2D cohesive powders [54, 55].

### Total coordination number and saturation

Fig. 2.23 displays total coordination number  $z$  (or liquid bridge coordination number) as a function of  $I$  for different values of  $P^*$ . Our results in the quasistatic limit are comparable to the experimental results by Kohonen *et al.* [74, 50] for random packing of spheres. They obtained  $z \approx 6$  for their loose packing ( $\Phi = 0.57$ ) and  $z \approx 6.5$  for their dense packing ( $\Phi = 0.62$ ). Due to the opposite variation of  $z_d$  and  $z_c$ , the sum  $z = z_c + z_d$  exhibits rather smaller changes. The maximum variation of  $z$ , within the investigated range of  $I$  and  $P^*$  values, belongs to the cohesive system with  $P^* = 10$  (see Fig. 2.23). It decreases from 6.8 in the quasistatic limit down to 4.8 for  $I = 0.562$ , which entails a decrease in saturation  $S_w$  (Eq. 2.2) from  $8 \times 10^{-3}$  to  $4 \times 10^{-3}$ . As we discussed in Sec. 2.2.6, the variations of the saturation within the pendular regime do not affect the rheological behaviour of the system significantly. Comparing the results for  $S_w = 1.075 \times 10^{-3}$ , in Tab. 2.4, to the standard case with  $S_w = 6.305 \times 10^{-3}$ , shows that the solid fraction just exhibits a tiny change and the friction coefficient only varies about 10%. Consequently, the influence of saturation on our results is below 5%.

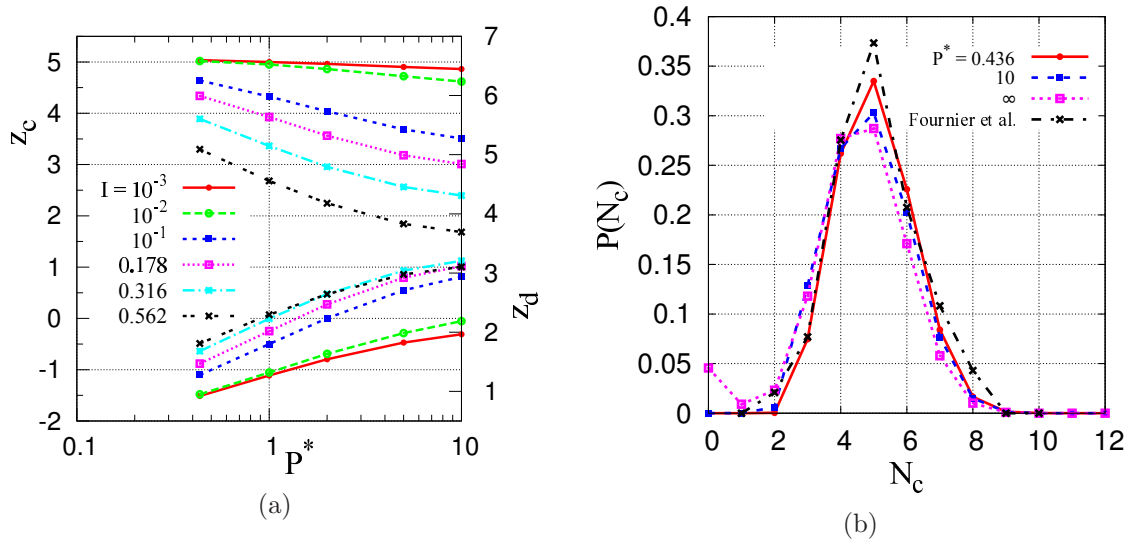


Figure 2.22: (a) Contact and distant Coordination numbers versus  $P^*$  for different values of  $I$ . (b) Distribution of the number of contacts per grain for different  $P^*$  values and  $I = 10^{-3}$ , compared to an experimental result [50].

### Coordination number of tensile and compressive bonds

An alternative decomposition of the coordination number is:

$$z = z^+ + z^-,$$

in which  $z^+$  is the coordination number of compressive bonds (positive forces) and  $z^-$  is the coordination number of tensile bonds (negative forces). Note that  $z^+$  includes only the contacts in which the repulsive elastic force is larger than the capillary force, and  $z^-$  includes all the distant interacting pairs and also all the contacts in which the capillary force dominates.

Richefeu *et al.* studied the random packing of a wet granular material under zero confining pressure [119], when the network of self-equilibrated bond forces involves the tensile and the compressive force chains. Under zero confining pressure they obtained  $z = 6.1$  in which the respective contributions of compressive and tensile bonds are  $z^+ = 2.97$  and  $z^- = 3.13$ . They showed that after the application of a confining pressure (with  $0.5 \lesssim P^* \lesssim 1$  with their choice of parameters) a fraction of tensile bonds transform into compressive bonds and the contribution of tensile bonds to  $z$  decreases (with  $z^+ = 4.85$  and  $z^- = 0.85$  when  $z = 5.7$ ).

We also measured  $z^+$  and  $z^-$  and we observed that in shear flow, the tensile and compressive bonds contribute almost equally to the total coordination number. Tab. 2.5 displays the variations of  $z^+$ ,  $z^-$  and the distant coordination number,  $z_d$ , with  $P^*$ , for two different values of  $I$ . For the smaller values of  $P^*$ , in the quasistatic limit, despite the decrease of  $z_d$ ,  $z^+$  decreases and  $z^-$  increases. It should be noted that  $z_c$  does not vary significantly with  $P^*$  in the quasistatic limit (Fig. 2.22a). Increasing  $P^*$  would increase the number of contacts with an attractive force ( $z^- - z_d$ ). For faster flows, the number of contacts, and consequently  $z^+$ , increases for smaller  $P^*$ , while  $z_d$  and  $z^-$  significantly decrease.

### Coordination number of close neighbours

It is interesting to compare the number of distant interacting pairs to the total number of neighbour pairs at distance below  $D_0$ . The coordination number  $z(h)$  of the neighbour grains at distance below  $h$  (such that  $z(0) = z_c$ ) grows with  $h$  as depicted in Fig. 2.24, corresponding

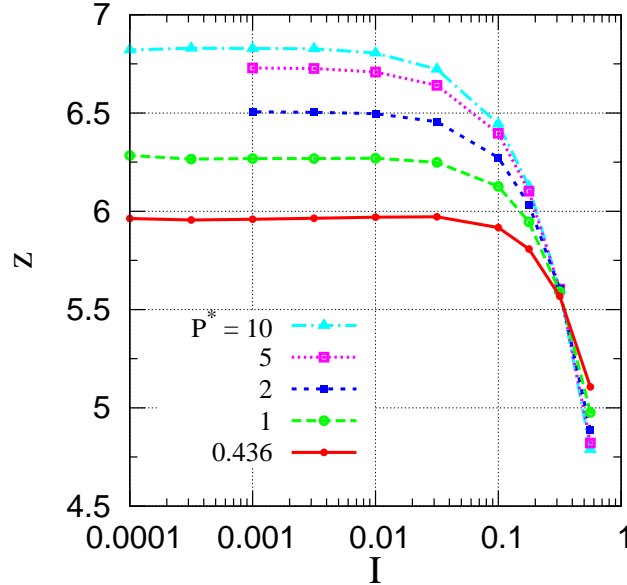


Figure 2.23: Coordination number of all interactions as a function of  $I$  for different  $P^*$  values.

$P^*$	$I = 10^{-3}$			$I = 10^{-1}$		
	$z^+$	$z^-$	$z_d$	$z^+$	$z^-$	$z_d$
0.436	3.381	2.579	0.924	3.133	2.785	1.278
1	3.797	2.471	1.269	3.242	2.885	1.801
2	4.105	2.401	1.544	3.227	3.046	2.235
5	4.400	2.328	1.825	3.140	3.257	2.710
10	4.520	2.308	1.965	3.084	3.359	2.934

Table 2.5: Coordination number of compressive  $z^+$  and tensile  $z^-$  bonds and also distant coordination number  $z_d$  versus  $P^*$  for two different values of  $I$ .

to  $I = 10^{-3}$  (quasistatic limit).  $z(h)$ , like the contact coordination number, is a decreasing function of  $P^*$  for small  $h/a$  (below about  $2.5 \times 10^{-3}$ , see the inset in Fig. 2.24). It increases with  $P^*$ , like the solid fraction, beyond that distance. In the denser systems the grains have more neighbours on average, but this is only true if neighbours at some distance are included in the count, and does not apply to the contacts (a situation reminiscent of some observations in static packings of cohesionless grains [1]). Up to meniscus rupture distance  $D_0$ , equal to  $0.1a$  in the present case, each grain has on average  $z(D_0) - z_c$  non-contacting neighbours, among which  $z_d$  neighbours are interacting by an attractive capillary force. The ratio  $z_d/(z(D_0) - z_c)$  for different values of  $P^*$  and two different  $I$  values are given in Tab. 2.6. The proportion of the neighbours within the range  $D_0$  bonded by a liquid bridge varies between 0.61 to 0.71 for  $I = 10^{-3}$  and between 0.68 to 0.79 for  $I = 10^{-1}$ . These values are similar to the proportion of about 50% reported by Kohonen *et al.* [74].

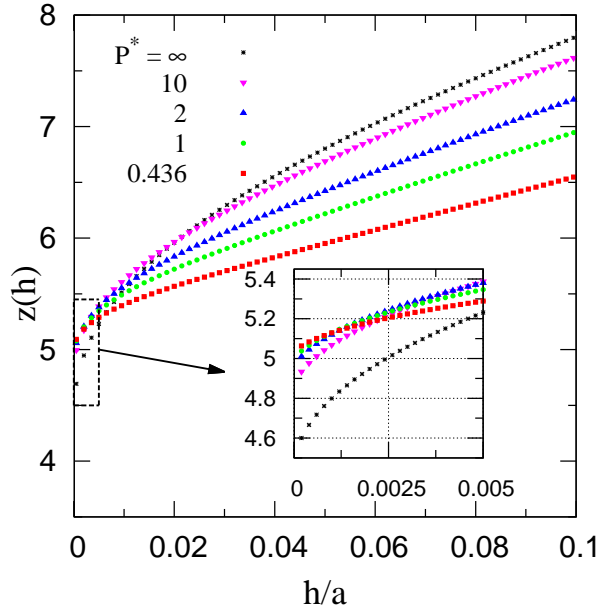


Figure 2.24: Coordination number of neighbour grains versus dimensionless interparticle distance  $h/a$ , for different values of  $P^*$  for  $I = 10^{-3}$ . The inset shows the same plot over a smaller range.

$P^*$	$I = 10^{-3}$		$I = 10^{-1}$	
	$z_d$	$z_d/(z(D_0) - z_c)$	$z_d$	$z_d/(z(D_0) - z_c)$
0.43	0.9228	0.60854	1.2782	0.68076
1	1.2691	0.64957	1.8007	0.72312
2	1.5437	0.67483	2.2353	0.75088
5	1.8251	0.70103	2.7102	0.77634
10	1.9652	0.71193	2.9341	0.78694

Table 2.6: Distant coordination number  $z_d$  and the probability of meniscus formation between close neighbours defined as  $z_d/(z(D_0) - z_c)$ , versus  $P^*$  for two different values of  $I$ .

### 2.3.2 Normal interactions

#### Pressure and average normal force

As we described in Sec. 1.2.2, there is a relation between the average pressure  $\mathcal{P}$  and average normal force  $\langle F^N \rangle$  (see Eq. 1.18). Now, we derive a similar relation including distant interactions. The internal pressure is proportional to the trace of stress tensor ( $\mathcal{P} = \frac{1}{3} \text{tr} \underline{\underline{\sigma}}$ ). Thus, by using Eq. 1.15 we obtain:

$$\mathcal{P} = \frac{1}{3\Omega} \sum_{i < j} F_{ij}^N \|\mathbf{r}_{ij}\|, \quad (2.17)$$

in which  $\|\mathbf{r}_{ij}\|$  is the center to center distance between interacting particles. For distant interactions we write it as  $a + h_{ij}$  ( $a$  is the particle diameter,  $h_{ij}$  is the interparticle gap) and for contacts it is approximately equal to  $a$ . We can split this equation for contacts and

distant interactions as:

$$\begin{aligned}
 \mathcal{P} &= \frac{1}{3\Omega} \sum_{i<j} F_{ij}^{N,c} a + \frac{1}{3\Omega} \sum_{i<j} F_{ij}^{N,d} (a + h_{ij}) \\
 &= \frac{1}{3\Omega} \sum_{i<j} F_{ij}^{N,c} a + \frac{1}{3\Omega} \sum_{i<j} F_{ij}^{N,d} h_{ij}
 \end{aligned}
 \tag{2.18}$$

Replacing the sums with the average values and using the definitions of  $\Phi$ ,  $z$  and  $z_d$  gives us:

$$\mathcal{P} = \frac{\Phi z}{\pi a^2} \langle F^N \rangle + \frac{\Phi z_d}{\pi a^3} \langle F^{N,d} h \rangle
 \tag{2.19}$$

Tab. 2.7 checks that Eq. 2.19 is nearly exact and shows that the second term in Eq. 2.19 is very small of the order of  $10^{-3}$ .

$P^*$	$\mathcal{P}$	$z$	$z_d$	$\Phi$	$\langle F^N \rangle$	$\langle F^N h \rangle$	$\mathcal{P}$
0.436	0.943	5.960	0.923	0.524	0.949	-0.015	0.944
1	0.953	6.269	1.269	0.556	0.862	-0.007	0.956
2	0.952	6.506	1.544	0.572	0.806	-0.003	0.956
5	0.956	6.729	1.825	0.585	0.764	-0.001	0.957
10	0.955	6.829	1.965	0.590	0.745	-0.000	0.955

Table 2.7: Internal pressure  $\mathcal{P}$  versus  $P^*$ , obtained from the direct measurement (second column) and calculated from Eq. 2.19 and other parameters in this table (last column), for  $I = 10^{-3}$ .

### Probability distribution function of normal forces

The probability distribution function (pdf) of normal forces (normalized by maximum tensile force  $F_0$ ) for  $P^* = 0.436$  and different values of  $I$  is shown in Fig. 2.25a. The distribution of compressive (positive) forces is similar to the results obtained in other numerical studies on cohesionless [104, 1, 38, 139, 101, 110] or cohesive [119, 118] granular materials. We see an approximately exponential decay of  $P(F^N/F_0)$  for larger values of  $F^N/F_0$  with a peak close to  $F^N = 0$ . The slope of the decay increases as we approach the quasistatic limit [104]. The contribution of contacts and distant interactions to pdf are separately plotted in Fig. 2.25b, in which the distribution of the total interactions, indicated by black circles, is the sum of the two other terms. The contribution of contacts decreases for the stronger tensile or compressive forces, while the contribution of distant interaction sharply increases near  $-F_0$  and near another slightly negative value, which coincides with  $F(D_0)$ , the attractive force at meniscus rupture distance. To describe these behaviours we plotted the distribution of interparticle distances (or normal deflection of the contacts),  $P(h/a)$ , for all interacting pairs in Fig. 2.26a.

The inset in Fig. 2.26a shows  $P(h/a)$  for contacts ( $h/a \leq 0$ ) in a shorter range of  $h/a$ . The vertical dashed line, which nearly coincides with the peak of  $P(h/a)$ , indicates the interparticle distance for which the normal elastic force and the capillary force compensate. The normal force is compressive for smaller gaps and tensile for larger ones. The decrease of  $P(h/a)$  in both directions explains the decrease of the contribution of contacts to  $P(F^N/F_0)$  for the stronger compressive or tensile forces (Fig. 2.25b). The decrease of  $P(h/a)$  for larger interparticle distances (with  $h/a > 0$ ), in Fig. 2.26a, also shows that the distant interacting pairs are more frequent with smaller gaps or with a capillary force near the maximum cohesion  $F_0$ . That is why the contribution of distant interactions to  $P(F^N/F_0)$  increases near

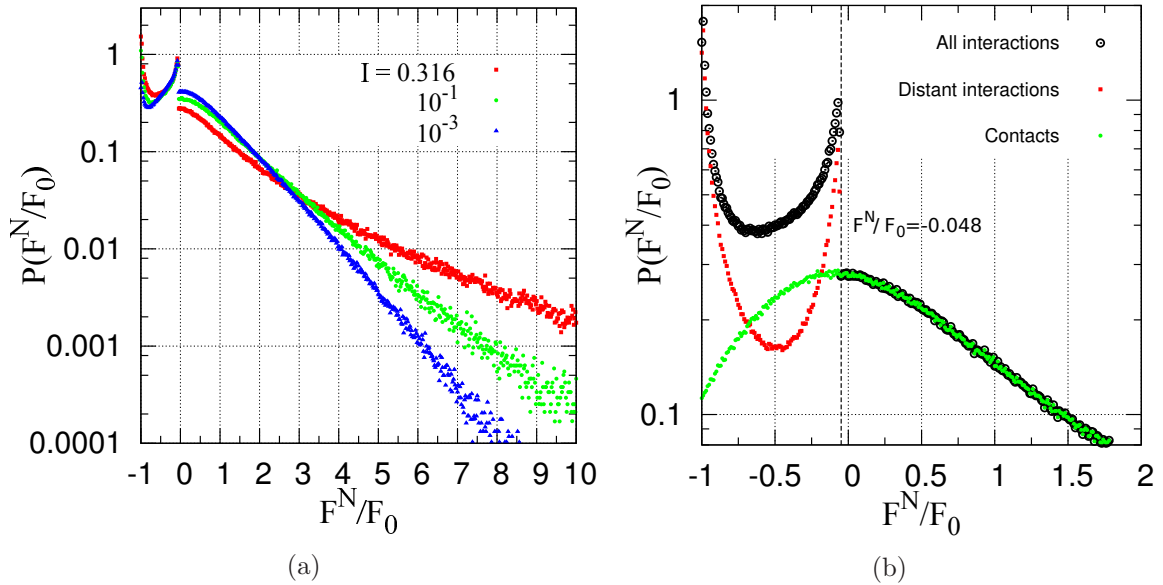


Figure 2.25: (a) Distributions of the normal forces for  $P^* = 0.436$  and different values of  $I$  normalized by the maximum cohesive force  $F_0$ . (b) Contribution of the contacts and the distant interactions to the normal force distribution for  $P^* = 0.436$  and  $I = 0.316$ . Note that just the distribution for all interactions is normalized. The vertical dashed line shows the normal force at rupture distance  $D_0 = 0.1$ .

$F^N = -F_0$  (Fig. 2.25b). The rate of the variations in  $P(h/a)$  rapidly decreases and it tends to a plateau for larger  $h/a$ . Since for the larger  $h$  the variation of capillary forces is small (Fig. 2.16), the probability of finding pairs with the same value of  $F^N/F_0$  increases. This explains the increase of the contribution of the distant interaction to  $P(F^N/F_0)$  for larger values of  $F^N/F_0$  in Fig. 2.25b, until the pdf drops off for the small negative value corresponding to  $D_0 = 0.1$ .

The influence of  $P^*$  on normal force distribution is shown in Fig. 2.26b. Since the variation of the average normal force for different values of  $P^*$  (Tab. 2.7) is very small compared to the large range of  $F_0$  used in our simulations (from 0.1 to 2.293), we normalized the pdf by  $\langle F^N \rangle$ . The decrease of the slope of the pdf for smaller values of  $P^*$  shows that the stronger capillary forces reinforces the contact network and so it can support stronger repulsive interactions. This effect is also reported by other numerical studies [118].

### 2.3.3 Anisotropy

In Sec. 2.2 we studied the influence of  $P^*$  and  $I$  on the rheology and we measured the contributions of different forces to the stresses, from a macroscopic point of view. We also investigated the different microscopic features of the material in previous sections. But to have a comprehensive knowledge about the microscopic origin of the rheological behaviour, we also need to examine the organization of the interacting pairs and possible favoured direction in the orientation of pairs and strong forces. Several recent studies show that the shear strength of granular materials can generally be attributed to the formation of an anisotropic structure induced by mechanical loading [111, 9, 8] (see Sec. 1.2.2). Herein, we make a detailed inquiry on the anisotropy of the pair orientations (structural anisotropy) and on the anisotropy of the angular distribution of force intensities (mechanical anisotropy). We also relate stresses to the microscopic parameters. We use these relations to describe the influence of anisotropy



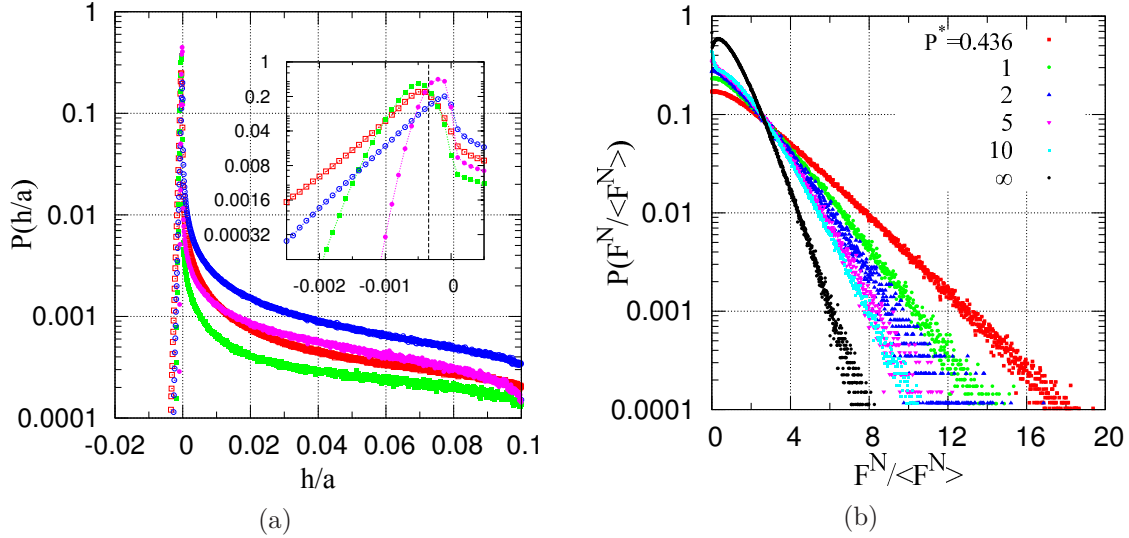


Figure 2.26: (a) Distributions of normal interparticle distances normalized by particle diameter  $a$  for  $P^* = 0.436$  with  $I = 0.316$  (red empty squares) and  $I = 10^{-3}$  (green filled squares) and also for  $P^* = 10$  with  $I = 0.316$  (blue empty circles) and  $I = 10^{-3}$  (magenta filled circles). Inset is the same figure for a shorter range of  $h/a$ . Vertical dashed line indicates  $h/a = -3.420 \times 10^{-4}$  for which the normal elastic force balances the capillary force. (b) Distributions of normal forces normalized by average normal force  $\langle F^N \rangle$  for  $I = 10^{-3}$  and different values of  $P^*$ .

parameters on the contribution of normal forces to stress components,  $\sigma_{\alpha\beta}^N$ , which represents more than 80% of the total  $\sigma_{\alpha\beta}$  (see Fig. 2.14a).

### Stress-anisotropy relation

We can replace the sum in Eq. 1.15 with the average of the tensor product of normal force vector  $\mathbf{F}^N$  and branch vector  $\mathbf{r}$ . So, for a system of  $N$  particles, including  $Nz/2$  interacting pairs we have:

$$\underline{\underline{\sigma}}^N = \frac{Nz}{2\Omega} \langle \mathbf{F}^N \otimes \mathbf{r} \rangle \quad (2.20)$$

We split this equation into two terms, the contribution of contacts  $\underline{\underline{\sigma}}^{N,c}$ , and the contribution of distant interactions  $\underline{\underline{\sigma}}^{N,d}$ . Since the system under consideration is close to the rigid limit ( $\kappa \gg 1$ ), small deformations at contacts are negligible. So for all pairs in contact we can write  $\mathbf{r} = a\mathbf{n}$ , with  $a$  the particle diameter and  $\mathbf{n}$  the unit vector in the direction of  $\mathbf{r}$ . Then we get:

$$\underline{\underline{\sigma}}^N = \frac{Nz_c a}{2\Omega} \langle \mathbf{F}^{N,c} \otimes \mathbf{n} \rangle + \frac{Nz_d}{2\Omega} \langle \mathbf{F}^{N,d} \otimes \mathbf{r} \rangle \quad (2.21)$$

Mathematically, material anisotropy can be characterized by the joint probability density function  $P(\mathbf{n}, \mathbf{F})$  defined as the probability of finding an interacting pair of particles oriented along the unit vector  $\mathbf{n}$  and carrying a force of intensity  $F$ . By using this function, the first term in the right hand side of the above equation could be replaced by

$$\underline{\underline{\sigma}}^{N,c} = \frac{Nz_c a}{2\Omega} \int d\Omega dF^{N,c} P(\mathbf{n}, \mathbf{F}^{N,c}) \mathbf{n} \otimes \mathbf{n}. \quad (2.22)$$

Defining  $\langle F^{N,c} \rangle_{\mathbf{n}}$  as the density of normal contact forces along the unit vector  $\mathbf{n}$  and  $E(\mathbf{n})$  as

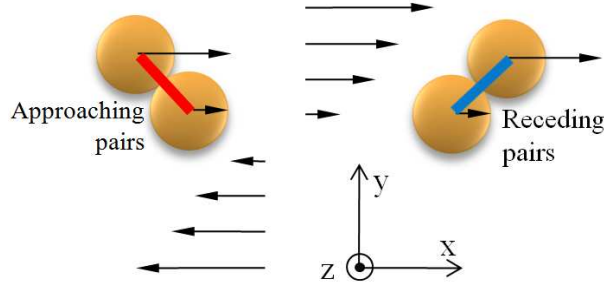


Figure 2.27: An sketch of approaching ( $\varphi$  near  $3\pi/4$ ) and receding pairs ( $\varphi$  near  $\pi/4$ ) in shear flow.

the probability of finding a contact along  $\mathbf{n}$ , we get:

$$\underline{\underline{\sigma}}^{\text{N,c}} = \frac{Nz_c a}{2\Omega} \int d\Omega E(\mathbf{n}) \langle \mathbf{F}^{\text{N,c}} \rangle_{\mathbf{n}} \mathbf{n} \otimes \mathbf{n}, \quad (2.23)$$

in which  $E(\mathbf{n})$  describes the structural anisotropy and  $\langle \mathbf{F}^{\text{N,c}} \rangle_{\mathbf{n}}$  describes the mechanical anisotropy in the system.

From a similar procedure, the second term in the right hand side of Eq.2.21, representing  $\underline{\underline{\sigma}}^{\text{N,d}}$ , could be written as an integral over the anisotropy functions. Note that for the distant interacting pairs, the center to center distances are not constant and we need also to consider the anisotropy of the angular distribution of these distances, characterized by  $\mathcal{L}(\mathbf{n})$  (see sec. A.1.5). The result will be:

$$\underline{\underline{\sigma}}^{\text{N,d}} = \frac{Nz_d a}{2\Omega} \int d\Omega E(\mathbf{n}) \langle \mathbf{F}^{\text{N,d}} \rangle_{\mathbf{n}} \mathcal{L}(\mathbf{n}) \mathbf{n} \otimes \mathbf{n} \quad (2.24)$$

### Structural anisotropy

$E(\mathbf{n})$  is defined on the unit sphere in  $\mathbb{R}^3$  and can thus be expanded in series of spherical harmonics. Eq. A.7 shows the result of such an expansion in which the coefficients are the components of the second-order fabric tensor  $\underline{\underline{\mathbf{F}}}$ , defined by Eq. 1.19. To have an idea about the fabric parameters, let us consider component  $F_{12}$  of fabric tensor and Fig. 2.27. This figure represents two different orientations of pairs according to angle  $\varphi$  from the direction of the flow  $x_1$ , in the  $x_1x_2$  plane. Pairs with  $0 < \varphi < \pi/2$  are labeled *receding pairs* and pairs with  $\pi/2 < \varphi < \pi$  are labeled *approaching pairs*, according to their normal relative motion in the average shear flow (Fig. 2.27). Generally, a positive value of  $F_{12}$  shows that the pairs tend to be more often oriented in the direction of receding pairs and a negative value of  $F_{12}$  shows that the approaching pairs are dominant.

Fig. 2.28 shows the variations of different components of fabric tensor as functions of inertial number  $I$  for  $P^* = 0.436$ . The contribution of contacts and of distant interacting pairs are shown in two separate graphs. In both cases  $F_{13}$  and  $F_{23}$  are negligible. Compared to  $F_{12}$ , terms  $(F_{33} - 1/3)$  and  $(F_{11} - F_{22})$  are also small. Those latter will be discussed more in Sec. 2.2.5, but here we focus on the contributions of contact and distant interactions to  $F_{12}$  which exhibit the largest variations in both graphs.

The negative sign of  $F_{12}^c$  shows that the contacts are mostly oriented in the direction of the approaching pairs. Therefore, they reinforce the shear strength and as the value of  $|F_{12}^c|$  increases,  $\mu^*$  also increases (see Fig. 2.11a). The positive sign of  $F_{12}^d$  in Fig. 2.28b shows that the distant interacting pairs are mostly oriented in the direction of the receding pairs. Noting that these pairs interact with an attractive force and considering their favorite orientation, they also enhance the shear strength. This explains the positive contribution of

distant interactions to shear stress in Fig. 2.13a. The variation of  $F_{12}^d$  for larger values of  $I$  is in the opposite direction to  $F_{12}^c$  and  $\mu^*$ . The relatively large values of  $F_{12}^d$  compared to  $F_{12}^c$  are due to the hysteretic nature of the liquid bridges (see Sec. 1.2.3).

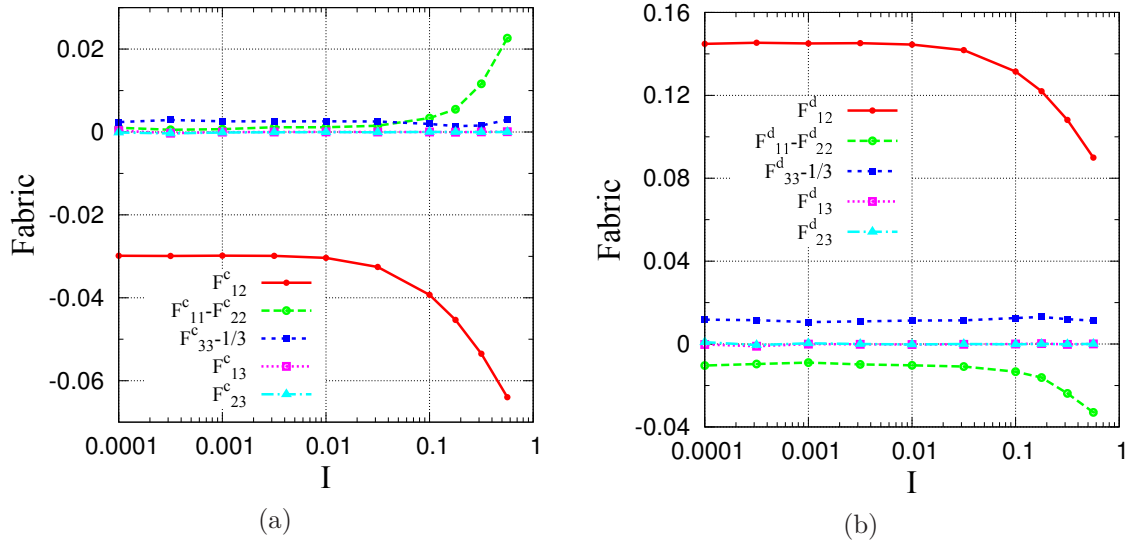


Figure 2.28: Fabric parameters for contacts (a) and distant interactions (b) versus  $I$  for  $P^* = 0.436$ .

The evolutions of fabric parameters  $F_{12}^c$  and  $F_{12}^d$  versus  $I$ , for different  $P^*$  values, are displayed in Fig. 2.29. The decrease of  $F_{12}^c$  as  $I$  increases is also observed in Reference [104], in which the shear flow of frictionless dry grains is studied and the value  $F_{12}^c \simeq -0.02$  is obtained in the quasistatic limit. In our case, in the dry system ( $P^* = \infty$ ),  $F_{12}^c$  undergoes the largest variations within the applied range of  $I$ . Our results reveal that in the presence of friction, the anisotropy in the contact orientations increases. As we decrease the value of  $P^*$ , the variation of  $F_{12}^c$  with  $I$  also decreases. Strictly speaking, it is more difficult to impose a certain orientation to the pairs that are strongly connected with random orientations within the clusters. The evolutions of  $F_{12}^c$  and  $F_{12}^d$  with  $P^*$  are better visualized in Fig. 2.30. For smaller  $P^*$  values, the anisotropy of the contacts decreases and the anisotropy of the distant interactions increases, in accordance with the increase of the contribution of the distant interactions to the shear stress, for smaller values of  $P^*$  (Fig. 2.13a).

The decrease of the anisotropy of the contact orientations could be explained as follows. Considering the relative motion of a pair of grains in the shear flow, as depicted in Fig. 2.27, it is reasonable to expect the separation of contacting pairs to occur for  $0 < \varphi < \pi/2$ . As the capillary force opposes the receding motion, the separation angle increases for smaller values of  $P^*$ . As a consequence, the anisotropy of contacts decreases. On the other hand, as we mentioned in Sec. 2.3.1, the opposite variations of the contact coordination number and the solid fraction indicate the agglomeration of particles. Shear flow carries these agglomerates for some distance before they break and in their random tumbling motion also tends to increase the isotropy of the contact orientations.

Using the values of the fabric parameters and the coordination number of contacts and distant interactions, the fabric parameters for total interactions (or liquid bridges) could be calculated as below:

$$F_{\alpha\beta} = \frac{F_{\alpha\beta}^c z_c + F_{\alpha\beta}^d z_d}{z_c + z_d}$$

We can use this equation to calculate  $F_{12}$ , which results in a negative value for all values of  $P^*$  and  $I$ . So, the total interactions (and also the contacts) are mostly oriented in the

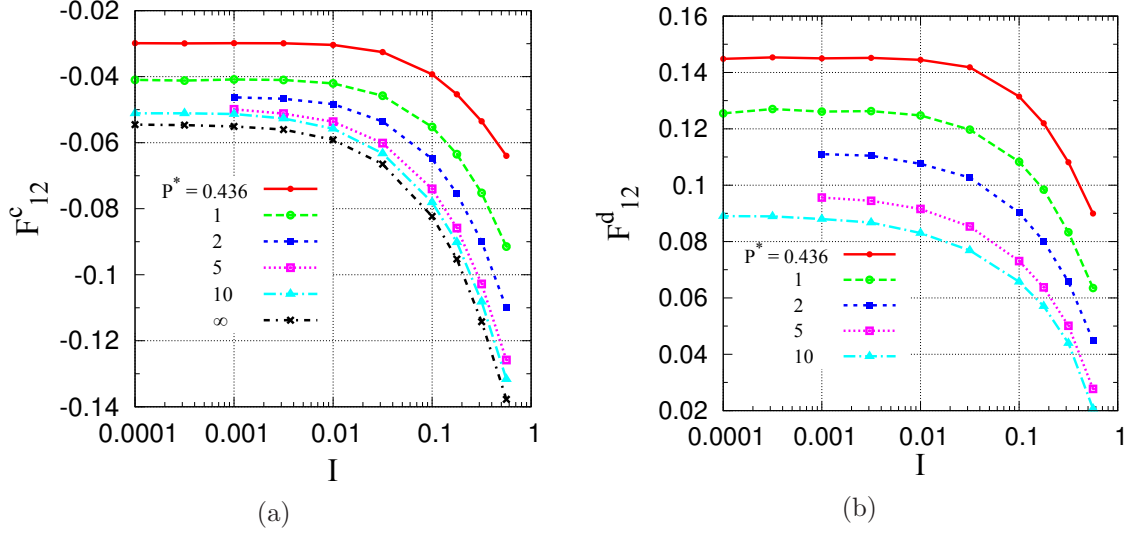


Figure 2.29: Fabric parameter  $F_{12}$  for contacting pairs (a) and distant interactions (b) versus  $I$  for different  $P^*$ .

direction of approaching pairs. Considering that the contacts carry strongest capillary force, we can say: the attractive capillary forces with the largest population and strongest force in the direction of approaching pairs, reduce the shear stress  $\sigma_{12}$ , as displayed in Fig. 2.14b.

### Mechanical anisotropy

The mechanical anisotropy is described with  $\langle F^N \rangle_{\mathbf{n}}$  or equivalently with its dimensionless form  $\mathcal{F}(\mathbf{n})$  which is normalized by average normal force  $\langle F^N \rangle$ . Similar to  $E(\mathbf{n})$ , the angular distribution of force intensity,  $\mathcal{F}(\mathbf{n})$ , can be expanded in series of spherical harmonics. The result of the expansion is shown in Eq. A.8 in which  $\mathcal{F}_{\alpha\beta}$  components are defined in analogy to the fabric parameters and can be calculated using Eq. A.3. Here again the contribution of contacts and distant interactions are separately calculated. For both contributions  $\mathcal{F}_{13}$  and  $\mathcal{F}_{23}$  are negligible. The other terms in Eq. A.8, for the distant interactions, are also small of the order of  $10^{-2}$ . For small values of  $P^*$  and  $I$ ,  $\mathcal{F}_{12}^d$  is about -0.03, which decreases down to -0.05 for larger values of  $P^*$  and  $I$ . It shows that the anisotropy in the intensity of the distant forces induce shear softening in the system, however this influence is very small. The values of  $(\mathcal{F}_{33}^c - 1/3)$  and  $(\mathcal{F}_{11}^c - \mathcal{F}_{22}^c)$  are also small (the latter will be discussed in Sec. 2.2.5).  $(\mathcal{F}_{33}^c - 1/3)$  is displayed in Fig. 2.31a for the different values of  $P^*$  and  $I$ , in which it increases with  $P^*$  from -0.03 to -0.01, nearly the same for different values of  $I$ .  $\mathcal{F}_{12}^c$  shows the largest anisotropy and variation compared to the other terms (Fig. 2.31b). The negative sign of  $\mathcal{F}_{12}^c$  shows that statistically the strongest contact forces tend to be oriented in the direction of approaching pairs. Consequently, the anisotropy in the angular distribution of force intensity leads to the increase of shear strength. This anisotropy increases for smaller values of  $P^*$  and does not vary significantly with  $I$ .

In addition to distribution functions  $E(\mathbf{n})$  and  $\mathcal{F}(\mathbf{n})$ , we also measured the anisotropy in the angular distribution of the center to center distances, which is characterized by  $\mathcal{L}^d(\mathbf{n})$ . Eq. A.9 shows the expansion of  $\mathcal{L}^d(\mathbf{n})$ , involving parameters  $\mathcal{L}_{\alpha\beta}^d$ . All the measured components of  $\mathcal{L}_{\alpha\beta}^d$  are small.  $\mathcal{L}_{12}^d$  has the largest value, of the order of  $10^{-3}$ , which is nearly the same for different  $P^*$  and  $I$  values. The positive sign of  $\mathcal{L}_{12}^d$  is in agreement with the result for  $\mathcal{F}_{12}^d$ , showing that the largest center to center distances (and so the weakest capillary forces) are oriented like receding pairs. Since the contacts and so the formation of liquid bridges mostly happen in the direction of approaching pairs, it could be regarded as a consequence

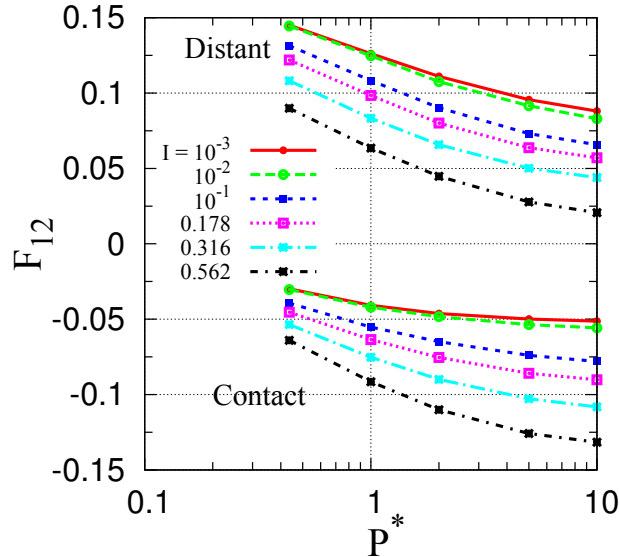


Figure 2.30: Fabric parameter  $F_{12}$  for contacts and distant interactions versus  $P^*$  for different  $I$  values.

of hysteretic nature of the liquid bridges.

### 2.3.4 Calculation of stress components from microscopic parameters

The anisotropy of the orientation of pairs and of the angular distribution of force intensities are investigated in the previous sections. We also qualitatively studied the influence of the anisotropies on the shear stress. Herein, we propose an approximate equation between each stress component and the microscopic parameters for both the contributions of contacts and distant interactions. The results are compared to their values from the direct measurements.

#### Contribution of contacts to shear stress

Expansions of  $E(\mathbf{n})$  and  $\mathcal{F}(\mathbf{n})$  can be injected in Eq. 2.23, to express the components of tensor  $\underline{\underline{\sigma}}^{N,c}$  as functions of the microscopic parameters. The equations are derived in Appendix A for the diagonal (Eq. A.12) and non-diagonal (Eq. A.13) components of the stress tensor. By replacing  $\Omega$  with  $\pi N a^3 / (6\Phi)$  in Eq. A.12, the shear stress will be:

$$\sigma_{12}^{N,c} = \frac{3\Phi z_c}{\pi a^2} \langle F^{N,c} \rangle [F_{12}^c + \mathcal{F}_{12}^c] \quad (2.25)$$

This shows that the contribution of normal contact forces to shear stress (or internal friction) partly stem from the anisotropy in the orientation of contacts that are more often oriented in the direction of the approaching pairs, those that mostly interact by repulsive forces. The larger intensity of the contact normal forces in the direction of the approaching pairs, which is characterized by  $\mathcal{F}_{12}^c$ , is another source of the shear strength. The values of coefficient  $3\Phi z_c / (\pi a^2)$  are given in Tab. 2.11. Tab. 2.8 compares the predictions of Eq. 2.25 to the directly measured values of  $\sigma_{12}^{N,c}$ . The results are in good agreement, with a difference lower than 5% in most cases.

On comparing Fig. 2.30 to Fig. 2.31b one observes that, for small values of  $P^*$  and  $I$ , force anisotropy  $\mathcal{F}_{12}^c$  has the dominant contribution to  $\sigma_{12}^{N,c}$ . As we increase  $P^*$  or  $I$ , this contribution tends to decrease and that of fabric parameter  $F_{12}^c$  to increase. Tab. 2.9 gives the contribution of fabric anisotropy to the shear stress for the different values of  $P^*$  and  $I$ .

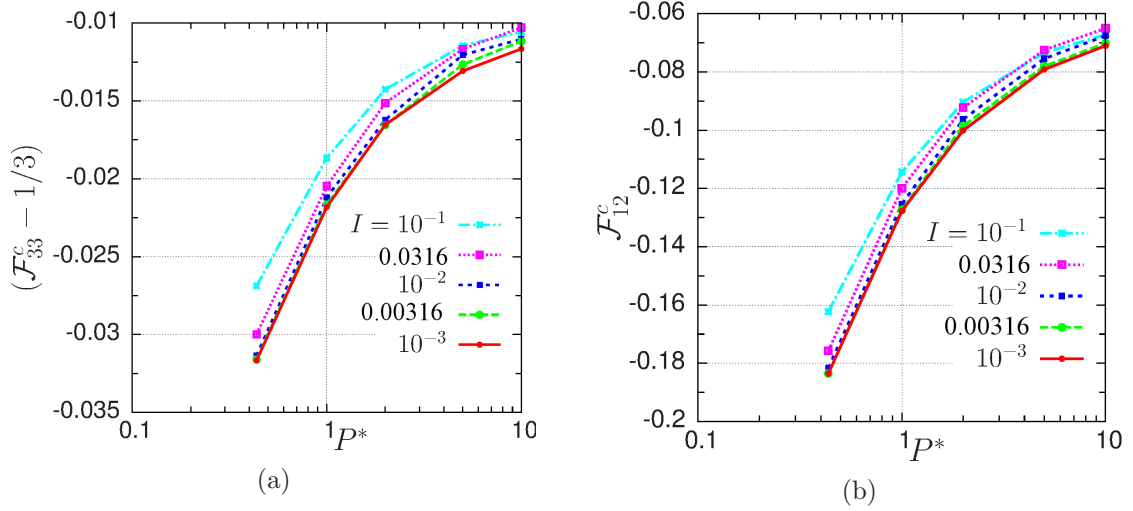


Figure 2.31:  $(\mathcal{F}_{33}^c - 1/3)$  (a) and  $\mathcal{F}_{12}^c$  (b) components of force anisotropy versus  $P^*$  for different values of  $I$ .

	$P^* = 0.436$		$P^* = 1$		$P^* = 10$		$P^* = \infty$	
$I$	Micro.	Direct	Micro.	Direct	Micro.	Direct	Micro.	Direct
0.562	-0.803	-0.804	-0.681	-0.683	-0.551	-0.574	-0.530	-0.561
0.316	-0.755	-0.741	-0.623	-0.611	-0.499	-0.505	-0.480	-0.534
$10^{-1}$	-0.693	-0.662	-0.538	-0.511	-0.400	-0.393	-0.382	-0.409
$10^{-2}$	-0.674	-0.641	-0.508	-0.474	-0.345	-0.330	-0.320	-0.334
$10^{-3}$	-0.671	-0.639	-0.508	-0.474	-0.341	-0.325	-0.315	-0.327

Table 2.8: Comparison of the direct measurements of  $\sigma_{12}^{N,c}$  to the results of Eq. 2.25 for different values of  $P^*$  and  $I$ .

$I$	$P^* = 0.436$	$P^* = 1$	$P^* = 2$	$P^* = 5$	$P^* = 10$	$P^* = \infty$
0.562	0.27	0.40	0.47	0.55	0.58	0.60
0.316	0.25	0.38	0.46	0.53	0.56	0.59
$10^{-1}$	0.19	0.33	0.42	0.50	0.54	0.57
$10^{-2}$	0.14	0.25	0.33	0.41	0.45	0.50
$10^{-3}$	0.14	0.24	0.31	0.38	0.42	0.48

Table 2.9: Relative contribution of fabric anisotropy to  $\sigma_{12}^{N,c}$  for different values of  $P^*$  and  $I$ .

### Contribution of distant interactions to shear stress

Eq. A.14 and Eq. A.15 are derived for the calculation of the contribution of distant interaction to the stress components, from the microscopic parameters. By replacing  $\Omega$  with  $\pi N a^3 / (6\Phi)$  for the shear stress we obtain:

$$\sigma_{12}^d = \frac{3\Phi z_d l_0}{\pi a^2} \langle F^{N,d} \rangle \left[ F_{12}^d + \mathcal{F}_{12}^d + \mathcal{L}_{12}^d \right]. \quad (2.26)$$

$l_0$  in this equation is the average center to center distant between the distant interactions normalized by particle diameter  $a$ , about 1.025 for all  $P^*$  and  $I$  values. The values of the coefficient are listed in Tab. 2.11. For large  $P^*$  values, the contribution of distant interactions

is very small. Tab. 2.10 shows the good agreement between the results of Eq. 2.26 and the results of the direct measurement, for two small values of  $P^*$ . Note that  $\mathcal{L}_{12}^d$  is very small and does not significantly affect the result.  $\mathcal{F}_{12}^d$  varies between -0.05 and -0.03, which reduces the shear stress  $\sigma_{12}^d$ . Consequently, for the distant interactions the main source of the shear strength is the anisotropy of the orientation of pairs. The contributions of fabric anisotropy  $F_{12}^d$  in  $\sigma_{12}^d$  are displayed in the last two columns of Tab. 2.10.

$I$	$P^* = 0.436$		$P^* = 1$		$P^* = 0.436$	$P^* = 1$
	Micro.	Direct	Micro.	Direct		
0.562	-0.066	-0.069	-0.015	-0.019	1.656	2.926
0.316	-0.089	-0.092	-0.032	-0.035	1.462	1.892
$10^{-1}$	-0.094	-0.094	-0.045	-0.047	1.310	1.479
$10^{-2}$	-0.073	-0.072	-0.038	-0.039	1.251	1.356
$10^{-3}$	-0.069	-0.069	-0.036	-0.037	1.256	1.356

Table 2.10: Comparison of the direct measurements of  $\sigma_{12}^d$  to the results of Eq. 2.26 (left side) and the contribution of fabric anisotropy to  $\sigma_{12}^d$  (right side) for different values of  $P^*$  and  $I$ .

$I$	$P^* = 0.436$		$P^* = 1$		$P^* = 10$		$P^* = \infty$
	A1	A2	A1	A2	A1	A2	A1
0.562	3.449	-1.214	2.958	-0.686	2.410	-0.091	0.718
0.316	3.558	-1.209	3.131	-0.725	2.602	-0.104	1.113
$10^{-1}$	3.436	-1.937	3.176	-0.615	2.755	-0.103	1.812
$10^{-2}$	3.177	-1.628	3.033	-0.413	2.793	-0.074	2.444
$10^{-3}$	3.144	-1.601	3.011	-0.387	2.785	-0.063	2.548

Table 2.11: Values of the coefficient  $3\Phi_{z_c}\langle F^{N,c} \rangle / (\pi a^2)$  (labeled by A1) and the coefficient  $3\Phi_{z_d}l_0\langle F^{N,d} \rangle / (\pi a^2)$  (labeled by A2) for different values of  $P^*$  and  $I$ .

In addition to the shear stresses, we also measured the normal stress components for contacts and distant interactions. Appendix B compares the results from microscopic estimations to the results of direct measurements. Compared to the results for the shear stress, the errors of the microscopic approximation of the normal stresses are noticeable, as large as 25% for some data with small  $P^*$  and large  $I$  values. For larger  $P^*$  and smaller  $I$  values the results are closer to the direct measurements and the errors decrease below 10%.

### 2.3.5 Microscopic origin of normal stress differences

As we discussed in Sec. 2.2.5, the normal contact forces have the dominant contribution to the first and second normal stress differences. Here, we calculate the first normal stress difference due to the contact forces,  $N_1^c (= \sigma_{11}^{N,c} - \sigma_{22}^{N,c})$ , from the microscopic parameters and we compare the results to the direct measurements. We also investigate the influence of the fabric and force anisotropies on  $N_1^c$ . We can calculate the first normal stress difference from Eq. A.12, as

$$N_1^c = \frac{3\Phi_{z_c}}{\pi a^2} \langle F^{N,c} \rangle [(F_{11}^c - F_{22}^c) + (\mathcal{F}_{11}^c - \mathcal{F}_{22}^c)]. \quad (2.27)$$

Tab. 2.12 compares the results of the above equation to the direct measurements. The



results are in agreement for large values of  $P^*$  and  $I$ , but at small values of  $P^*$  and  $I$ , the approximation becomes inaccurate, underestimating the true value by more than 50%.

$I$	$P^* = 0.436$		$P^* = 1$		$P^* = 5$		$P^* = 10$	
	Micro.	Direct	Micro.	Direct	Micro.	Direct	Micro.	Direct
0.562	0.197	0.202	0.142	0.144	0.121	0.119	0.112	0.117
0.316	0.130	0.152	0.103	0.108	0.080	0.075	0.077	0.069
$10^{-1}$	0.059	0.089	0.044	0.060	0.023	0.024	0.017	0.016
$10^{-2}$	0.028	0.059	0.016	0.033	-0.004	-0.003	-0.009	-0.010
$10^{-3}$	0.021	0.054	0.016	0.035	-0.004	-0.002	-0.013	-0.013

Table 2.12: Comparison of the direct measurements of  $N_1^c$  to the result of Eq. 2.27, for different values of  $P^*$  and  $I$ .

The evolutions of fabric and force anisotropy terms in Eq. 2.27 are displayed in Fig. 2.32 as functions of  $I$ , for different  $P^*$  values. The increase of the term  $(F_{11}^c - F_{22}^c)$  with  $I$  shows that the contacts tend to align with the direction of the flow for large  $I$ . For small  $P^*$  it is more difficult to violate the isotropy of the contacts which are confined in the clusters, and so the rate of change of fabric anisotropy decreases. In the limit of small  $P^*$ , and for the largest  $I$  values,  $(\mathcal{F}_{11}^c - \mathcal{F}_{22}^c)$  and consequently the average intensity of normal forces in direction  $x_1$  increase. The fabric and force anisotropies both enhance  $N_1^c$  in this range but the influence of the anisotropy of contact orientation becomes dominant as we increase the value of  $P^*$ . The curves in the limit of small  $I$  and large  $P^*$  values show that the negative sign of  $N_1^c$  in this limit is due to the change in the favoured orientation of the contacts and of the strong normal forces.

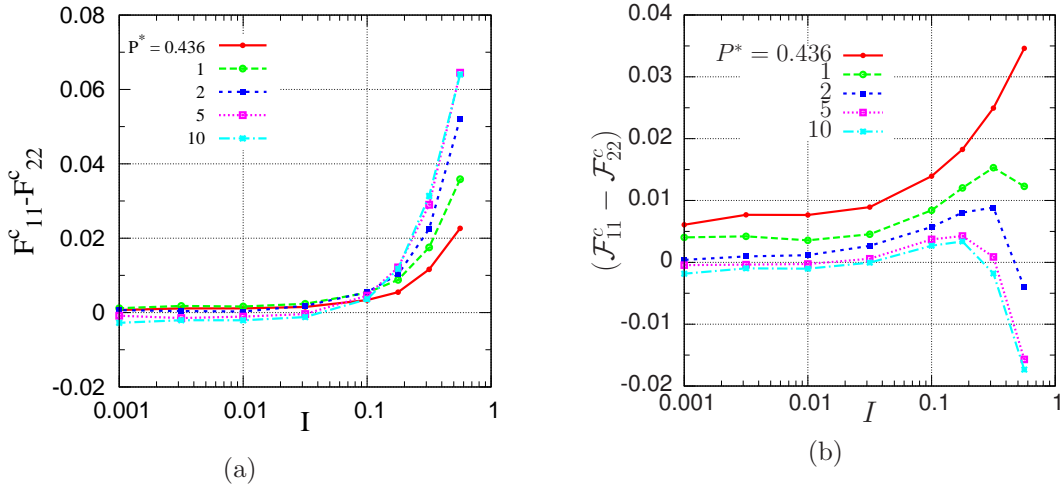


Figure 2.32: Fabric anisotropy  $(F_{11}^c - F_{22}^c)$  (a) and force anisotropy  $(\mathcal{F}_{11}^c - \mathcal{F}_{22}^c)$  (b) terms versus  $I$  for different values of  $P^*$ .

The errors in the microscopic approximation of the second normal stress difference,  $N_2^c$ , are large and the results are quite far from the direct measurements. However, in the quasistatic limit, the anisotropy parameters in Fig. 2.33 show a similar trend as  $N_2^c$  in Fig. 2.15b. For small values of  $I$ , for which the force anisotropy has the dominant contribution to  $N_2^c$ , increasing  $P^*$  causes a strong increase in  $(\mathcal{F}_{22}^c - \mathcal{F}_{33}^c)$ , starting from a relatively large value about 0.02 up to a value larger than 0.04. For small  $P^*$  values, the variations of  $N_2^c$  and of the anisotropy parameters with  $I$  are similar but for smaller capillary forces they vary in

opposite directions. As we increase the flow rate, the influence of  $P^*$  on the sum of the two anisotropy terms,  $(\mathcal{F}_{22}^c - \mathcal{F}_{33}^c)$  and  $(F_{22}^c - F_{33}^c)$ , decreases, while the variations of  $N_2^c$  with  $P^*$  also decrease.

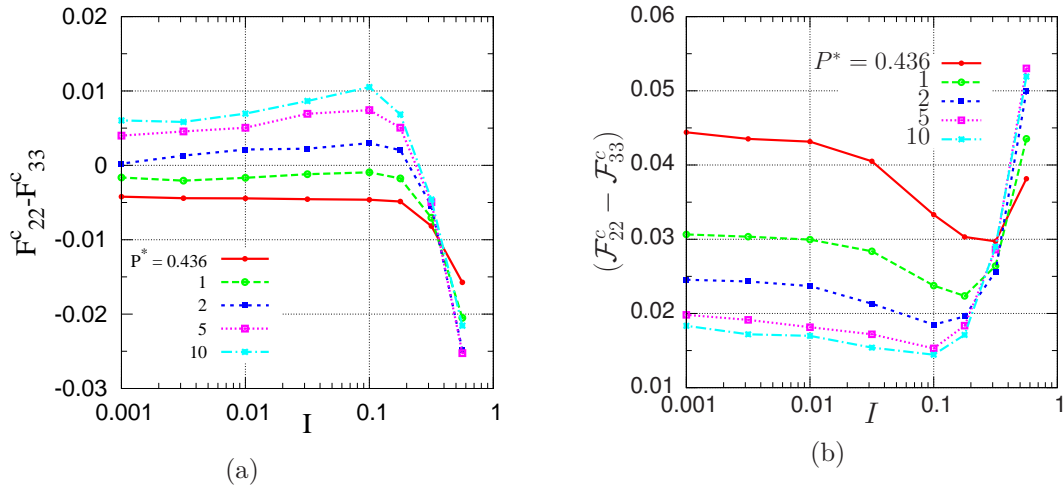


Figure 2.33: Fabric anisotropy  $(F_{22}^c - F_{33}^c)$  (a) and force anisotropy  $(\mathcal{F}_{22}^c - \mathcal{F}_{33}^c)$  (b) terms versus  $I$  for different values of  $P^*$ .

### 2.3.6 Influence of capillary force model on microscopic behaviours

The influence of the capillary force model on the macroscopic behaviour is discussed in Sec. 2.2.6. Here, we report the effect of the force model on the microscopic behaviour of the material.

#### Influence of the force range and meniscus volume

The contact coordination number does not change much with the force range or meniscus volume. Setting  $D_0 = 0$  (instead 0.1 of the standard case) or decreasing the volume of the meniscus from the standard value  $V = 10^{-3}$  down to  $10^{-6}$ , just leads to a small decrease of  $z_c$ , e.g., from 5 to 4.7 in the quasistatic limit, when  $P^* = 0.436$ . However, it has a strong influence on  $z_d$ . Compared to the standard case, for  $P^* = 0.436$  and small values of  $I$ , it decreases from 0.9 down to a value below 0.3 when we set  $D_0 = 0.01$ , or down to about zero when we set  $V = 10^{-6}$ . In this range of  $P^*$  and  $I$  values, the fabric parameter  $F_{12}^c$  undergoes a small decrease, at most from -0.03 to -0.04. The results show similar values for other anisotropy factors,  $(F_{11}^c - F_{22}^c)$  and  $(F_{ozz}^c - 1/3)$ . However,  $F_{12}^d$  changes a lot, from 0.15 down to 0.12 for  $D_0 = 0.01$  or down to 0.09 for  $V = 10^{-3}$ .

#### Influence of capillary force hysteresis

In Sec. 2.2.6 we showed that changing the rule of liquid bridge formation has a significant effect on macroscopic behaviour. If we assume that the liquid bridge forms right after two particle approach a distance below  $D_0$ , instead forming at contact, the number of contacts slightly increases, e.g., in the quasistatic limit and  $P^* = 0.436$ ,  $z_c$  increases about 5%. For these values of  $P^*$  and  $I$ , we see a strong increase of  $z_d$  about 70%. The values of fabric parameters due to contacts, are equivalent, but when the menisci form at  $D_0$ , more distant interactions can be found in the direction of approaching pairs and  $F_{12}^d$  exhibits a strong decrease from 0.15 to 0.07.

### 2.3.7 Agglomeration

The aggregation of cohesive grains is observed and reported in many numerical and experimental studies. Gilabert *et al.* [54, 55] studied the aggregation of particles in a 2D model powder under isotropic pressure. Rognon *et al.* [122] reported the increase of the porosity due to the agglomeration in the simulation of the shear flow of 2D cohesive grains. Ennis *et al.* [122] studied the agglomeration mechanism in powder granulation. An experimental study on the granulation of the wet powders is also presented by Talu *et al.* [144]. In reference [90], the aggregation of dilute and dense granular materials is studied by measuring the fluctuations in the local concentration of the particles in a simple shear flow of wet powders. A numerical study on the steady state 3D Chute flow is performed by Brewster *et al.* [20], reporting the increase of the number of long-lasting contacts in the presence of the cohesive forces. Weber *et al.* in [150], carried out a detailed study of the effect of capillary forces on agglomerate duration and size.

We observed in Sec. 2.3.1 that the coordination number of contacts and the solid fraction vary in opposite directions. We explained that this effect is a consequence of the agglomeration of the particles. We also argued in Sec. 2.3.3 that the decrease of  $|F_{12}^c|$  for smaller values of  $P^*$  is a result of the tumbling motion of the grain clusters within the flow. On the other hand, we found in Sec. 2.2.4 that the significant effect of the capillary forces on the microscopic behaviour could not be understood only by directly adding the effects of these forces. In this section, we study and characterize the agglomeration phenomena in the presence of capillary forces. First, we measure the age of the contacts and distant interactions and the possible influence of the control parameter on durability of the individual pairs. Then, we characterize the agglomeration effect with the size and duration of clusters and the effect of  $P^*$  and  $I$  on the properties of the clusters. We use the information to explain our observations of the macroscopic properties, particularly the strong influence of the capillary forces on the solid fraction and the internal friction.

#### Age of contacts and of distant interactions

The distribution of the age  $\tau^c$  of contacts for  $I = 10^{-1}$  and different values of  $P^*$  is shown in Fig. 2.34.  $P(\tau^c\dot{\gamma})$  is the probability distribution of contact ages  $\tau_c$ , expressed as a function of strain  $\tau^c\dot{\gamma}$ . The decrease of  $P(\tau^c\dot{\gamma})$  is slower for smaller  $P^*$ , showing that for the stronger cohesive forces the contacts survive over larger strain intervals [20, 150]. For large strain intervals, the curves might be described with an exponential function,  $P(\tau^c\dot{\gamma}) \propto e^{-\tau^c/\tau_0^c}$ , in which  $\tau_0^c$  is the decay time of the age of contacts. We measure  $\tau_0^c$  by fitting an exponential function to the data in Fig. 2.34, for all  $\tau^c\dot{\gamma} > 0.5$ . The results are given in the second column of Tab. 2.13, showing that the decay time increases as we decrease  $P^*$ . Average contact ages,  $\tau_{\text{avg}}^c$ , are displayed in the third column of this table, which show the same behaviour. Since the slope of the curve increases for smaller strain interval, which is not considered in the fit,  $\tau_{\text{avg}}^c$  is smaller than  $\tau_0^c$ . The inset in Fig. 2.34, which is plotted for a shorter range of  $\tau^c\dot{\gamma}$  values, displays the decrease of the slope with  $\tau^c\dot{\gamma}$ .

Fig. 2.35 shows the evolution of the pdf with  $I$  for two different values of  $P^*$ . The results show that the age of the contacts (in units of  $1/\dot{\gamma}$ ) decreases in faster flows. For  $I \leq 10^{-2}$ , we do not see a significant difference between the curves, showing nearly quasistatic behaviour. The probability distribution function of the age of interaction  $P(\tau^i\dot{\gamma})$  (or the pdf of the age of liquid bridges) is also illustrated in Fig. 2.36 for different values of  $P^*$ . The liquid bridges survive for quite large strain intervals, reaching several units of strain with probability of order 0.1. As the capillary force increases the slope of the curve and so the average age of the menisci also increases. The rate of this increase is even larger for smaller values of  $P^*$ . For very small values of strain interval,  $\tau^i\dot{\gamma} \lesssim 1$ , in the inset of Fig. 2.36, the slope decreases

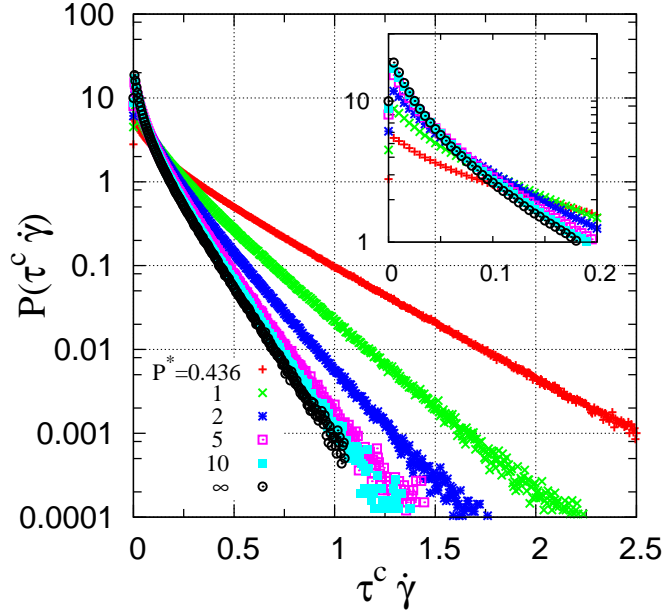


Figure 2.34: Distribution of the age of contacts for different values of  $P^*$  and  $I = 0.1$ . Inset shows the same graph in a shorter range of  $\tau^c \dot{\gamma}$ .

reaching a plateau near zero. It shows that most of the liquid bridges survive at least for a few tens of unit strain. However, in the midrange ( $1 \lesssim \tau^i \dot{\gamma} \lesssim 3$ ), the curves have the largest slope. Here again we fit an exponential function to the curves, by defining  $\tau_0^i$  as the decay time of the age of distant interactions. The variation of  $\tau_0^i$  and also average age of the interactions  $\tau_{\text{avg}}^i$  with  $P^*$ , is displayed in Tab. 2.13. Note that here again, due to the larger slopes of the curves in midrange, the values of  $\tau_{\text{avg}}^i$  is smaller than  $\tau_0^i$ . We do not see any noticeable difference between the curves for different values of  $I$ . The pairs may loose their contacts in faster flows, but they are still bounded with the liquid bridges and cannot leave the cluster.

We conclude that the evolutions of the age of contacts and of distant interactions reveal the formation of aggregates in the presence of capillary forces. These clusters are transported by the flow for some distance before they are broken or restructured. They may survive for strain intervals of a few units, which confirms our previous discussion, in Sec. 2.3.3, of the influence of  $P^*$  on the anisotropy of contact orientations. The influence of the agglomeration on macroscopic behaviours could be explained with this scenario (as in [122]): considering the sketch in Fig. 2.27, approaching pairs have to tumble, one grain moving over the other, while they are pressed against each other in the shear flow. As the pair is then oriented in the receding quadrant, the liquid bridge might break if the distance reaches  $D_0$ . In the similar motion of larger clusters their finite deformability and multiple connections might prevent their rupture into a pair of separate objects during the receding phase.

## Clusters

Particles glued by liquid bridges can form large clusters which significantly influence the shear strength and the solid fraction of granular material. Here, we study the influence of the capillary forces and the flow rates on the size and duration of these clusters. First we need to define the clusters by requesting all contacts or liquid bonds to have reached a minimum age,  $\tau^{\text{cl}}$ . We measure the size of the clusters for different values of  $\tau^{\text{cl}}$  in the range of

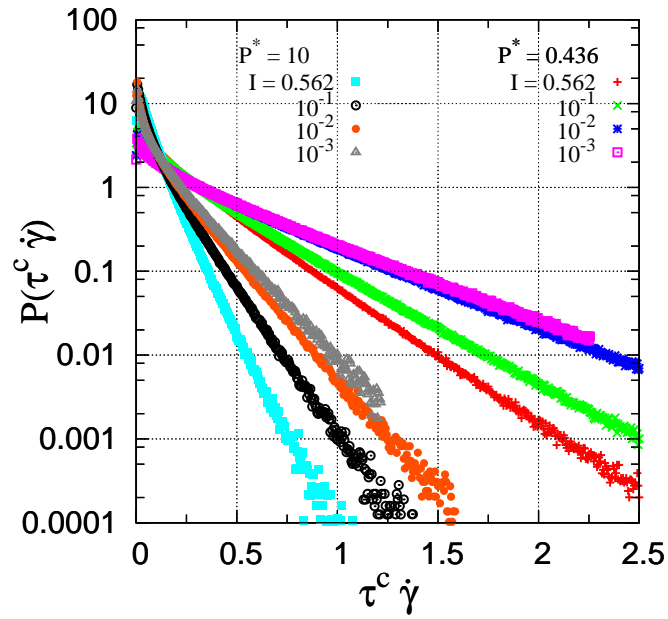


Figure 2.35: Distribution of the age of contacts for different values of  $I$  and two different values of  $P^*$ .

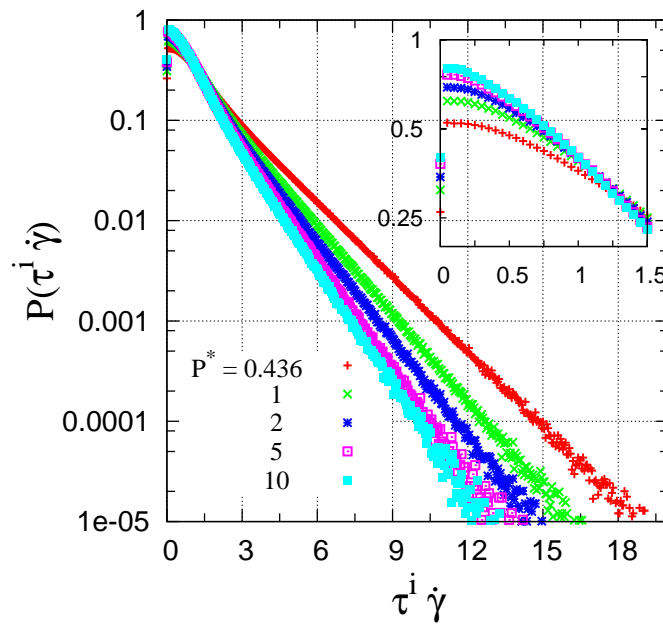


Figure 2.36: Distribution of the age of all interaction for different values of  $P^*$  (same for all values of  $I$ ). Inset shows the same graph in a shorter range of  $\tau^i \dot{\gamma}$ .

$P^*$	$\dot{\gamma}\tau_0^c$	$\tau^c\dot{\gamma}_{\text{avg}}$	$\dot{\gamma}\tau_0^i$	$\tau^i\dot{\gamma}_{\text{avg}}$
0.436	0.306	0.258	1.704	1.609
1	0.180	0.154	1.437	1.325
2	0.153	0.111	1.295	1.187
5	0.128	0.087	1.164	1.072
10	0.120	0.080	1.102	1.021
$\infty$	0.118	0.074	—	—

Table 2.13: Decay time of age distribution function for contacts,  $\tau_0^c$ , and force all interactions,  $\tau_0^i$ , obtained by an exponential fit to the data of Fig. 2.34 and Fig. 2.36); average contact age  $\tau_{\text{avg}}^c$  and interaction age  $\tau_{\text{avg}}^i$ , for different values of  $P^*$  and  $I = 0.1$ . All three parameters are normalized by shearing time  $1/\dot{\gamma}$ .

$0.25 \leq \tau^{\text{cl}}\dot{\gamma} \leq 5$ . Fig. 2.37b displays the number of clusters  $N^{\text{cl}}$  versus their size  $S^{\text{cl}}$ . Note that every data point counts the number of clusters in the interval of  $n/4 < \log_{10}(S^{\text{cl}}) \leq (n+1)/4$  with  $1 \leq n < 20$ .  $N^{\text{cl}}$  is averaged over the results of several configurations in steady state shear flow. The results of Fig. 2.37b are obtained for  $P^* = 0.436$  and different values of  $I$ , only considering the clusters with  $\tau^{\text{cl}}\dot{\gamma} \geq 2$ . The sample typically comprises a number of small clusters (e.g., more than 200 clusters consist of 2 or 3 grains, regardless of the value of  $I$ ), and a few large ones. One huge may contain a significant proportion of the grains in the whole system. One interesting result in Fig. 2.37a is that the distribution of the size of clusters for the smallest reduced pressure ( $P^* = 0.436$ ) is nearly the same for  $I = 10^{-2}$  and  $10^{-3}$  as the quasistatic limit is approached, in agreement with the other macroscopic and microscopic results. As we increase  $I$ , the large clusters break into smaller ones and consequently the number of clusters of intermediate size increases while large clusters become scarce. Fig. 2.37b represents the similar results for clusters which have sustained a strain of 5 units, showing the same trends as Fig. 2.37a, with smaller cluster sizes (clusters of several tens of grains are still present, albeit scarce).

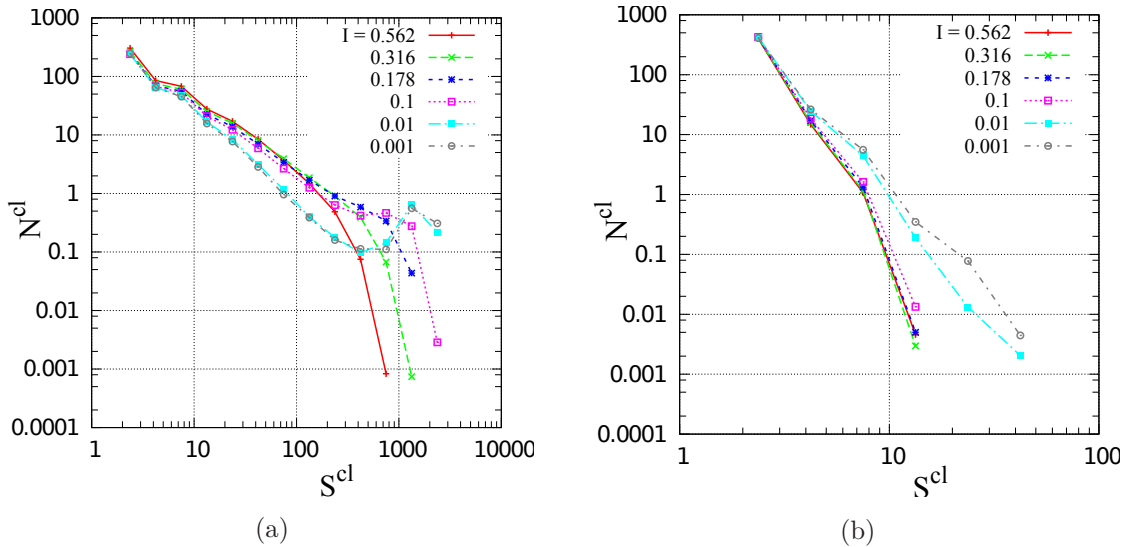


Figure 2.37: Number of clusters  $N^{\text{cl}}$  versus size of clusters  $S^{\text{cl}}$  for  $P^* = 0.436$  and different values of  $I$ . Only clusters that survive for the strain interval  $\dot{\gamma}\tau^{\text{cl}} = 2$  (a) or  $\dot{\gamma}\tau^{\text{cl}} = 5$  (b) count.

The results in Fig. 2.37 should be compared to those in Fig. 2.38 that are plotted for a larger value of  $P^*$  and two different values of  $\tau^{\text{cl}}\dot{\gamma}$ . The number of the large clusters, for larger values of  $P^*$ , is decreased while larger numbers of small clusters (more than 500 clusters for  $P^* = 10$ ) consisting of 2 or 3 particles are formed in the material. The lifetime of these scarce clusters is also lower than for  $P^* = 0.436$  such that for  $\tau^{\text{cl}}\dot{\gamma} \geq 3$  almost no cluster with  $S^{\text{cl}} > 10$  appears (Fig. 2.38b), and we observe that only about 100 clusters including 2 or 3 particles can sustain shear strains as large as 5.

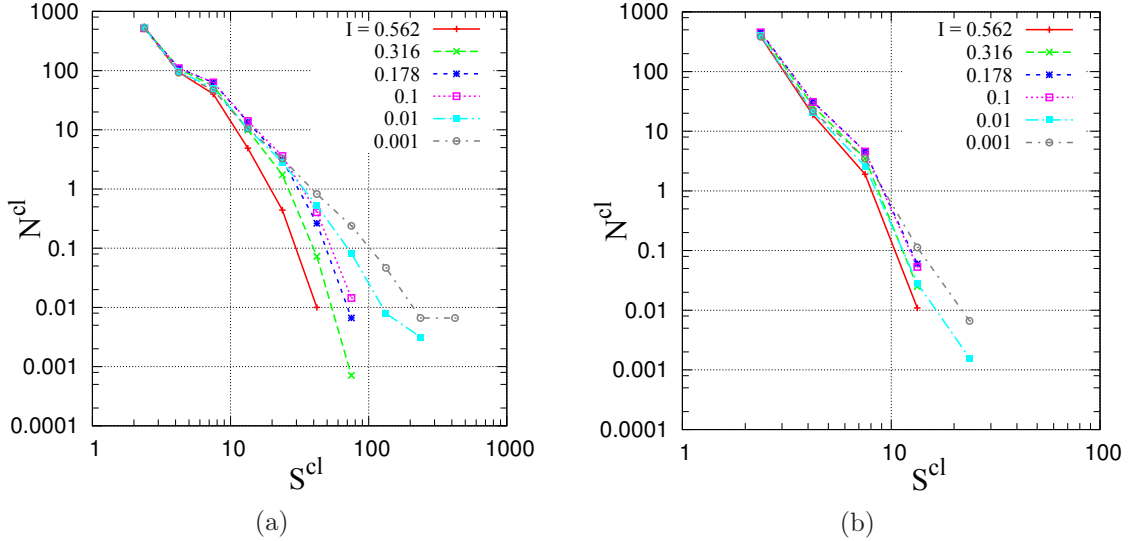


Figure 2.38: Number of clusters  $N^{\text{cl}}$  versus size of clusters  $S^{\text{cl}}$  for  $P^* = 10$  and different values of  $I$ . Only clusters that survive for the strain interval  $\dot{\gamma}\tau^{\text{cl}} = 2$  (a) or  $\dot{\gamma}\tau^{\text{cl}} = 3$  (b) count.

To characterize the intensity of the clustering effect we calculate the mass average of the cluster sizes as below:

$$\langle S^{\text{cl}} \rangle_{\text{m}} = \frac{\sum_i (S_i^{\text{cl}})^2}{\sum_i S_i^{\text{cl}}}, \quad (2.28)$$

in which the summations run over all the clusters with size  $S^{\text{cl}}$ . The results for  $\langle S^{\text{cl}} \rangle_{\text{m}}$  for the different values of  $P^*$  and  $I$  are shown in Fig. 2.39, as functions of  $\tau^{\text{cl}}\dot{\gamma}$ . For small values of  $\tau^{\text{cl}}\dot{\gamma}$  almost all particles are gathered in a single cluster and so we have only one cluster including about 4000 grains, which results in  $\langle S^{\text{cl}} \rangle_{\text{m}} \simeq 4000$ . For large values of  $\tau^{\text{cl}}\dot{\gamma}$  most particles are isolated or part of a very small cluster, and so a value close to 1 for  $\langle S^{\text{cl}} \rangle_{\text{m}}$  is expected. In the midrange of  $\tau^{\text{cl}}\dot{\gamma}$ ,  $\langle S^{\text{cl}} \rangle_{\text{m}}$  decreases with  $P^*$  and  $I$  showing that for stronger capillary forces or slower flows several small clusters are replaced by a few large clusters.



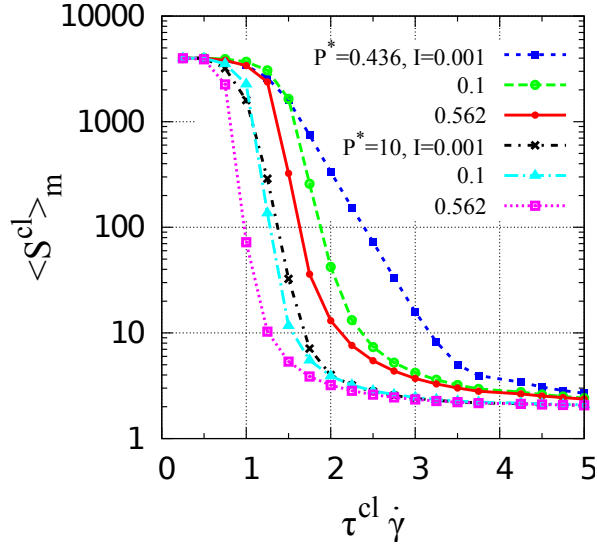


Figure 2.39: Mass average,  $\langle S^{cl} \rangle_m$ , versus cluster age  $\tau^{cl} \dot{\gamma}$  for different values of  $P^*$  and  $I$ .

## 2.4 Summary and discussion

In this chapter we studied the rheological properties of unsaturated granular materials, when due to a small amount of liquid in the system, the liquid bridges between particles form and create capillary forces. We focused on the pendular state, for which the liquid phase is completely discontinuous and no coalescence occurs between liquid bridges. The homogeneity of the flow was studied and we showed that localization may occur for small values of  $P^*$ . On investigating the flow homogeneity we showed that the localization patterns are regular and persistent for  $P^* = 0.1$ , and that the localization tendency of the flow increases for smaller values of inertial number. However, strong localization was also observed for large values of the inertial number ( $I \geq 0.178$ ). In this range of  $I$ , the velocity patterns show that the flow is completely concentrated within a shear bands with a thickness of one or two particle diameters, but in the slow flow ( $I \leq 10^{-2}$ ) the shear bands are thicker, between 5 and 10 particle diameters. The homogeneity of the flow was verified for all values of  $P^* \geq 0.436$ , for which well-defined steady state conditions under controlled normal stress were obtained.

The influence of the capillary forces on the material rheology was studied, based on the constitutive laws, and observed to be important. In the presence of the liquid bridges, the solid fraction can reach very small values (e.g., 0.52 for  $P^* = 0.436$  in the quasistatic limit) which cannot be observed in cohesionless systems. We also observed that the internal friction of unsaturated granular materials is considerably larger than in the dry system. For  $P^* = 0.436$ , the macroscopic friction coefficient,  $\mu^*$ , was measured 2.5 times as large as its value for dry grains. In contrast to the dry granular materials, for small enough values of  $P^*$ , wet granular assemblies can form loose and stable structures. Despite this strong influence of capillary forces, our measurements showed that the capillary forces only contribute about 10% to the total shear stress. As a consequence, the influence of the capillary interactions on the macroscopic properties cannot be expressed only as an additive effect due to the isotropic capillary pressure (as usually proposed, based on effective stress ideas). The effect of the capillary force model was studied, showing a negligible influence of the meniscus volume on the solid fraction and a moderate effect on the shear stress, within the saturation range of the pendular state. In addition, an important influence of the distant interacting pairs and

the hydraulic hysteresis on mechanical properties were observed.

The microscopic properties of unsaturated granular material were investigated, in which the contributions of contacts and the distant interactions were distinguished. The results showed that for the smaller values of  $P^*$  the coordination number of the contacts slightly increases while the solid fraction of the system decreases. We explain this behaviour with the clustering effect: the particles strongly attract their close neighbours with the capillary forces. Consequently, the particles agglomerate and form certain structures of clusters which increase the void space and the porosity of the system. The distribution of normal forces was studied showing that for larger values of  $I$  and smaller values of  $P^*$  the slope of the distribution of repulsive force decreases and so the force network can support stronger repulsive forces.

We observed that the anisotropy of the orientation of distant interactions and the anisotropy of the angular distribution of contact forces increase for smaller values of  $P^*$ , which induce shear strength in the material. The anisotropies in the system with different components of fabric tensor and force anisotropy parameters was characterized and we related these parameters to different stress components. The contribution of the force anisotropies increases for smaller values of  $I$  and  $P^*$  up to 85% for  $P^* = 0.436$  in the quasistatic limit, however for the cohesionless material the fabric and the force anisotropies have about the same contribution. Finally we studied the agglomeration phenomenon with calculations of contact and interaction age distributions, cluster sizes and lifetimes. We showed the age of the contacts and distant interactions to increase for smaller  $P^*$  values, as well as the size and the age of the clusters. We concluded that the formation of large and long-lasting clusters is the main reason of the strong influence of capillary forces on rheological properties.

It is interesting to compare the quasistatic constitutive law obtained in Eq. 2.13 with the Coulomb yield criterion, as defined in Fig. 1.1. Defining  $\mu^* = |\tau|/\sigma$  and using  $F_0/a^2$  as the unit of stress, Eq. 2.13 may be written as:

$$\tau = \mu_{\infty}^* \sigma + B \sigma^{1-\beta}. \quad (2.29)$$

Fig. 2.40 plots the above equation and also the equation for a dry material ( $\tau = \mu_{\infty}^* \sigma$ ) with the parameters ( $\mu_{\infty}^* \simeq 0.34, B = 0.27$  and  $\beta = 0.82$ ) obtained in our simulations. Note that the range of  $\sigma$  in our study, with unit of stress  $F_0/a^2$ , is between 0.436 and 10. Within this range the graph, at first sight, may appear linear, in agreement with the Coulomb yield criterion. However, discrepancies are predicted for the lower values of pressure, as (??) predicts  $\tau \rightarrow 0$  for  $\sigma \rightarrow 0$ , and for larger values of pressure too as its increase is slightly faster. Actually the observed yield locus  $\sigma - P$  is not a straight line and the calculations of Coulomb cohesion by means of a fit to experimental data might be inaccurate. We can estimate the apparent Coulomb cohesion, assuming that the yield locus is a straight line between  $(\sigma, \tau)$  and  $(2\sigma, \tau(2\sigma))$ . Using Eq. 2.29 the slope of the line would be  $(\mu_{\infty}^* + 0.036\sigma^{-0.82})$ . Thus the apparent Coulomb cohesion is:

$$c_{\text{app}} = 0.234 \sigma^{0.18}$$

which varies between 0.202 and 0.354 as  $\sigma$  grows from 0.436 to 10.

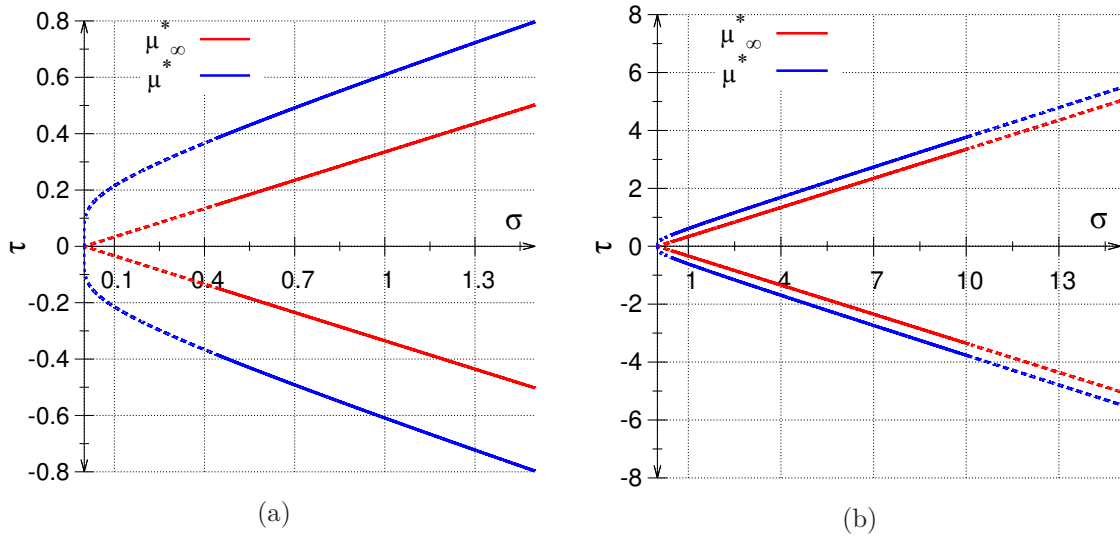


Figure 2.40: (a) Eq. 2.29 with stress unit  $F_0/a^2$  (blue line) and in the dry case,  $\tau = \mu_\infty^* \sigma$  (red line). (b) Same graph for a larger range of  $\sigma$ . Dashed lines are out of the investigation range.

## Chapter 3

# Rheology of very dense, viscous suspensions

We now present another numerical study in which the interstitial liquid affects the granular dynamics by its viscosity. The study of dense suspensions or granular pastes, which we report on in this chapter, was tackled with a “granular” point of view and a “granular framework”, as outlined in Sec. 1.5, on dealing with the very dense limit, when hydrodynamic forces are dominated by near-neighbour lubrication forces. The system dynamics, however, is dealt with in the limit of vanishing Reynolds number, and devoid of inertia, with the consequence that the numerical method is quite different from standard DEM, and based on matrix computations. Although the treatment of intergranular contacts was adapted to deal with dense systems in a physically reasonable way, and the use of a pressure controlled set-up greatly contributes to smooth out the singularities associated with the approach to jamming, we were confronted with the numerical difficulties mentioned in Sec. 1.5, which we have only imperfectly overcome. As a consequence, the results are still somewhat incomplete in some respects, and call for more extensive calculations, relying on improved numerical methods. In particular, we could not obtain statistically relevant results for frictional spheres. Nevertheless, we shall see that our results, although still restricted in their scope, do confirm conjectures, provide a few relevant measurements and suggest questions and perspectives for further studies.

### 3.1 Numerical suspension model

#### 3.1.1 Interactions

We implement the model outlined in Sec. 1.5.2, with the sole near-neighbour hydrodynamic resistance matrix elements, and a cut-off at short distance, as introduced in connection with Fig. 1.24.

We consider assemblies of  $N$  equal-sized spherical beads of diameter  $a$  enclosed in a cuboidal simulation cell, and immersed in a Newtonian fluid of viscosity  $\eta_0$ . The edges of the cell are parallel to the unit vectors  $\mathbf{e}_1$ ,  $\mathbf{e}_2$ ,  $\mathbf{e}_3$  that define the coordinate axes and have lengths  $L_1$ ,  $L_2$ ,  $L_3$ , the cell volume being denoted as  $\Omega = L_1 L_2 L_3$ . Beads interact through hydrodynamic lubrication forces – we implement the Ball-Melrose approach [11, 137], exploiting the assumption of lubrication force dominance, as introduced in Sec. 1.5.2. The hydrodynamic forces are pairwise additive and couple neighbouring particles at distance (between surfaces)  $h \leq h_{\min}$ .

As  $\xi_N(h)$  does not diverge as  $h \rightarrow 0$ , interparticle contacts should be considered. In the

present chapter, we only report on the simplest model, involving frictionless particles with normal contact forces. Those are evaluated with linear unilateral contact elasticity, relating normal elastic force  $F_N$  to contact deflection  $h$  as

$$F_N = K_N h, \quad (3.1)$$

involving a spring constant,  $K_N$ . Whenever two particles come into contact, we simply add the viscous hydrodynamic force to normal contact force (3.1).

Stress components are given by the quasi-static form of Eq. 1.15:

$$\sigma_{\alpha\beta} = \frac{1}{\Omega} \sum_{1 \leq i < j \leq N} \mathbf{F}_{ij}^{\alpha} \mathbf{r}_{ij}^{\beta}, \quad (3.2)$$

where only the interacting pairs contribute to the sum, and  $\mathbf{r}_{ij}$  is the “branch vector”, pointing from the center of  $i$  to the center of  $j$ . On writing (3.2) we conform to the usual soil mechanics convention, used throughout the present report, that tensile stresses are negative.

### 3.1.2 Boundary conditions

Our systems are subjected to simple shear flows in which a macroscopic motion along direction  $x_1$  is set up, with velocity gradient  $\dot{\gamma}$  along direction  $x_2$ . This flow is imposed within the periodic cell with the Lees-Edwards procedure of Sec. 1.3.3 (see Fig. 1.17), which is now standard in the simulation of homogeneously sheared suspensions [39, 135, 93]. The control of the normal stress is however an innovation in this context: while  $L_3$  and  $L_1$  are fixed, the cell height  $L_2$  in the direction of the velocity gradient is allowed to fluctuate in order to maintain normal stress  $\sigma_{22}$  equal to a prescribed value  $\Sigma_{22}$  up to a small tolerance. Consequently, volume  $\Omega$  and solid fraction  $\Phi$  will also fluctuate about some average values characterizing the state of the flowing suspension in steady flow. Although this is the procedure applied in the DEM simulations of Chapter 2, we need to specify how it is adapted to the viscous, Stokesian dynamics of our suspension model. In the Lees-Edwards procedure, the simulation cell, in which coordinate  $x_2$  is bounded by  $\pm L_2/2$ , is periodically replicated in all directions, but its copy along direction  $x_2$  (for which  $L_2/2 \leq x_2 \leq 3L_2/2$ ) is moved in the  $x_1$  direction by a shift  $\Delta$  such that

$$\frac{d\Delta}{dt} = \dot{\gamma} L_2, \quad (3.3)$$

in which  $L_2$  is evolving in time. As usual, quantities pertaining to any interacting pair  $i, j$ , such as branch vector  $\mathbf{r}_{ij}$  which is used to compute stresses by formula (3.2), should be defined on associating with  $i$  the appropriate image of  $j$  (the nearest one) by the group of translations defined by the cell periodicity.

Particle velocities are conveniently parametrized on writing, for any  $i$ ,  $1 \leq i \leq N$ , with  $-L_2/2 \leq x_i^{(2)} \leq L_2/2$ ,

$$\mathbf{V}_i = \tilde{\mathbf{V}}_i + \dot{\gamma} x_i^{(2)} \mathbf{e}_1 - \dot{\epsilon} x_i^{(2)} \mathbf{e}_2 \quad (3.4)$$

While velocities  $\tilde{\mathbf{V}}_i$  are periodic, the other terms in (3.4) correspond to global strain rates.  $\dot{\epsilon}$  is a notation for ratio  $-\dot{L}_2/L_y$ . In the evaluation of relative velocity  $\delta\mathbf{V}_{ij}$  that entails hydrodynamic forces by (1.62), difference  $y_j - y_i$ , which appears in formula (1.61) because of (3.4), should be adequately computed with the nearest image convention too.

### 3.1.3 Hydrodynamic resistance matrix, equations of motion

As forces are only sensitive to *relative* velocities, the motion is determined up to a global rigid body translation (rigid rotations are forbidden by the cell periodicity) and it is convenient to

impose  $\tilde{\mathbf{V}}_1 = 0$ . One thus has  $N_f = 3N - 2$  degrees of freedom in the considered central force case ( $\xi_T = 0$ ), while  $\mathbf{V}$  would be  $6N - 2$ -dimensional in the general case. A corresponding ( $N_f$ -dimensional) hydrodynamic force vector  $\mathbf{F}^H$  can be defined on gathering coordinates of forces  $\mathbf{F}_i^H$  (with  $i \geq 2$ ) (and of moments  $\mathbf{\Gamma}_i^H$  if  $\xi_T \neq 0$ ), and  $-\Omega\sigma_{yy}$ , with the tensor defined in (3.2). The power of hydrodynamic forces is the scalar product (in  $N_f$  dimensions)  $\mathbf{F}^H \cdot \mathbf{V}$ .

The equation of motion was written as (1.60), but we need to take into account the contact forces, and the effect of the externally imposed shear rate. In general, all resultants of non-hydrodynamic interparticle forces, such as contact or colloidal interactions, and all external force fields (such as gravity) are to be included in  $\mathbf{F}^{\text{ext}}$ . In the present case, all coordinates of the external force vector, which we denote as  $\mathbf{F}_{\Sigma}^{\text{ext}}$  are equal to zero except the last one,  $\Omega\Sigma_{22}$ . The vector containing the resultant of contact forces on all grains is denoted by  $\mathbf{F}_c$ . Shear rate  $\dot{\gamma}$  is enforced in the system by a manipulation of boundary conditions leading to relation (1.61). This amounts to applying a certain additional external force  $\dot{\gamma}\mathcal{F}$ , with a geometrically determined,  $\dot{\gamma}$  independent  $N_f$  dimensional vector  $\mathcal{F}$ . To evaluate  $\dot{\gamma}\mathcal{F}$ , one has to compute the interparticle forces corresponding to the  $\dot{\gamma}$  term in (1.61), deduce the corresponding interparticle hydrodynamic forces from (1.62), then compute the resulting contributions to  $\mathbf{F}_i^H$ ,  $\mathbf{\Gamma}_i^H$  (if necessary), and  $\sigma_{22}$ , and finally reverse their signs. The final equations of motion read:

$$\mathbf{V} = \underline{\underline{\Xi}}^{-1} \cdot [\dot{\gamma}\mathcal{F} + \mathbf{F}_c + \mathbf{F}_{\Sigma}^{\text{ext}}]. \quad (3.5)$$

### 3.1.4 Practical computation procedure

To integrate Eq. 3.5 and compute particle trajectories, the algorithm is as follows:

- (i) At time  $t$ , from the known positions of the particles in the simulation cell and the current values of  $\Delta$  and  $L_2$  we deduce the elements of matrix  $\underline{\underline{\Xi}}$  and the coordinates of vectors  $\mathcal{F}$ ,  $\mathbf{F}_c$  and  $\mathbf{F}_{\Sigma}^{\text{ext}}$ .
- (ii) We solve Eq. 3.5 by iterative techniques (see below), and thus find velocities and  $\dot{\epsilon}$ .
- (iii) We move the particles, temporarily, to their positions at time  $t + \Delta t$  as deduced to a first order (Euler explicit) scheme. We change  $\Delta$  and  $L_2$  accordingly.
- (iv) We use the temporary positions obtained at step (iii) to define a new  $\underline{\underline{\Xi}}$ , and recalculate the velocities with this matrix. The final move of the particles to their positions at time  $t + \Delta t$  uses the arithmetic average of the two previously calculated velocities. We thus implement the ‘‘trapezoidal rule’’ of order 2. We also update  $\Delta$  and  $L_2$ .

Time step  $\Delta t$  is corrected at each integration step so that:

$$\text{Max}_{i,j} \left\{ \frac{|\xi_N(h_{ij}(t + \Delta t)) - \xi_N(h_{ij}(t))|}{\xi_N(h_{ij}(t))}, \|\mathbf{n}_{ij}(t + \Delta t) - \mathbf{n}_{ij}(t)\| \right\} = x_{\text{obj}} \quad (3.6)$$

In this work, we set  $x_{\text{obj}}$  at 0.01. This condition ensures that the trajectories are determined with a satisfactory accuracy. Particles do not overlap, and we also check that distances between particles are consistently evaluated.<sup>1</sup>

To solve the linear system given by Eq. 3.5 we use the preconditioned conjugate gradient method. This method is derived from the conjugate gradient method which enables to solve a linear system of the type  $\underline{\underline{\Xi}} \cdot \mathbf{V} = \mathbf{F}$  in an iterative way. This method involves multiplications by matrix  $\underline{\underline{\Xi}}$ , which in our case amounts to directly computing the net effect of lubrication

<sup>1</sup>The strong lubrication effect entails that relative velocities of close neighbours are essentially tangential, and one has to make sure that the neglected higher order effects of this tangential motion do not spuriously affect the normal motion.

parameters	simulated systems
$\mathcal{V}i$	0.1, 0.05, 0.01, 0.005, 0.001, 0.0005
$N$	1372
$h_{\min}/a$	$10^{-4}$
$h_{\max}/a$	0.1
$\kappa$	$10^5$

Table 3.1: Parameters characterizing the different systems used in this work.

forces in neighbouring pairs, on applying Eqs. (1.61), (1.62) and (1.65)–(3.2). The conjugate gradient method has a very slow convergence rate and is quite sensitive to the accumulation of numerical errors. We can speed it up thanks to the use of a preconditioner, *i.e.* a matrix  $\underline{\underline{\Xi}}'$  which is close to  $\underline{\underline{\Xi}}$  and for which  $\underline{\underline{\Xi}}' \cdot \mathbf{V} = \mathbf{F}$  can be solved rapidly. We proceed in the following way: at some integration step, the resistance matrix is fully determined and factorized using complete Cholesky decomposition (exploiting its “skyline” structure, once particles are suitably renumbered). This matrix is thereafter used as a preconditioner for a certain number of integration steps. Note that in step ( $i$ ) of the algorithm, it is not necessary to build the resistance matrix explicitly unless its Cholesky factorization is about to be computed and the preconditioner updated. The Cholesky factorization is the slowest and most memory-consuming step in the whole computation procedure, but its great advantage is its robustness and ability to deal with ill-conditioned matrices (due to the divergence of  $\xi_N$  at small  $h$ ), for which the conjugate gradient algorithm without a preconditioner, or even with the “incomplete Cholesky” preconditioner used by [135], tend to fail. With the system sizes we study (up to  $N = 1372$ ) this method is still practical and the current random access memory capacities of tabletop computers are not exceeded. Average time step is dependent on  $\dot{\gamma}$  and the number of iterations required to simulate a shear strain equal to 1 ranges from  $10^2$  for  $\mathcal{V}i = 0.1$  to  $10^5$  for  $\mathcal{V}i = 0.0005$ . Computation times depend on shear rates and on system sizes: our longest simulation runs took a couple of weeks.

Initial configurations are obtained from simulations of densely packed granular assemblies, with the procedures presented in [1]. Isotropic configurations in periodic cubic cells at random close packing solid fraction  $\Phi_{\text{RCP}}$  are slightly expanded, so that close neighbours are separated by a distance at least equal to  $h_0 = 0.01$ , and the algorithm outlined above is then applied with a certain value of shear rate  $\dot{\gamma}$ , and the boundary conditions of Sec. 3.1.2. In the steady state flows we are interested in, the initial configuration becomes irrelevant after a transient and it is convenient, to minimize the duration of this initial stage, to start a simulation with a certain value of  $\dot{\gamma}$  from the final configuration obtained with the nearest previously studied value of  $\dot{\gamma}$ .

### 3.1.5 Dimensional analysis and state parameters

From the parameters of the problem, interstitial liquid viscosity  $\eta_0$ , particle diameter  $a$ , stiffness  $K_N$ , imposed stress  $\sigma_{22} = P$  and shear rate  $\dot{\gamma}$ , one extracts dimensionless parameters  $\mathcal{V}i$  (introduced in Eq. 1.66), ratios  $h_{\min}/a$  and  $h_{\max}/a$ , and reduced stiffness  $\kappa = K_N/(aP)$ .

Our simulations are carried out in systems of  $N=1372$  beads, with  $h_{\min}/a = 10^{-4}$ ,  $h_{\max}/a = 0.1$ , and  $5 \cdot 10^{-4} \leq \mathcal{V}i \leq 10^{-1}$ . These data are listed in Table 3.1



### 3.1.6 Macroscopic phenomena, rheology

#### Internal friction coefficient and solid fraction

The internal friction coefficient versus viscous number  $\mathcal{V}i$  is shown in Fig. 3.1a. We observe a gradual decrease as  $I$  decreases. From the accurate measurements of dry frictionless beads in shear flow carried out in [104] we expect for low  $\mathcal{V}i$  to retrieve the critical state value  $\mu^* \simeq 0.1$ . This limit is still not closely approached for the lowest studied value of  $\mathcal{V}i$ ,  $5 \times 10^{-4}$ . This is reminiscent of the observations made in [104], that the approach to the quasistatic limit is particularly slow with frictionless grains. Similarly, the solid fraction, although very high (larger than in most simulation results published),  $\Phi \simeq 0.625$ , is still not very close to the RCP value ( $\simeq 0.64$ ) that should be reached in the critical state of frictionless beads [104].

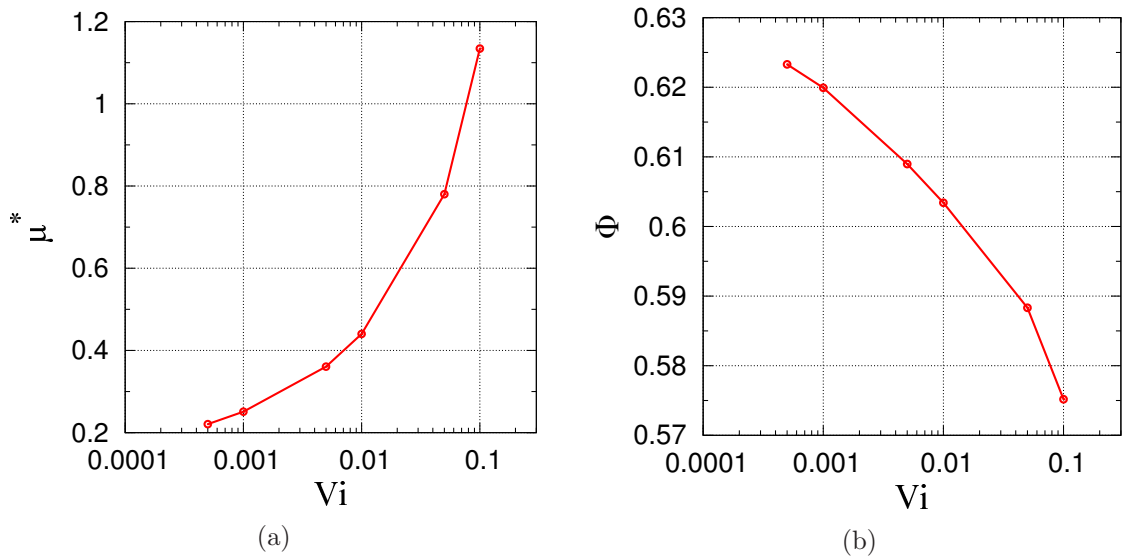


Figure 3.1: Effective friction coefficient  $\mu^*$  (a) and solid fraction  $\Phi$  (b) versus  $\mathcal{V}i$ .

#### Effective suspension viscosity

Fig. 3.2a shows the variation of effective viscosity  $\eta$ , relative to the viscosity  $\eta_0$  of the suspending liquid, as deduced from  $\mu^*$  by Eq. 1.67, as a function of solid fraction  $\Phi$ . As expected, we find that  $\eta/\eta_0$  is a strongly increasing function of  $\Phi$ , reaches quite high values for large solid fractions. The form of its divergence as  $\Phi_{\text{RCP}}$  is approached cannot, however, be accurately determined. Let us note, however, that no singularity is detected at  $\Phi < \Phi_{\text{RCP}}$ ... The pathological behaviour mentioned in Refs. [92, 10, 46] is likely due to the strong fluctuations in small size numerical samples sheared at constant volume.

#### Viscosity of a random isotropic suspension

We also measured the viscosity for a random isotropic suspension,  $\eta_i$ , as a function of  $\Phi$ . This value is obtained by instantaneous measurement of the viscosity in an isotropic random suspension subjected to a shear rate under a constant volume, before the action of shear flow selects a specific internal suspension structure.  $\eta_i$  characterizes a random configuration chosen with a uniform probability distribution in the set of all those for which particles are

not overlapping – i.e., according to the statistics of a hard sphere system<sup>2</sup>. To measure  $\eta_i$ , configurations at  $\Phi_{\text{RCP}}$  are first dilated to the desired solid fraction, then particles are attributed random velocities, an event-driven (hard-sphere molecular dynamics), conservative calculation is carried out at constant  $\Phi$ , particle collisions preserving until each particle has undergone 50 collisions on average. The results for different value of  $\Phi$  are represented in Fig. 3.2b. The values of  $\eta/\eta_0$  is quite below the viscosity in steady shear flow. The results are compared to those obtained by Sierou and Brady [136]. For small values of solid fraction, our results are slightly smaller, that might be due to the absence of long-range hydrodynamic interactions in our model. However, for larger solid fractions, we observe a faster increase, compared to the results by Sierou and Brady. The comparison of both graphs in Fig. 3.2

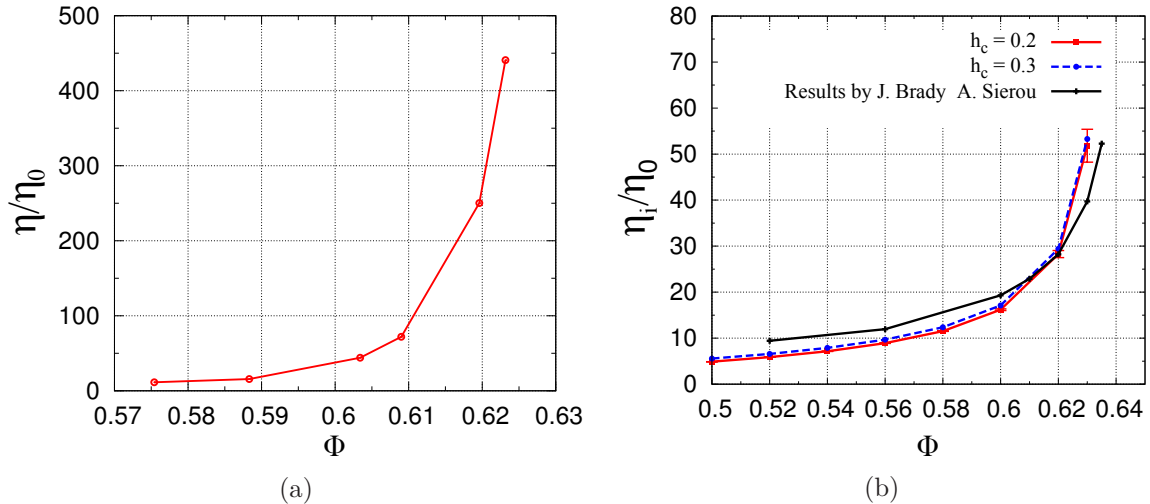


Figure 3.2: Effective viscosity in steady shear flow (a) and isotropic suspension viscosity (b) as a function of solid fraction  $\Phi$ .

shows that the steady-state velocity is considerably larger than its counterpart, measured in a random isotropic suspension at the same density. Thus, the distribution of distances and orientations of pairs of neighbours should greatly affect the shear stress. Let us also recall that the isotropic system of Fig. 3.2b is completely devoid of intergranular contacts.

### Contact contribution to shear stress

This contrasts with the important mechanical role of contacts in steady-state shear flow, as revealed by Fig. 3.3, in which the relative contribution of contact forces to shear stress is displayed. While viscous forces dominate for the largest values of  $\mathcal{V}i$ , in the approach to the quasistatic limit, as the velocity dependent terms vanish, the contact forces gradually take over and provide most of the shear stress.

### Normal stress differences

Like the dry or unsaturated granular systems of 2.2, our model viscous suspensions develop normal stress differences, as shown in Fig. 3.4 (we plotted  $-N_1$  and  $-N_2$  to represent them with the usual sign convention for stresses in fluid mechanics, which is opposite to the one used in this report). Remarkably, those differences vary rapidly in the investigated  $\mathcal{V}i$  interval, and become very small as  $\mathcal{V}i \rightarrow 0$ . Once again, the behaviour of dry grains (frictionless ones

<sup>2</sup>The equilibrium phase of the hard sphere fluid [60] is a crystal for  $\Phi \geq 0.53$ , and therefore a random isotropic configuration at larger solid fraction should belong to a metastable glassy state.

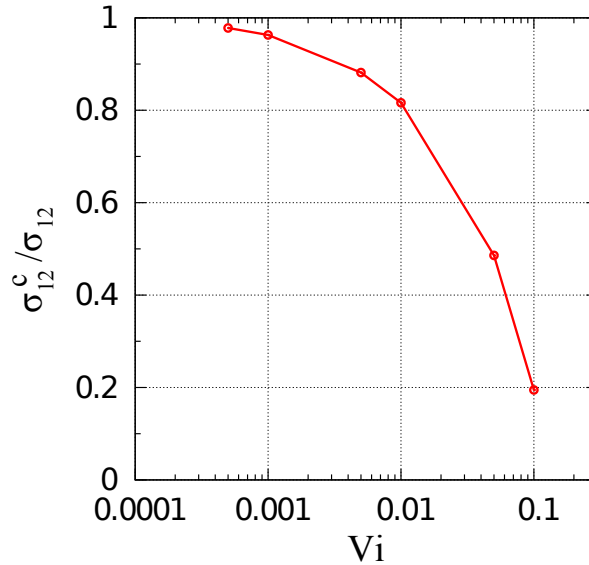


Figure 3.3: Contribution of contact forces on total shear stress,  $\sigma_{12}^c / \sigma_{12}$ , as a function of  $\mathcal{V}i$ .

in the present case) in the critical state is retrieved, for which in Ref. [104], normal stress differences  $N_1$  and  $N_2$  were extremely small, not distinguishable from zero.

### 3.1.7 Microscopic characteristics

One may analyse the microscopic origins of shear stress, applying ideas similar to those of Sec. 2.3.3.

#### Coordination numbers

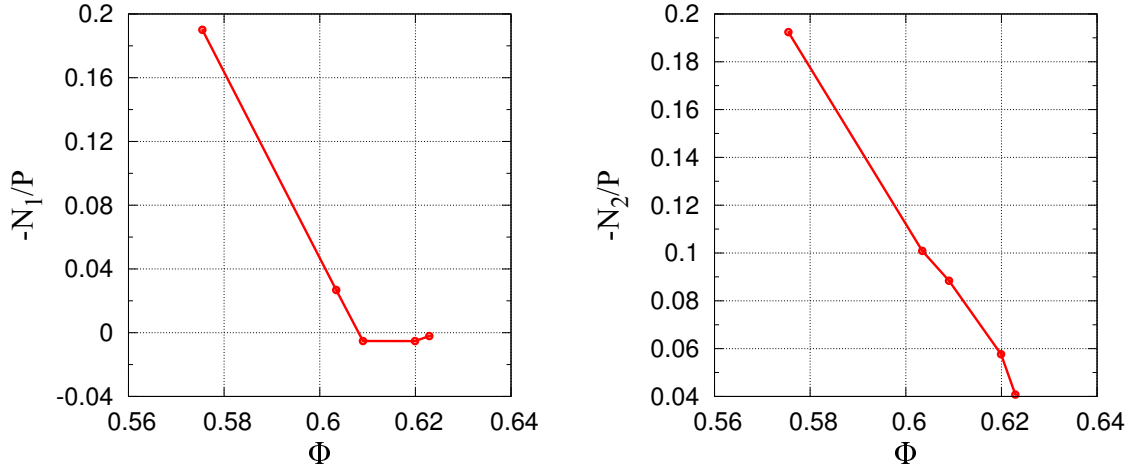
The average number of interacting pairs per grain is shown in Fig. 3.5, distinguishing between the coordination number of contacts,  $z_c$ , and the total number  $z$  of neighbours within viscous force range ( $h \leq h_{\max}$ ).  $z$  grows, like  $\Phi$ , for smaller  $\mathcal{V}i$  values.  $z_c$  should approach the critical value,  $z_c = 6$ , which is that of RCP states in that case, for  $\mathcal{V}i \rightarrow 0$ .

#### Fabric parameters

Finally, fabric parameters are shown in Fig. 3.6, both for all interactions (Fig. 3.6a) and for contacts (Fig. 3.6b). While notable values of  $F_{11} - F_{22}$  and  $F_{33} - 1/3$ , in agreement with results of normal stress differences, are observed for the lower densities, they tend to decrease for smaller  $\mathcal{V}i$ . With rigid, frictionless dry grains in shear flow, all those parameters, except  $F_{12}$ , were found negligible [104].

## 3.2 Conclusion

Our simulations show that the “granular” approach, in terms of internal friction and density laws, applies successfully to a model system for which the behaviour of rigid, perfectly lubricated grains is closely approached (we use a high value of  $\kappa$ , and a small asperity scale cutting off the lubrication effect for small gaps). Although the approach to the quasi-static limit (under constant  $P$ ) or, equivalently, to the concentration for which the viscosity diverges, is not



(a) First normal stress difference versus solid fraction. (b) Second normal stress difference versus solid fraction.

Figure 3.4: Normal stress differences.

probed with very high accuracy in this study, our results do argue in favour of a critical state identical to the one of dry grains in the quasistatic limit of  $\mathcal{V}i \rightarrow 0$ . No singularity, if grains are devoid of friction, occurs for  $\Phi < \Phi_{\text{RCP}}$ . It might be hoped to approach the quasi-static limit even closer, and then accurately characterize the diverging viscosities, on improving the numerical procedure (with, possibly, higher order schemes and/or more efficient solvers for the sparse system of linear equations). Many additional physical effects could also be introduced to this basic, reference model, such as various short-ranged forces and contact friction.

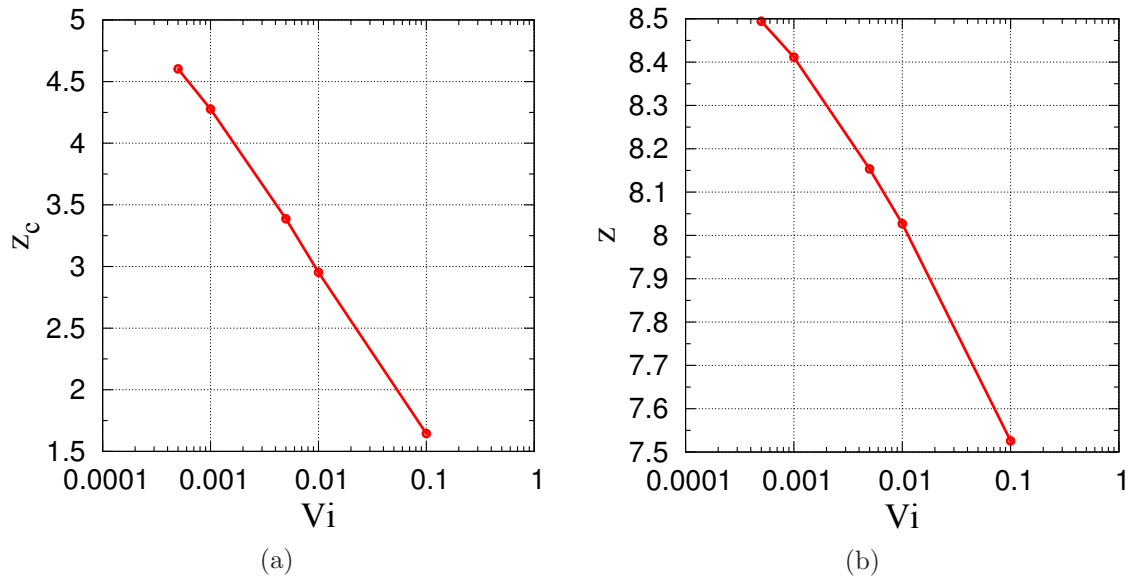


Figure 3.5

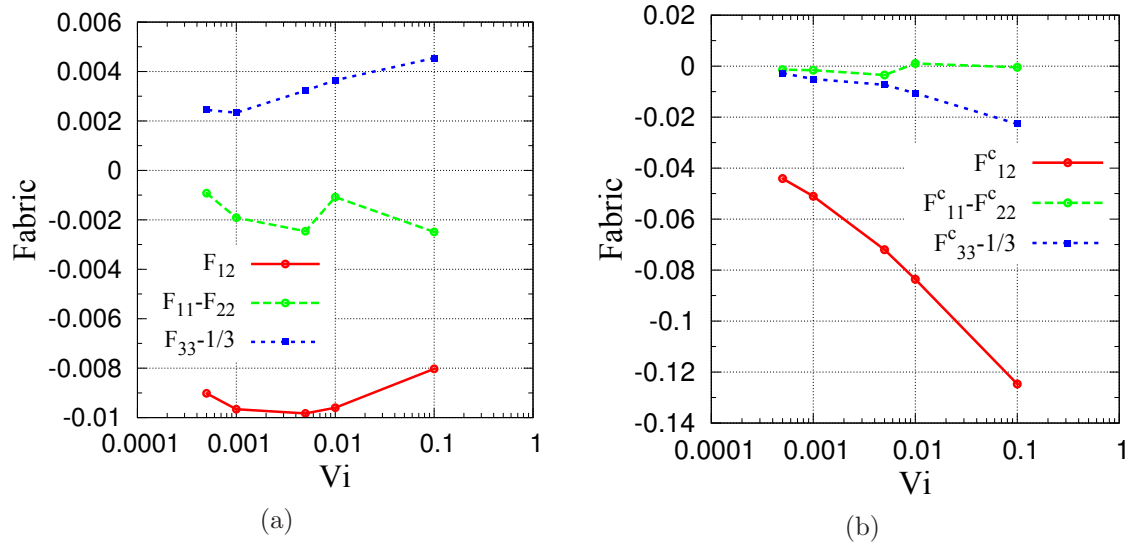


Figure 3.6: (a) Fabric parameters of neighbours at distance  $h_c = 0.1$  and (b) fabric parameters for contacts.



## Chapter 4

# Conclusions and perspectives

In the framework of this thesis, we studied the rheological behavior of wet granular materials either for small amounts of water in the presence of capillary interactions, or in fully saturated materials when the particles interact by viscous hydrodynamic forces. The rheology of unsaturated granular materials (in the pendular state) is studied in Chap. 2. The homogeneity of the flow is examined showing that localization may occur in the bulk of the material for small values of  $P^*$ . We observed a strong decrease of the solid fraction and a strong increase of the macroscopic friction coefficient to the values that cannot be observed in a cohesionless system. It reveals that compared to the cohesionless materials, wet granular materials under shear form much looser but more stable structures. We showed that the capillary effect cannot be described only as an additive isotropic pressure, and one also needs to study the microstructural changes due to capillary forces. Our studies on the microscopic properties of the material revealed an opposite trend in the variations of the contact coordination number and of the solid fraction which indicates the agglomeration and formation of clusters. We also observed a strong influence of capillary forces on the age of contact and distant interactions. We showed that for the stronger capillary effect, the age and the size of the clusters increase, which explain the strong influence of the capillary forces on the rheology. The investigations on the anisotropy of the contact orientations and forces, induced by shear flow and capillary effect, showed that for large values of  $P^*$ , both the fabric and force anisotropies are equally at the origin of the shear stress, but for small values of  $P^*$  the contribution of the force anisotropy dominates.

For the saturations above the limit of the pendular regime, the liquid bridges start to merge and we enter the funicular regime. As we increase the saturation, we may pass through different regimes up to the fully saturated case when the dominant interactions are viscous hydrodynamic forces. Further studies on different regimes and the transitions between them are necessary in order to calculate and unify the rheological laws in a wide range of saturation including the dry grains and the suspensions. A coupled discrete element/lattice Boltzmann model [34] might be employed to introduce the capillary and viscous forces between particles. More investigations can be done on the localization phenomenon, and we need to study the influence of the stiffness number on the flow homogeneity. In our simulations we used a very simple model for liquid distribution, in which the volume of the liquid bridges is always constant in time and for all particles. So the dynamics of the menisci volume are not considered in our model and also the saturation may vary with the control parameters. Although we showed that the variation of the saturation in our simulations is small and does not affect the mechanical properties significantly, the dynamics of the menisci volume may have an important effect on the rheology and should be introduced in our model. On the other hand, such a more realistic model might permit studying some other features of wet granular material like the fluid migration within the shear bands (see Sec. 1.2.4).



In Chap. 3 we studied the rheological behavior of saturated granular materials when the grains are completely immersed in a Newtonian fluid. A lower cut-off distance for hydrodynamic forces is defined to permit the real contacts between particles. The variations of solid fraction and microscopic friction coefficient with viscous number are studied which shows that the results in quasistatic limit coincide with the dry grain results, as was expected. We observed that as we approach smaller values of the viscous number, the importance of the contact forces increases and they become dominant near the quasistatic limit. We showed that the effective viscosity of suspensions diverges as we approach the critical state solid fraction  $\Phi_c$  which coincides with the random close packing solid fraction of frictionless grains,  $\Phi_{\text{RCP}}$ . The effective viscosity of random isotropic suspensions is also measured, resulting the values below the steady flow results, but a similar divergence trend near random close packing solid fraction. It reveals the importance of the distribution of distances and orientation of pairs. We also studied the microscopic properties of the flow by calculating the coordination number and fabric parameters. In this study, we assumed that the particles are ideally frictionless. In a more realistic model the friction between contacts should be introduced.

# Appendices



# Appendix A

## Force and fabric Anisotropies, expression of stress components

### A.1 Expansions with anisotropy parameters

#### A.1.1 Arbitrary functions

Let us introduce spherical coordinate angles  $\theta, \varphi$ , w.r.t. coordinate axis  $Ox_3$ , with usual relations, for unit vector  $\mathbf{n}$ :

$$\begin{aligned}n_1 &= \sin \theta \cos \varphi \\n_2 &= \sin \theta \sin \varphi \\n_3 &= \cos \theta.\end{aligned}$$

We consider any real function  $f$  of normal vector  $f(\mathbf{n})$  such that  $f(-\mathbf{n}) = f(\mathbf{n})$  and expand it to second order in spherical harmonics.

$$f(\mathbf{n}) = f_0 + \sum_{m=-2}^2 c_2^m Y_2^m(\theta, \varphi) \quad (\text{A.1})$$

Parity  $f(-\mathbf{n}) = f(\mathbf{n})$  ensures vanishing of all coefficients  $c_l^m$  for  $l = 1$ .

Definitions of relevant spherical harmonic functions:

$$\begin{aligned}Y_2^0(\theta, \varphi) &= \frac{1}{2} \sqrt{\frac{5}{4\pi}} (3 \cos^2 \theta - 1) \\Y_2^{\pm 1}(\theta, \varphi) &= \mp \sqrt{\frac{15}{8\pi}} \sin \theta \cos \theta e^{\pm i\varphi} \\Y_2^{\pm 2}(\theta, \varphi) &= \frac{1}{2} \sqrt{\frac{15}{2\pi}} \sin^2 \theta e^{\pm 2i\varphi}\end{aligned}$$

and parity of  $f$  ensure that expansion A.1 may be rewritten as

$$\begin{aligned}f(\mathbf{n}) &= f_0 + \frac{5}{8} (3f_{33} - f_0) (3n_3^2 - 1) + 15[f_{13}n_1n_3 + f_{23}n_2n_3] \\&+ \frac{15}{4} [(f_{11} - f_{22})(n_1^2 - n_2^2) + 4f_{12}n_1n_2],\end{aligned} \quad (\text{A.2})$$

as remarked in [], using the following notations for appropriate moments of  $f$  on the unit

sphere  $S$  ( $d\Omega = \sin\theta d\theta d\varphi$ )

$$\begin{aligned} f_0 &= \frac{1}{4\pi} \int_S f(\mathbf{n}) d\Omega \\ f_{\alpha\beta} &= \frac{1}{4\pi} \int_S f(\mathbf{n}) n_\alpha n_\beta d\Omega \quad (1 \leq \alpha, \beta \leq 3) \end{aligned} \tag{A.3}$$

All coefficients of functions of  $\theta, \varphi$  appearing in the r.h.s. of Eq. (A.2) vanish for constant (isotropic)  $f$ . By construction one has:

$$f_{11} + f_{22} + f_{33} = f_0. \tag{A.4}$$

### A.1.2 Products, to leading order in anisotropy coefficients

On dealing with products of several functions  $f^{(1)}, f^{(2)}, \dots, f^{(p)}$ :

$$f = \prod_{k=1}^p f^{(k)},$$

we shall often neglect terms beyond order one in anisotropy coefficients  $c_l^m$ , so that denoting as  $C_l^m$  the coefficients of the expansion of product  $f$ , the following approximation is adopted:

$$C_2^m \simeq \sum_{k=1}^p c_2^m(k) \prod_{j \neq k} f_0^{(j)}. \tag{A.5}$$

One thus naturally assumes the following relation between averages over unit sphere  $S$ :

$$\frac{1}{4\pi} \int_S f d\Omega \simeq \prod_{k=1}^p f_0^{(k)} \tag{A.6}$$

### A.1.3 Fabric

The angular distribution of contact orientations  $E(\theta, \varphi)$  is defined and normalized such that  $\int_S E d\Omega = 1$ . It is customary to define fabric parameters  $F_{\alpha\beta}$  as

$$F_{\alpha\beta} = \int_S E(\mathbf{n}) n_\alpha n_\beta d\Omega,$$

differing from Eq.(A.3) by a factor of  $4\pi$ , whence the expansion:

$$\begin{aligned} E(\mathbf{n}) &= \frac{1}{4\pi} + \frac{5}{16\pi} (3F_{33} - 1)(3n_3^2 - 1) + \frac{15}{4\pi} [F_{13}n_1n_3 + F_{23}n_2n_3] \\ &\quad + \frac{15}{16\pi} [(F_{11} - F_{22})(n_1^2 - n_2^2) + 4F_{12}n_1n_2]. \end{aligned} \tag{A.7}$$

### A.1.4 Average normal force

The average normal force conditioned by contact orientation  $\mathbf{n}$  or  $\theta, \varphi$ , is conveniently written as  $\langle F^N \rangle \mathcal{F}(\mathbf{n})$ , extracting a constant factor of  $\langle F^N \rangle$ , the average normal force. One has, by definition:

$$\frac{1}{4\pi} \int_S \mathcal{F}(\mathbf{n}) E(\mathbf{n}) d\Omega = 1,$$

but our approximations – see (A.6) – imply that

$$\frac{1}{4\pi} \int_S \mathcal{F}(\mathbf{n}) d\Omega \simeq 1.$$

Applying definitions (A.3) to function  $\mathcal{F}$ , one may write

$$\begin{aligned} \mathcal{F}(\mathbf{n}) = & 1 + \frac{5}{4}(3\mathcal{F}_{33} - 1)(3n_3^2 - 1) + 15[\mathcal{F}_{13}n_1n_3 + \mathcal{F}_{23}n_2n_3] \\ & + \frac{15}{4}[(\mathcal{F}_{11} - \mathcal{F}_{22})(n_1^2 - n_2^2) + 4\mathcal{F}_{12}n_1n_2]. \end{aligned} \quad (\text{A.8})$$

### A.1.5 Branch vector

It is defined as the vector pointing from the center of one grain to the center of its interacting neighbour. For spherical grains, only its length matters, as its orientation is given by the unit normal vector. Let us define  $\mathcal{L}(\mathbf{n})$  as the ratio of its average length, conditioned by direction  $\mathbf{n} \in S$ , to the average diameter  $a$ , and denote its (dimensionless) average as  $l_0$ . Function  $\mathcal{L}(\mathbf{n})$  is then expanded like  $\mathcal{F}(\mathbf{n})$ , and it will be convenient to define

$$\mathcal{L}_{\alpha\beta} = \frac{1}{4\pi l_0} \int_S \mathcal{L}(\mathbf{n}) n_\alpha n_\beta d\Omega.$$

Thus

$$\begin{aligned} \frac{\mathcal{L}(\mathbf{n})}{l_0} = & 1 + \frac{5}{4}(3\mathcal{L}_{33} - 1)(3n_3^2 - 1) + 15[\mathcal{L}_{13}n_1n_3 + \mathcal{L}_{23}n_2n_3] \\ & + \frac{15}{4}((\mathcal{L}_{11} - \mathcal{L}_{22})(n_1^2 - n_2^2) + 4\mathcal{L}_{12}n_1n_2). \end{aligned} \quad (\text{A.9})$$

## A.2 Stress components to first order in anisotropy parameters

The contribution of *normal forces* to stresses are given by ( $z$  denoting coordination number,  $n$  the number density of grains)

$$\sigma_{\alpha\beta}^{\text{N}} = \frac{azn}{2} \langle F^{\text{N}} \rangle \int_S E(\mathbf{n}) \mathcal{F}(\mathbf{n}) \mathcal{L}(\mathbf{n}) n_\alpha n_\beta d\Omega. \quad (\text{A.10})$$

For *contact forces* between equal-sized beads (neglecting contact deflections),  $\mathcal{L}(\mathbf{n}) = 1$ . The corresponding contribution  $\sigma_{\alpha\beta}^{\text{Nc}}$  combines anisotropy parameters of fabric  $E$  and force  $\mathcal{F}$ , it is readily evaluated using expansions (A.7) and (A.8), and values of the following integrals:

$$\begin{aligned} \int_S n_\alpha^2 d\Omega &= \frac{4\pi}{3} \quad (1 \leq \alpha \leq 3) \\ \int_S n_\alpha^4 d\Omega &= \frac{4\pi}{5} \quad (1 \leq \alpha \leq 3) \\ \int_S n_\alpha^2 n_\beta^2 d\Omega &= \frac{4\pi}{15} \quad (1 \leq \alpha, \beta \leq 3, \beta \neq \alpha) \end{aligned} \quad (\text{A.11})$$

The final expressions might be rearranged using (A.4), resulting in the following formula for diagonal stress components: ( $\alpha = 1, 2$ , or  $3$ , no summation)

$$\boxed{\sigma_{\alpha\alpha}^{\text{N,c}} = \frac{nzca}{2} \langle F^{\text{N,c}} \rangle \left[ \frac{1}{3} + \left( F_{\alpha\alpha}^{\text{c}} - \frac{1}{3} \right) + \left( \mathcal{F}_{\alpha\alpha}^{\text{c}} - \frac{1}{3} \right) \right]}, \quad (\text{A.12})$$

while non-diagonal ones read ( $\alpha, \beta = 1, 2$ , or  $3$ ,  $\beta \neq \alpha$ )

$$\boxed{\sigma_{\alpha\beta}^{\text{N,c}} = \frac{nzca}{2} \langle F^{\text{N,c}} \rangle [F_{\alpha\beta}^{\text{c}} + \mathcal{F}_{\alpha\beta}^{\text{c}}]}. \quad (\text{A.13})$$

We use superscript c or d for parameters corresponding to contact or distant interactions. In general, anisotropy parameters for  $\mathcal{L}$  might also be introduced, whence a factor of  $l_0$  and terms  $\mathcal{L}_{\alpha\alpha} - 1/3$  or  $\mathcal{L}_{\alpha\beta}$  in formulae (A.12, A.13). This applies in particular to the contribution of distant capillary forces transmitted by liquid bridges. The result for diagonal and non-diagonal components of stress are

$$\sigma_{\alpha\alpha}^{\text{N,d}} = \frac{nz_{\text{d}}al_0}{2} \langle F^{\text{N,d}} \rangle \left[ \frac{1}{3} + \left( F_{\alpha\alpha}^{\text{d}} - \frac{1}{3} \right) + \left( \mathcal{F}_{\alpha\alpha}^{\text{d}} - \frac{1}{3} \right) + \left( \mathcal{L}_{\alpha\alpha}^{\text{d}} - \frac{1}{3} \right) \right], \quad (\text{A.14})$$

and

$$\sigma_{\alpha\beta}^{\text{N,d}} = \frac{nz_{\text{d}}al_0}{2} \langle F^{\text{N,d}} \rangle \left[ F_{\alpha\beta}^{\text{d}} + \mathcal{F}_{\alpha\beta}^{\text{d}} + \mathcal{L}_{\alpha\beta}^{\text{d}} \right]. \quad (\text{A.15})$$



## Appendix B

# Normal stress components, comparing microscopic estimation with direct measurements

Contribution of the normal contact forces to the normal stress components for different values of  $P^*$ , comparing the results of Eq. A.12 with the direct measurement:

$I$	$\sigma_{11}^{N,c}$		$\sigma_{22}^{N,c}$		$\sigma_{33}^{N,c}$	
0.562	1.307	1.544	1.110	1.342	1.032	1.118
0.316	1.298	1.505	1.168	1.353	1.092	1.167
$10^{-1}$	1.218	1.358	1.158	1.269	1.060	1.103
$10^{-2}$	1.119	1.234	1.091	1.175	0.968	1.003
$10^{-3}$	1.104	1.219	1.083	1.165	0.957	0.990

Table B.1:  $P^* = 0.436$ .

$I$	$\sigma_{11}^{N,c}$		$\sigma_{22}^{N,c}$		$\sigma_{33}^{N,c}$	
0.562	1.104	1.320	0.961	1.175	0.893	0.968
0.316	1.132	1.310	1.030	1.202	0.969	1.036
$10^{-1}$	1.112	1.234	1.068	1.174	0.996	1.043
$10^{-2}$	1.050	1.147	1.034	1.113	0.948	0.982
$10^{-3}$	1.043	1.139	1.027	1.105	0.940	0.973

Table B.2:  $P^* = 1$ .

$I$	$\sigma_{11}^{N,c}$		$\sigma_{22}^{N,c}$		$\sigma_{33}^{N,c}$	
0.562	0.903	1.098	0.790	0.980	0.717	0.790
0.316	0.940	1.075	0.863	1.006	0.799	0.849
$10^{-1}$	0.953	1.038	0.935	1.023	0.867	0.902
$10^{-2}$	0.947	1.007	0.956	1.017	0.889	0.913
$10^{-3}$	0.942	1.001	0.955	1.014	0.887	0.910

Table B.3:  $P^* = 10$ .

$I$	$\sigma_{11}^{N,c}$		$\sigma_{22}^{N,c}$		$\sigma_{33}^{N,c}$	
0.562	0.862	1.056	0.741	0.950	0.720	0.757
0.316	0.892	1.047	0.819	0.976	0.788	0.804
$10^{-1}$	0.907	1.003	0.898	0.994	0.847	0.862
$10^{-2}$	0.916	0.982	0.927	0.998	0.877	0.889
$10^{-3}$	0.918	0.982	0.929	0.998	0.882	0.894

Table B.4:  $P^* = \infty$ .

Contribution of the distant interactions to the normal stress components for different values of  $P^*$ , comparing the results of Eq. A.14 with the direct measurement:

$I$	$\sigma_{11}^d$		$\sigma_{22}^d$		$\sigma_{33}^d$	
0.562	-0.377	-0.350	-0.427	-0.396	-0.411	-0.396
0.316	-0.380	-0.350	-0.419	-0.386	-0.410	-0.395
$10^{-1}$	-0.299	-0.272	-0.320	-0.289	-0.319	-0.304
$10^{-2}$	-0.201	-0.183	-0.214	-0.192	-0.213	-0.204
$10^{-3}$	-0.192	-0.175	-0.204	-0.183	-0.204	-0.194

Table B.5:  $P^* = 0.436$ .

$I$	$\sigma_{11}^d$		$\sigma_{22}^d$		$\sigma_{33}^d$	
0.562	-0.210	-0.197	-0.241	-0.225	-0.235	-0.227
0.316	-0.226	-0.210	-0.251	-0.232	-0.248	-0.240
$10^{-1}$	-0.194	-0.179	-0.208	-0.189	-0.212	-0.203
$10^{-2}$	-0.131	-0.119	-0.139	-0.125	-0.143	-0.136
$10^{-3}$	-0.123	-0.112	-0.130	-0.117	-0.134	-0.128

Table B.6:  $P^* = 1$ .

$I$	$\sigma_{11}^d$		$\sigma_{22}^d$		$\sigma_{33}^d$	
0.562	-0.028	-0.028	-0.031	-0.030	-0.031	-0.031
0.316	-0.032	-0.031	-0.036	-0.034	-0.036	-0.035
$10^{-1}$	-0.033	-0.031	-0.035	-0.032	-0.036	-0.035
$10^{-2}$	-0.024	-0.023	-0.025	-0.023	-0.026	-0.025
$10^{-3}$	-0.020	-0.019	-0.021	-0.019	-0.022	-0.021

Table B.7:  $P^* = 10$ .

# References

- [1] Ivana Agnolin and Jean-Noël Roux. Internal states of model isotropic granular packings. i. assembling process, geometry, and contact networks. *Phys. Rev. E*, 76(6):061302, 2007.
- [2] Ivana Agnolin and Jean-Noël Roux. Internal states of model isotropic granular packings. ii. compression and pressure cycles. *Phys. Rev. E*, 76(6):061303, 2007.
- [3] Ivana Agnolin and Jean-Noël Roux. Internal states of model isotropic granular packings. iii. elastic properties. *Phys. Rev. E*, 76(6):061304, 2007.
- [4] Einat Aharonov and David Sparks. Shear profiles and localization in simulations of granular materials. *Phys. Rev. E*, 65(5):051302, 2002.
- [5] M. Allen and D. Tildesley. *Computer simulations of liquids*. Oxford University Press, Oxford, 1987.
- [6] B. Andreotti, Y. Forterre, and O. Pouliquen, editors. *Granular Media: Between Fluid and Solid*. Cambridge, Cambridge, UK, 2013.
- [7] T. Aste and D. Weaire. *The Pursuit of Perfect Packing*. Institute of Physics Publishing, Bristol, 2000.
- [8] E. Azéma and F. Radjai. Force chains and contact network topology in sheared packings of elongated particles. *Phys. Rev. E*, 85:031303, 2012.
- [9] E. Azéma, F. Radjai, R. Peyroux, and G. Saussine. Force transmission in a packing of pentagonal particles. *Phys. Rev. E*, 76:011301, 2007.
- [10] R.C. Ball and J.R. Melrose. Lubrication breakdown in hydrodynamic simulations of concentrated colloids. *Adv. Colloid Interface Sci.*, 59:19–30, 1995.
- [11] R.C. Ball and J.R. Melrose. A simulation technique for many spheres in quasi-static motion under frame-invariant pair drag and Brownian forces. *Physica A*, 247:444–472, 1997.
- [12] J. Biarez and P.-Y. Hicher. *Elementary Mechanics of Soil Behaviour*. A. A. Balkema, Rotterdam, 1993.
- [13] A.W. Bishop. The principle of effective stress. *Tecnisk Ukelab*, 39:859–863, 1959.
- [14] F. Blanc. *Rhéologie et microstructure de suspensions concentrées non browniennes*. PhD thesis, Université de Nice-Sophia Antipolis, 2011.
- [15] F. Blanc, É Lemaire, A. Meunier, and F. Peters. Microstructure in sheared non-brownian concentrated suspensions. *J. Rheol.*, 57:273–292, 2013.
- [16] F. Blanc, F. Peters, and É Lemaire. Local transient rheological behavior of concentrated suspensions. *J. Rheol.*, 55:835–854, 2011.
- [17] F. Boyer, É. Guazzelli, and O. Pouliquen. Unifying suspension and granular rheology. *Phys. Rev. Lett.*, 107:188301:1–5, 2011.
- [18] J. F. Brady and G. Bossis. Stokesian dynamics. *Annu. Rev. Fluid Mech.*, 20:111, 1988.
- [19] J. F. Brady and J. F. Morris. Microstructure of strongly sheared suspensions and its impact on rheology and diffusion. *J. Fluid Mech.*, 348:103–139, 1997.

- 
- [20] R. Brewster, G.S. Grest, J.W. Landry, and A.J. Levine. Plug flow and the breakdown of bagnold scaling in cohesive granular flows. *PRE*, 72:061301, 2005.
- [21] N.V. Brilliantov and T. Pöschel. Collision of adhesive viscoelastic particles. In Hinrichsen and Wolf [66], pages 189–209.
- [22] C. S. Campbell. Granular shear flows at the elastic limit. *Journal of Fluid Mechanics*, 465:261–291, 2002.
- [23] C. S. Campbell. Stress-controlled elastic granular shear flows. *Journal of Fluid Mechanics*, 539:273–297, 2005.
- [24] C.S. Campbell. Rapid granular flows. *Annu. Rev. Fluid Mech.*, 22:57–92, 1990.
- [25] C. Cassar, M. Nicolas, and O. Pouliquen. Submarine granular flows down inclined plane. *Phys. Fluids*, 17, 2005.
- [26] A. Castellanos. The relationship between attractive interparticle forces and bulk behaviour in dry and uncharged fine powders. *Advances in Physics*, 54:263–376, 2005.
- [27] A. Castellanos, J. M. Valverde, A.T. Perez, A. Ramos, and P.K. Watson. Flow regimes in fine cohesive powders. *Phys. Rev. Lett.*, 82:1156–1159, 1999.
- [28] A. Castellanos, J. M. Valverde, and M. A. S. Quintanilla. Aggregation and sedimentation in gas-fluidized beds of cohesive powders. *Phys. Rev. E*, 64:041304, 2001.
- [29] J. Christoffersen, M. M. Mehrabadi, and S. Nemat-Nasser. A micromechanical description of granular material behavior. *Journal of Applied Mechanics*, 48:339–344, 1981.
- [30] P. A. Cundall and O. D. L. Strack. A discrete numerical model for granular assemblies. *Géotechnique*, 29(1):47–65, 1979.
- [31] F. da Cruz, S. Emam, M. Prochnow, J.-N. Roux, and F. Chevoir. Rheophysics of dense granular materials: discrete simulation of plane shear flows. *Phys. Rev. E*, 72:021309, 2005.
- [32] Pierre Dantu. étude expérimentale d’un milieu pulvérulent compris entre deux plans verticaux et parallèles. *Annales des Ponts et Chaussées*, IV:193–202, 1967.
- [33] F. Darve, editor. *Manuel de rhéologie des géomatériaux*. Presses des Ponts et Chaussées, Paris, 1987.
- [34] J.-Y. Delenne, M. Mansouri, F. Radjaï, M.S. El Youssoufi, and A. Seridi. Onset of immersed granular avalanches by dem-lbm approach. *Advances in Bifurcation and Degradation in Geomaterials*, 11:109–115, 2011.
- [35] B.V. Derjaguin, V.M. Müller, and Y.P. Toporov. Effect of contact deformations on the adhesion of particles. *J. Colloid Interface Sci.*, 53:314–326, 1975.
- [36] J. Desrues and G. Viggiani. Strain localization in sand: an overview of the experimental results obtained in grenoble using stereophotogrammetry. *Int. J. Numer. Anal. Meth. Geomech.*, 28:279–321, 2004.
- [37] H. di Benedetto, T. Doanh, H. Geoffroy, and C. Sauzéat, editors. *Deformation characteristics of geomaterials: Recent investigations and prospects*, Lisse, 2003. Swets and Zeitlinger.
- [38] A. Donev, S. Torquato, and F. H. Stillinger. Pair correlation function characteristics of nearly jammed disordered and ordered hard-sphere solids. *Phys. Rev. E*, 71(1):011105, 2005.
- [39] D. I. Dratler and W. R. Schowalter. Dynamic simulations of suspensions of non-brownian hard spheres. *J. Fluid Mech.*, 325:53–77, 1996.
- [40] U. El Shamy and Gröger T. Micromechanical aspects of the shear strength of wet granular soils. *Int. J. Numer. Anal. Meth. Geomech.*, 32:1763–1790, 2008.
- [41] D. Elata and J. G. Berryman. Contact force-displacement laws and the mechanical behavior of random packs of identical spheres. *Mechanics of Materials*, 24:229–240, 1996.
- [42] S. Emam, J.-N. Roux, J. Canou, A. Corfdir, and J.-C. Dupla. Granular packings assembled by rain deposition: an experimental and numerical study. In García Rojo et al. [51], pages 49–52.

- [43] N. Estrada, E. Azéma, F. Radjai, and A. Taboada. Identification of rolling resistance as a shape parameter in sheared granular media. *Phys. Rev. E*, 84:011306, 2011.
- [44] N. Estrada, A. Taboada, and F. Radjai. Shear strength and force transmission in granular media with rolling resistance. *Phys. Rev. E*, 78:021301, 2008.
- [45] A. Fall, A. Lemaitre, F. Bertrand, D. Bonn, and G. Ovarlez. Shear Thickening and Migration in Granular Suspensions. *Phys. Rev. Lett.*, 2010.
- [46] R.S. Farr, J.R. Melrose, and R.C. Ball. Kinetic theory of jamming in hard-sphere start-up flows. *Phys. Rev. E*, 55:7203–7211, 1997.
- [47] H. Flyvbjerg and H.G. Petersen. Error estimates on averages of correlated data. *Journal of Chemical Physics*, 91:461–466, 1989.
- [48] A.J. Forsyth and Rhodes M.J. A simple model incorporating the effects of deformation and asperities into the van der waals force for macroscopic spherical solid particles. *J. Colloid Interface Sci.*, 223(1):133–138, 2000.
- [49] Y. Forterre and O. Pouliquen. Flows of dense granular media. *Annu. Rev. Fluid Mech.*, 40:1–24, 2008.
- [50] Z. Fournier, D. Geromichalos, S. Herminghaus, M. M. Kohonen, F. Mugele, M. Scheel, M. Schulz, B. Schulz, Ch. Schier, R. Seemann, and A. Skudelný. Mechanical properties of wet granular materials. *J. Phys.: Condens. Matter*, 17:S477–S502, 2005.
- [51] R. García Rojo, H. J. Herrmann, and S. McNamara, editors. *Powders and Grains 2005*, Leiden, 2005. Balkema.
- [52] GDR MiDi. On dense granular flows. *European Physical Journal E*, 14:341–365, 2004.
- [53] H. Geoffroy, H. di Benedetto, A. Duttine, and C. Sauzéat. Dynamic and cyclic loadings on sands: results and modelling for general stress-strain conditions. In H. di Benedetto, T. Doanh, H. Geoffroy, and C. Sauzéat, editors, *Deformation characteristics of geomaterials*, pages 353–363, Lisse, 2003. Swets and Zeitlinger.
- [54] F. A. Gilabert, J.-N. Roux, and A. Castellanos. Computer simulation of model cohesive powders: Influence of assembling procedure and contact laws on low consolidation states. *Phys. Rev. E*, 75(1):011303, 2007.
- [55] F. A. Gilabert, J.-N. Roux, and A. Castellanos. Computer simulation of model cohesive powders: Plastic consolidation, structural changes, and elasticity under isotropic loads. *Phys. Rev. E*, 78(1):031305, 2008.
- [56] I. Goldhirsch. Scale and kinetics of granular flows. *Chaos*, 9:659–672, 1999.
- [57] E. Guazzelli and J. Morris. *A Physical Introduction to Suspension Dynamics*. Cambridge University Press, 2011.
- [58] E. Guyon, J.-P. Hulin, and Petit L. *Hydrodynamique physique*. CNRS Éditions, EDP Sciences, 2001.
- [59] T. C. Halsey and A. J. Levine. How sandcastles fall. *PRL*, 80:3141–3144, 1998.
- [60] J.-P. Hansen and I. R. McDonald. *Theory of Simple Liquids*. Academic Press, 1986.
- [61] J. Happel and H. Brenner. *Low Reynolds Number Hydrodynamics*. Martinus Nijhoff, The Hague, 1983.
- [62] T. Hatano. Power-law friction in closely packed granular materials. *Phys. Rev. E*, 75:060301(R), 2007.
- [63] S. Herminghaus. Dynamics of wet granular matter. *Advances in Physics*, 54:3, 221–261, 2005.
- [64] H. J. Herrmann, J.-P. Hovi, and S. Luding, editors. *Physics of Dry Granular Media*, Dordrecht, 1998. Balkema.
- [65] P.-Y. Hicher. Elastic properties of soils. *ASCE Journal of Geotechnical Engineering*, 122:641–648, 1996.

- 
- [66] H. Hinrichsen and D. E. Wolf, editors. *The Physics of Granular Media*, Berlin, 2004. Wiley-VCH.
- [67] I. Jordanoff and M. M. Khonsari. Granular lubrication: Toward an understanding of the transition between kinetic and quasi-fluid regime. *J. Tribol.*, 126(1):137–145, 2004.
- [68] J. N. Israelashvili. *Intermolecular and Surface Forces*. Academic Press, 1991.
- [69] K. Iwashita and M. Oda. *Mechanics of Granular Materials: An Introduction*. Taylor & Francis, Netherlands, 1999.
- [70] M. Jean. Contact Dynamics Method. In *Discrete-element Modeling of Granular Materials* [109], chapter 2, pages 27–66.
- [71] D. L. Johnson, K. Kendall, and A.D. Roberts. Surface energy and the contact of elastic solids. *Proc. R. Soc. London A*, 324:301–313, 1971.
- [72] K. L. Johnson. *Contact Mechanics*. Cambridge University Press, 1985.
- [73] P. Jop, Y. Forterre, and O. Pouliquen. A constitutive law for dense granular flow. *Nature*, 441:727–730, 2006.
- [74] M. M. Kohonen, D. Geromichalos, M. Scheel, C. Schier, and S. Herminghaus. On capillary bridges in wet granular materials. *Physica A*, 339:7–15, 2004.
- [75] I.M. Krieger and T.J. Dougherty. A mechanism for non-newtonian flow in suspensions of rigid spheres. *J. Rheol.*, 3:137–152, 1959.
- [76] A. Kudrolli. Granular matter: Sticky sand. *Nature Materials*, 7:174–175, 2008.
- [77] M. R. Kuhn and C. S. Chang. Stability, Bifurcation and Softening in Discrete Systems: A Conceptual Approach for Granular Materials. *International Journal of Solids and Structures*, 43:6026–6051, 2006.
- [78] R. Kuwano and R. J. Jardine. On the applicability of cross-anisotropic elasticity to granular materials at very small strains. *Géotechnique*, 52:727–749, 2002.
- [79] P.V. Lade and J.M. Duncan. Elastoplastic stress-strain theory for cohesionless soil. *J. Geotech. Eng. Div.*, 101:1037–1053, 1975.
- [80] L. D. Landau and E. M. Lifchitz. *Mécanique des fluides*. Mir, Moscow, 1989.
- [81] A. Lemaitre, J.-N. Roux, and F. Chevoir. What do dry granular flows tell us about dense non-brownian suspension rheology? *Rheologica Acta*, 48:925–942, 2009.
- [82] G. Lian, C. Thornton, and M. J. Adams. A theoretical study of the liquid bridge forces between two rigid spherical bodies. *J. of Colloid and Interface Sci.*, 161(1):138–147, 1993.
- [83] E.M. Lifshitz. The theory of molecular attraction forces between solid bodies. *Sov. Phys. JETP*, 2:73–85, 1956.
- [84] N. Maeda, J.N. Israelachvili, and M.M. Kohonen. Evaporation and instabilities of microscopic capillary bridges. *Proc. Natl. Acad. Sci. USA*, 100:803–808, 2003.
- [85] V. Magnanimo, L. La Ragione, J. T. Jenkins, P. Wang, and H. A. Makse. Characterizing the shear and bulk moduli of an idealized granular material. *Europhys. Lett.*, 81:34006, 2008.
- [86] T.S. Majmudar and R.P. Behringer. Contact force measurements and stress-induced anisotropy in granular materials. *Nature*, 435:1079–1082, 2005.
- [87] H. A. Makse, D. L. Johnson, and L. M. Schwartz. Packing of compressible granular materials. *Phys. Rev. Lett.*, 84(18):4160–4163, 2000.
- [88] R. Mani, D. Kadau, D. Or, and H. J. Herrmann. Fluid depletion in shear bands. *PRL*, 109:248001:1–5, 2012.
- [89] D. Maugis. *Contact, adhesion and rupture of elastic solids*. Springer, Berlin, 2000.
- [90] R. Mei, H. Shang, O.R. Walton, and J.F. Klausner. Concentration non-uniformity in simple shear flow of cohesive powders. *Powder Technology*, 112:102–110, 2000.

- [91] J. R. Melrose, J.H. van Vliet, and R.C. Ball. Continuous Shear Thickening and Colloid Surfaces. *Phys. Rev. Lett.*, 77:4660–4663, 1996.
- [92] J.R. Melrose and R.C. Ball. The pathological behaviour of sheared hard spheres with hydrodynamic interactions. *Europhys. Lett.*, 32:535–540, 1995.
- [93] J.R. Melrose and R.C. Ball. Continuous shear thickening transitions in model concentrated colloids - the role of interparticle forces. *J. Rheol.*, 48:937–960, 2004.
- [94] R. D. Mindlin and H. Deresiewicz. Elastic spheres in contact under varying oblique forces. *ASME Journal of Applied Mechanics*, 20:327–340, 1953.
- [95] N. Mitarai and F. Nori. Wet granular materials. *Advances in Physics*, 55:1, 1–45, 2006.
- [96] J.K. Mitchell and K. Soga. *Fundamentals of Soil Behavior*. Wiley, 2005.
- [97] D. M. Mueth, H. M. Jaeger, and S. R. Nagel. Force distribution in a granular medium. *Phys. Rev. E*, 57:3164–3169, 1998.
- [98] R.M. Nedderman. *Statics and Kinetics of Granular Materials*. Cambridge University Press, Cambridge, UK, 1992.
- [99] M. Nuth and L. Laloui. Effective stress concept in unsaturated soils: Clarification and validation of a unified framework. *Int. Journal for Numerical and Analytical Methods in Geomechanics*, 32:771–801, 2008.
- [100] C. O’Hern, L. E. Silbert, A. J. Liu, and S. R. Nagel. Jamming at zero temperature and zero applied stress: The epitome of disorder. *Phys. Rev. E*, 68(1):011306, 2003.
- [101] S. Ouaguenouni and J.-N. Roux. Force distribution in frictionless granular packings at rigidity threshold. *Europhysics Letters*, 39:117–122, 1997.
- [102] G. Ovarlez, F. Bertrand, and S. Rodts. Local determination of the constitutive law of a dense suspension of noncolloidal particles through magnetic resonance imaging. *J. Rheol.*, 50:259–292, 2006.
- [103] M. Parrinello and A. Rahman. Polymorphic transitions in single crystals: A new molecular dynamics method. *Journal of Applied Physics*, 52:7182–7190, 1981.
- [104] P.-E. Peyneau and J.-N. Roux. Frictionless bead packs have macroscopic friction, but no dilatancy. *Phys. Rev. E*, 78:011307, 2008.
- [105] P.-E. Peyneau and J.-N. Roux. Shear flow of sphere packings in the geometric limit. In A. CO, L.G. Leal, R.H. Colby, and A.J. Giacomin, editors, *Proceedings of the 15th International Congress on Rheology*, Monterey, CA, 2008. American Institute of Physics.
- [106] P.-E. Peyneau and J.-N. Roux. Solidlike behavior and anisotropy in rigid frictionless bead assemblies. *Phys. Rev. E*, 78:041307, 2008.
- [107] P.E. Peyneau. *Étude du comportement et du compactage de pâtes granulaires par simulation numérique discrète*. PhD thesis, École Nationale des Ponts et Chaussées, 2009.
- [108] O. Pitois, P. Moucheront, and X. Château. Liquid bridge between two moving spheres: An experimental study of viscosity effects. *J. Coll. Interf. Sci.*, 231:26–31, 2000.
- [109] F. Radjaï and F. Dubois. *Discrete-element modeling of granular materials*. Wiley, 2011.
- [110] F. Radjaï, M. Jean, J.-J. Moreau, and S. Roux. Force distribution in dense two-dimensional granular systems. *Phys. Rev. Lett.*, 77:274–277, 1996.
- [111] F. Radjaï and V. Richefeu. Bond anisotropy and cohesion of wet granular materials. *Phil. Trans. R. Soc. A*, 367:5123–5138, 2009.
- [112] F. Radjaï and V. Richefeu. Contact dynamics as a nonsmooth discrete element method. *Mechanics of Materials*, 41:715–728, 2009.
- [113] F. Radjaï and S. Roux. Contact dynamics study of 2d granular media : critical states and relevant internal variables. In Hinrichsen and Wolf [66], pages 165–187.



- 
- [114] F. Radjaï, s. Roux, and J.-J Moreau. Contact forces in a granular packing. *Chaos*, 9(3):544–550, 1999.
  - [115] F. Radjaï, D. E. Wolf, M. Jean, and J.-J. Moreau. Bimodal character of stress transmission in granular packings. *Phys. Rev. Lett.*, 80:61–64, 1998.
  - [116] D. C. Rapaport. *The Art of Molecular Dynamics Simulation*. Cambridge University Press, Cambridge, 2004.
  - [117] O. Reynolds. On the dilatancy of media composed of rigid particles in contact. *Philosophical Magazine (5th series)*, 20:469–481, 1885.
  - [118] V. Richefeu, M.S. El Youssoufi, and F. Radjaï. Shear strength properties of wet granular materials. *Phys. Rev. E*, 73:051304, 2006.
  - [119] V. Richefeu, F. Radjaï, and M.S. El Youssoufi. Stress transmission in wet granular materials. *European Physical Journal E*, 21:359–369, 2006.
  - [120] P. Rognon, J.-N. Roux, D. Wolf, M. Naaïm, and F. Chevoir. Rheophysics of cohesive granular materials. *Europhysics Letters*, 74:644–650, 2006.
  - [121] P.G. Rognon. *Rheology of cohesive granular materials—application to dense snow avalanches*. PhD thesis, École Nationale des Ponts et Chaussées, 2006.
  - [122] P.G. Rognon, J.-N. Roux, M. Naaïm, and F. Chevoir. Dense flows of cohesive granular materials. *J. Fluid Mech.*, 596:21–47, 2008.
  - [123] L. Rothenburg and N. P. Kruyt. Critical state and evolution of coordination number in simulated granular materials. *International Journal of Solids and Structures*, 41(2):5763–5774, 2004.
  - [124] J.-N. Roux. Geometric origin of mechanical properties of granular materials. *Phys. Rev. E*, 61:6802–6836, 2000.
  - [125] J.-N. Roux and F. Chevoir. Discrete numerical simulation and the mechanical behavior of granular materials. *Bulletin des Laboratoires des Ponts et Chaussées*, 254:109–138, 2005.
  - [126] J.-N. Roux and F. Chevoir. Simulation numérique discrète et comportement mécanique des matériaux granulaires. *Bulletin des Laboratoires des Ponts et Chaussées*, 254:109–138, 2005.
  - [127] J.-N. Roux and F. Chevoir. Dimensional Analysis and Control Parameters. In *Discrete-element Modeling of Granular Materials* [109], chapter 8, pages 199–232.
  - [128] J.-N. Roux and G. Combe. Quasi-Static Methods. In *Discrete-element Modeling of Granular Materials* [109], chapter 3, pages 67–101.
  - [129] A.N. Schofield and C.P. Wroth. *Critical state soil mechanics*. McGraw-Hill, London, 1968.
  - [130] L. Scholtès, B. Chareyre, F. Nicot, and F. Darve. Micromechanics of granular materials with capillary effects. *International Journal of Engineering Science*, 47:64–75, 2009.
  - [131] L. Scholtès, P.-Y. Hicher, F. Nicot, B. Chareyre, and F. Darve. On the capillary stress tensor in wet granular materials. *Int. Journal for Numerical and Analytical Methods in Geomechanics*, 33:1289–1313, 2009.
  - [132] S Shibuya, F. Tatsuoka, S. Teachavorasinskun, X.-J. Kong, F. Abe, Y.-S. Kim, and C.-S. Park. Elastic deformation properties of geomaterials. *Soils and Foundations*, 32:26–46, 1992.
  - [133] Z. Shojaaee. *Shear Bands in Granular Materials: Formation and Persistence at Smooth Walls*. PhD thesis, Universität Duisburg-Essen, 2012.
  - [134] Z. Shojaaee, J. N. Roux, F. Chevoir, and Wolf D. E. Shear flow of dense granular materials near smooth walls. i. shear localization and constitutive laws in the boundary region. *Phys. Rev. E*, 86:011301, 2012.
  - [135] A. Sierou and J. F. Brady. Rheology and microstructure in concentrated noncolloidal suspensions. *J. Rheol.*, 46:1031–1056, 2002.
  - [136] A. Sierou and J.F. Brady. Accelerated stokesian dynamics simulations. *J. Fluid Mech.*, 448:115–146, 2001.

- [137] L. E. Silbert, J. R. Melrose, and R. C. Ball. Colloidal microdynamics: Pair-drag simulations of model concentrated aggregated systems. *Phys. Rev. E*, 56:7067–7077, 1997.
- [138] L. E. Silbert, J. R. Melrose, and R. C. Ball. The rheology and microstructure of concentrated, aggregated colloids. *Journal of Rheology*, 43:673–700, 1999.
- [139] Leonardo E. Silbert, Gary S. Grest, and James W. Landry. Statistics of the contact network in frictionless and frictional granular packings. *Phys. Rev. E*, 66(36):061303, 2002.
- [140] J.R. Smart and D.T Leighton Jr. Measurement of the hydrodynamic surface roughness of noncolloidal spheres. *Phys. Fluids A*, 1:52–60, 1988.
- [141] F. Soulié, F. Cherblanc, M.S. El Youssoufi, and C. Saix. Influence of liquid bridges on the mechanical behaviour of polydisperse granular materials. *Int. J. Numer. Anal. Meth. Geomech.*, 30:213–228, 2006.
- [142] J. J. Stickel and R. L. Powell. Fluid mechanics and rheology of dense suspensions. *Annu. Rev. Fluid Mech.*, 37:129–149, 2005.
- [143] A. Taboada, N. Estrada, and F. Radjai. Additive decomposition of shear strength in cohesive granular media from grain scale interactions. *Phys. Rev. Lett.*, 97:098302, 2006.
- [144] I. Talu, G.I. Tardos, and J.R. van Ommen. Use of stress fluctuations to monitor wet granulation of powders. *Powder Technology*, 117:149–162, 2001.
- [145] P. Tegzes, T. Vicsek, and P. Schiffer. Avalanche dynamics in wet granular materials. *Phys. Rev. Lett.*, 89:094301, 2002.
- [146] J. Tejchman. *Shear Localization in Granular Bodies with Micro-Polar Hypoplasticity*. Springer, Heidelberg, 2008.
- [147] K. Terzaghi. *Principles of soil mechanics: a summary of experimental studies of clay and sand*. McGraw-Hill, New York, 1926.
- [148] C. Thornton and C. W. Randall. Applications of theoretical contact mechanics to solid particle system simulations. In M. Satake and J. T. Jenkins, editors, *Micromechanics of granular materials*, pages 245–252, Amsterdam, 1988. Elsevier.
- [149] D. Volfson, L.S. Tsimring, and I.S. Aranson. Partially fluidized shear granular flows: Md simulations and continuum theory. *Phys. Rev. E*, 68:021301, 2003.
- [150] W.M. Weber, D.K. Hoffman, and C.M. Hrenya. Discrete-particle simulations of cohesive granular flow using a square-well potential. *Granular Matter*, 6:239–254, 2004.
- [151] C.D. Willett, M.J. Adams, S.A. Johnson, and J.P.K. Seville. Capillary bridges between two spherical bodies. *Langmuir*, 16 (24):9396–9405, 2000.
- [152] David Muir Wood. *Soil Behaviour and Critical State Soil Mechanics*. Cambridge University Press, 1990.